Karlsruher Institut für Technologie | Institut für Hochfrequenztechnik und Elektronik

Alaska Satellite Facility

Deutsches Zentrum für Luft- und Raumfahrt

Bachelor Thesis

Antenna Pattern Correction in Elevation for a New SIR-C Processor

Hannes Kistner

Instructor: Prof. Dr.-Ing. Marwan Younis
Prof. Dr. Franz Meyer
Prof. Dr.-Ing. Thomas Zwick
Supervisor: Dr.-Ing. Valeria Gracheva
M.Sc. Mohamad Basim Alabd

Period: 01.11.2018 – 02.05.2019

Karlsruhe, 02.05.2019

Postanschrift: Institut für Hochfrequenztechnik und Elektronik
Kaiserstraße 12
D-76131 Karlsruhe
Gebäude: Engesserstraße 5, Geb. 30.10

Tel.: +49 (0) 721 608 4 2522
Sekr.: +49 (0) 721 608 4 2523
Fax: +49 (0) 721 608 4 5027
E-Mail: info@ihe.kit.edu
Web: www.ihe.kit.edu

Declaration

I hereby declare that I wrote my Bachelor Thesis on my own and that I have followed the regulations relating to good scientific practice of the Karlsruhe Institute of Technology (KIT) in its latest form. I did not use any unacknowledged sources or means and I marked all references I used literally or by content.

Karlsruhe, 02.05.2019

Hannes Kistner

Abstract

The Spaceborne Imaging Radar-C (SIR-C) was a radar system, which flew on two separate Space Shuttle missions in April and October 1994. Throughout these missions, a total of 143 hours of SAR data were recorded in multiple frequencies and polarizations. Unfortunately, high resolution SIR-C products are no longer available as the original SIR-C processor is no longer functional. To recover this historic dataset, the Alaska Satellite Facility is currently developing new software to process binary SIR-C data to high resolution, geocoded and calibrated SAR images.

This bachelor thesis contributes to the relative radiometric calibration of the new processor by developing an approach to correct the antenna patterns in elevation. The main challenges of the SIR-C antenna pattern correction were the multitude of different antenna beams generated by active antenna steering and the parameter uncertainties in the new processor. Implementation and verification of an antenna model, which derives the antenna elevation diagrams required for accurate image correction, is therefore a key element in the presented work. The antenna model was implemented using probe data from pre-flight feed current measurements and verified with in-orbit antenna elevation pattern estimates derived from real SIR-C Amazon rain forest acquisitions. It was found, that the uncertainty of the available SIR-C ephemeris data is too high in order to determine the antenna pointing direction with sufficient accuracy. Hence, one of the main challenges was the development of an approach, that provides reliable estimates of the geometric parameters based on the image data itself. A two pronged approach was implemented based on in-orbit antenna pattern estimates on one hand and beam nulling on the other. Beam nulling is a calibration method employed by SIR-C, which involved inverting the receive phase of half of the antenna array in elevation by 180 degrees. Thus the effective beam received has a notch or null at the boresight. The final implementation of the antenna pattern correction algorithm was tested on a total of 12 real SIR-C datatakes, which equates to about one terabyte of raw data. The test results were found to be consistent with original Jet Propulsion Laboratory technical reports and show that the antenna model approach was successfully applied. In-orbit measurements of the residual relative radiometric cross-swath errors after antenna pattern correction were better than $\pm 1\,\mathrm{dB}$, with best case scenarios as low as $\pm 0.11\,\mathrm{dB}$ over the Amazon.

Contents

List of Figures

List of Tables

1 Introduction

1.1 Spaceborne Imaging Radar-C

The Spaceborne Imaging Radar with payload C (SIR-C) was the third installment in a series of NASA earth-imaging SAR instruments to fly on the Space Shuttle. The series stated with SIR-A in 1981 and continued with SIR-B in l984 and SIR-C in 1994 [1]. Two Missions, also known under the name of Space Radar Laboratory (SRL), were flown aboard the Space Shuttle Endeavour in April and October, 1994. It was the first radar system in space capable of acquiring quad-polarization data with two frequencies at the same time ($1250\,\mathrm{MHz}$ L-band and $5300\,\mathrm{MHz}$ C- band) [2]. The innovative design by Jet Propulsion Laboratory (JPL) allowed for selection of system resources like pulse lengths or bandwidth to command the desired range resolution or swath-width. Additionally, the active phased array antennas enabled up to 23 degrees of electronic steering from the nominal 40 degrees off-nadir position. This translated into look angles between 17 and 63 degrees, which could be further extended by roll maneuvering of the Space Shuttle [3]. For wide-swath acquisitions, the phase-shifters of the antenna were programmed to spoil the antenna beam in order to obtain a more uniform antenna pattern. The radar system operated in 19 acquisition modes, differing by the combinations of polarization channels, pulse repetition frequency and bandwidth (resolution) [4]. On top of that, a number of experimental datasets were acquired using special radar modes such as along-track interferometry or SCANSAR mode, where swath widths up to $150\,\mathrm{km}$ were obtained by continuously varying the incidence angle during acquisition. A list of the different modes and a detailed description of SIR-C radar system is given in [2] and [3].

1.2 Motivation

The SIR-C/X-SAR Space Radar Laboratory represented a major technological innovation in radar remote sensing and was a precursor to other spaceborne SAR systems such as the Shuttle Radar Topography Mission (SRTM) in 2000 and the upcoming NISAR (launch in 2021). Throughout its two shuttle missions, SIR-C recorded more than 143 hours (93 terabits) of multi-frequency, polarimetric SAR data and obtained over 100 million square kilometers of ground coverage [5]. The SAR processor designed by JPL initially generated survey images with a course resolution of 100m [6] and only a few precision and interferometry products before it became inoperable in June 2005 [7]. Only, a fraction of the data collection has been processed into full resolution SAR

images needed for scientific application. The loss of the SIR-C data collection leaves a significant gap in Earth monitoring, namely between the L-band sensors of the SEASAT (1978) and ALOS (2006-2011) missions. In combination with other Satellite missions, C- and L-band data can be used for long-term observation of changes in landscape, infrastructure, and urban development. Since multi-frequency datasets with simultaneous acquisitions are still rare today, SIR-C also has particular value as a test environment for new spaceborne SAR algorithms.
In accordance with its goal to make remote-sensing data accessible to everyone, The Alaska Satellite Facility (ASF) [8] has built a new SIR-C processor based on JPL specifications [6]. ASF is currently processing all of the SIR-C binary data at full resolution and plans on making SIR-C Single Look Complex (SLC) and Multi Look Complex (MLC) image products available through the infrastructure of the Distributed Active Archive Center Fairbanks [6]. One of the remaining challenges in this endeavor is calibration of the image data, in order to establishe a direct relationship between radar backscatter and image pixel numbers. This is prerequisite for a wide variety of modern applications, which rely on the measurement aspect of SAR to derive accurate geophysical parameters [9]. To arrive at SAR images with absolute radiometric calibration, several steps such as the correction of range spreading loss or the effects of the antenna gain pattern (AGP) in elevation are necessary. The work done in the framework of this thesis is inserted in this context and more specifically focuses on the development of an antenna pattern correction algorithm (APCA) and subsequent implementation into the SIR-C processing chain. The solution to this problem involves the design of L- and C-band antenna models based on analysis of pre-flight probe measurements and requires extensive testing with real SIR-C data. Verification of the antenna elevation pattern and estimation of the residual cross-swath radiometric uncertainties will be performed with tropical rain forest images generated by the new SIR-C processor.

1.3 Problem Statement

The Alaska Satellite Facility is currently generating full resolution SIR-C products with a newly developed processor. The processing flow can be divided into four steps [10]:

1. **Decoding:** The original binary files are decoded into header/signal data format and cleaned to reduce the bit error rate. The header contains all parameters that are needed for processing including the orbital state vectors.

2. **Pre-Processing:** Depending on acquisition mode, the data need to be rearranged. This pre-processing step is necessary in order for a single processor to handle data from all modes of operation.

3. **Processing:** The Range-Doppler imaging algorithm is employed to focus SIR-C raw data into SLC or MLC products.

4. **Post-Processing:** The antenna pattern correction is performed and calibration parameters are applied.

The presented work addresses this fourth step, namely the correction of the antenna elevation pattern in order to achieve relative radiometric cross-swath calibration. The SIR-C radar image data in particular, presents some unique challenges in this regard, which shall subsequently be discussed:

Number of acquisition modes: The large number of operational modes, antenna configurations and shuttle maneuvers complicates the handling of different data acquisitions significantly. Currently, ASF is processing data acquired with 14 different modes, differing by the combination of active radar channels (number of polarization), pulse repetition frequency and bandwidth [10]. Additionally, the SIR-C antenna was capable of electronically steering to 256 beam positions [4] and offered eight different beamwidths ranging from 5 to 16 degrees in elevation. Data was collected over a wide range of incidence angles ($17°$ to $63°$) in a variety of programmable elevation beam patterns. The level of variation (see Fig. 3.4.2) increases the scope of testing substantially compared to other SAR sensors.

Availability of test data: Testing will focus on whether the antenna model matches the elevation patterns of actual SIR-C data and what ranges of radiometric variation remain in the cross track direction after the APCA is applied. For this purpose, SIR-C data from several tropical rain forest scenes are needed (see Sec. 4.1). The Amazon offers the best conditions for testing since it can be characterized as a flat uniform scatterer. Unfortunately, the number of suitable test sites is limited and only a portion of the acquired rain forest data has been processed to completion. In the interest of making more data available for testing, other sites such as the Sub-Saharan rain forest were considered as well. In order to derive meaningful figures of merit from such sub-optimal data, additional screening and cleaning steps are necessary.

Parameter uncertainty: A major source of calibration error are the large attitude uncertainties and high attitude drift rates of the space shuttle platform. Limited knowledge of the viewing geometry can cause significant angular offsets between the nominal reference patterns and the actual image data. The reason for the discrepancies is the available shuttle ephemeris information. There are three different sources for obtaining SIR-C ephemeris data: The Mission Operations Subsystem (MOS), state vectors embedded into the file headers, and Post-Flight Attitude and Trajectory History (PATH) tapes from the Johnson Space Center [3]. PATH tape data are most reliable in terms of completeness and accuracy but are not released for civilian use. Instead, the availability of ephemeris information is limited to the file headers, which are quoted in [11] as being the least accurate source. Hence, one of the main challenges is the development of an approach, that provides reliable estimates of the geometric parameters based on the image data itself. The

uncertainties involved in the attitude information are given in Table 2.3.1.

Access to Documentation: Given that the original processor was developed over 25 years ago, it is not surprising that the intricacies of SIR-C are not as well known today as they once used to be. Most of the records are in the form of paper copies, while others are still classified by the U.S. Government. Even though a number of documents has since been digitized, there remain multiple gaps in areas relevant to this thesis.
According to [4] the original SIR-C antenna pattern generation model achieved excellent results, reducing the residual relative cross track uncertainty well below the goal of $\pm 1\,\mathrm{dB}$. This software and many of the pertinent data records have since been lost when the old SIR-C Ground Data Processing System became inoperable in 2005 [7]. Coupled with the issues mentioned above, these circumstances conspire to make exact replication of the original calibration procedure impossible. Instead, the new processing chain had to be built from the ground up.

Aim and Scope of this Thesis: This set of problems motivates the development of a post processing software tool for antenna elevation pattern correction, which, if necessary, estimates the relevant parameters from the (raw) image data itself. This tool will provide the means to automate the important step of antenna pattern correction in the ongoing effort of making calibrated SIR-C products available to the scientific community. The aim of this thesis is to achieve an accuracy of $\pm 1\,\mathrm{dB}$ in terms of residual range variation (peak to peak excursion). This goal is consistent with the JPL requirements for relative cross swath calibration in SIR-C data [4]. Here, the relative cross-swath radiometric error is defined as the uncertainty in the estimate of the backscatter coefficient ratio between two image pixels at different range locations from the same image [11]. If performance is within the stated limits, the final APCA will be integrated into the new SIR-C processing chain. In addition, the Matlab subroutines will be designed to allow optional user-supplied input parameters for individual optimization.

1.4 Thesis Structure

This thesis is organized as follows. To establish the necessary background, Chapter 2 summarizes the basics of SAR image processing, radiometric calibration and phased array antennas. An overview of the SAR radar equation, backscatter conventions and SIR-C datatakes is also given, as they will be referenced in later chapters. The core of the thesis is divided into three parts:

- Antenna pattern modeling for the SIR-C phased array antennas in Chapter 3.
- Verification of the antenna model in Chapter 4.

- Development of an approach, that compensates potential inaccuracies in the geometric parameters and implementation of the final antenna pattern correction algorithm in Chapter 5.

In Chapter 6, the results of the antenna pattern correction are presented and discussed. Chapter 7 provides a conclusion and also includes an outlook for topics which may be investigated, to further improve the SIR-C antenna pattern correction in the future.

2 Theoretical Basics

In this chapter, several general principles of Synthetic Aperture Radar are summarized. The following sections will discuss the basics of SAR image processing, radiometric calibration and the phased array antennas as they relate to SIR-C. An overview of the SAR radar equation, backscatter conventions and SIR-C datatakes is also given, since they will be referenced in later chapters.

2.1 Synthetic Aperture Radar

Synthetic Aperture Radar is a remote sensing system that generates high-resolution images for scientific and commercial purposes. The applications of SAR are as diverse as, oceanography, forestry, agriculture, climate change research, environmental monitoring, 2-D and 3-D mapping, change detection and planetary exploration [12]. The name Synthetic Aperture refers to the concept of simulating a very large antenna by mounting a radar system on a moving platform. Motion in a direction perpendicular to the antenna beam causes Doppler-shifts in the radar signal that can be processed to achieve much finer spatial resolution in azimuth than conventional beam-scanning radars. Since its introduction to the civilian community in the 1970's, the use of SAR in remote-based investigations has become common practice. The popularity is mainly based upon the following distinguishing features [13]:

1. Unlike optical imaging systems, SAR carries its own illumination source and can therefore run day and night.

2. The microwave operating frequencies of SAR pass through clouds, allowing for uninterrupted radar imaging under all weather conditions.

3. SAR-systems provide complementary information to optical Sensors that can sometimes result in better discrimination of surface features. An example is oil slick detection, which is based on the effect that oil smooths the surface of water. Additionally, SAR can make polarimetric observations (HH, VV, HV, VH) that provide information about geological composition, vegetation and soil moisture.

4. The geometric resolution is independent of the distance between target and sensor.

5. The SAR signal has coherency, in that the start time and phase of each pulse are controlled

precisely. This property is pivotal for a wide range of applications that use interferometric techniques.

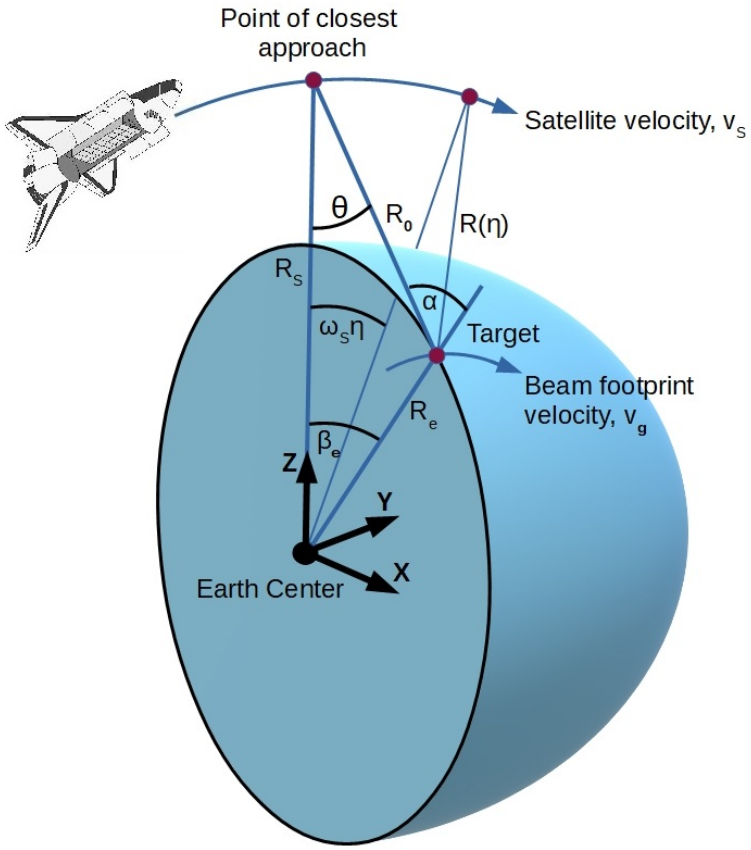

Figure 2.1.1: Spaceborne SAR acquisition geometry.

In the SAR image, the direction along the satellite's track is referred to as azimuth, while the cross track direction is called range direction. The terms "cross-swath" and "cross-track" will be used interchangeably in this thesis. As the platform moves, the distance between antenna and target is changing constantly. The smallest distance is called Range of Closest Approach and is abbreviated with R_0 in Figure 2.1.1. The nadir is the point on the ground directly beneath the sensor and the extend of the imaged area in ground range is called swath width. The angle θ refers to the antenna look angle at boresight.If the antenna look direction is not perpendicular to the flight track a so called squint angle must be considered. Often times the antenna is squinted with respect to the direction it should have, in order to achieve a Doppler Shift of zero when the target crosses the middle of the antenna beam. Furthermore, an ellipsoid model of the Earth is used with an earth-centered rotational (ECR) coordinate system. A more detailed description of the ellipsoid model and the coordinate system is given in Section 2.5.

2.1.1 Cross-Track (Range) Signal

Much like in conventional radar systems the range direction in SAR is resolved by measuring propagation delays between the transmitted pulses and the radar echoes. If a single-tone radar signal is used, the cross track resolution on the ground is determined only by the pulse duration τ_{p}. In order to be distinguishable from one another the trailing edge of the echo pulse from a close target must always arrive before the leading edge of a more distant target echo reaches the sensor. The resolution in ground range is:

$$\Delta R_{\mathrm{g}} = \frac{\tau_{\mathrm{p}} c}{2\sin(\alpha)}, \tag{2.1.1}$$

where c is the speed of light and α is the angle of incidence. Shorter pulses yield better resolution but also carry less energy and therefore result in a lower Signal to Noise Ratio (SNR). In order to achieve the desired resolution of a few meters, the required pulse length would not be sufficient to produce adequate SNR for reliable target detection [14]. Instead, a technique called pulse compression is employed that uses a longer frequency chirp, usually with a linear frequency modulation (FM) (see Fig. 2.1.2). The signal is then mixed with a carrier frequency f_0 and usually

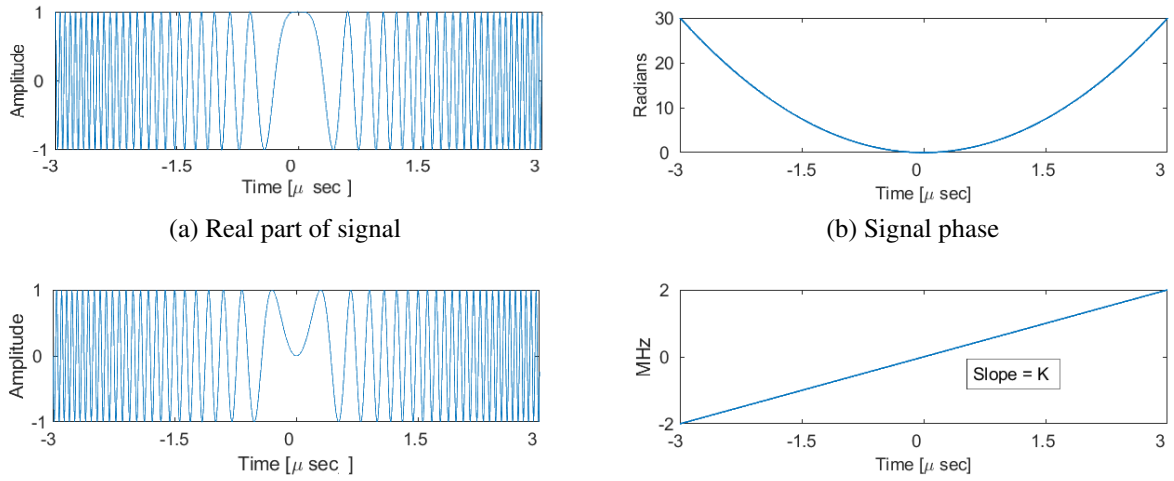

(a) Real part of signal

(b) Signal phase

(c) Imaginary part of singal

(d) Signal frequency

Figure 2.1.2: Amplitude, phase, and frequency of a linear FM pulse [13].

weighted with a window function $w(\tau)$. Commonly used carrier frequencies in SAR are found in L-band ($1-2\,\mathrm{GHz}$), C-band ($3.75-7.5\,\mathrm{GHz}$), and X-band ($7.5-12\,\mathrm{GHz}$) [12].The frequency bands are associated with certain backscatter properties, the most notable difference being the amount of surface penetration. The pulse envelope $w(\tau)$ is usually approximated by a rectangular window the size of the pulse duration, though additional weighing may be applied to reduce the side lobes of the impulse response function.
A linear FM radar pulse can be described by equation (2.1.2) [13]

$$s_{\mathrm{pulse}}(\tau) = w(\tau) \cdot \cos(2\pi f_0 \tau \pm \pi K_{\mathrm{r}} \tau^2), \tag{2.1.2}$$

where K_r is the FM rate

$$K_{\mathrm{r}} = \frac{B_{\mathrm{r}}}{\tau_{\mathrm{p}}}, \tag{2.1.3}$$

and B_{r} is the chirp bandwidth. The range delay τ is also called "fast time". In contrast, "slow time" η is used to parameterize the location of the platform. These names refer to the corresponding distances in range and azimuth, which are related to the speed of light and the comparatively slow velocity of the radar platform.
The use of pulse compression techniques requires additional processing of the signal in order to produce a focused image. This is done by matched filtering, which is further discussed in Section 2.2.2. As a result, the range resolution is now determined by the bandwidth B_{r}. The approximate resolution on the ground is [14, 13]

$$\delta R_{\mathrm{g}} = \frac{\delta R}{\sin(\alpha)} = \frac{0.886 \cdot \gamma_{w,\mathrm{r}} \cdot c}{2B_{\mathrm{r}} \sin(\alpha)}, \tag{2.1.4}$$

where δR is the slant range resolution and $\gamma_{w,\mathrm{r}}$ is a factor that accounts for broadening of the impulse response width due to weighting with a window function.

2.1.2 Along-Track (Azimuth) Signal

In SAR the term (geometric) resolution generally refers to the distance between the -3 dB points of the impulse response function, i.e. the width of the radar response to a point target. For a conventional side looking airborne radar (SLAR) this means that the azimuth resolution is determined by the beamwidth ϕ_{bw} and distance R between sensor and target [13]

$$\delta_{\mathrm{a}} = R \cdot \phi_{\mathrm{bw}} = 0.886 \frac{R\lambda}{L_{\mathrm{a}}}, \tag{2.1.5}$$

where λ is the wavelength of the carrier frequency and L_{a} is the length of the Antenna in azimuth direction. Without signal processing spaceborne Radar systems would yield δ_{a} on a scale of thousands of meters. The central idea of SAR, often credited to Carl Wiley (1965), is to improve the along-track resolution by processing Doppler shifts in the received signal. All point targets along the track of the moving radar have different relative velocities with respect to the radar platform at all times. Thus, the along track distance of a target from a point directly beneath the sensor is encoded into the Doppler shifts relative to the transmitted frequency. The waveform that represents the Doppler shifted, received signal is effectively sampled by the radar pulses with the pulse repetition frequency (PRF). If the radar echos are analyzed in the frequency domain, any energy observed at a specific Doppler frequency is associated with a distinct coordinate in the along track dimension. By this means, targets at the same range can be discriminated even if they are in the beam at the same time[14]. The instantaneous Doppler frequency $f_{\mathrm{D}}(\eta)$ is the first derivative of the phase

$$\varphi_{\mathrm{a}}(\eta) = -\frac{4\pi}{\lambda} R(\eta), \tag{2.1.6}$$

with respect to the slow time:

$$f_{\mathrm{D}}(\eta) = \frac{1}{2\pi}\frac{\mathrm{d}\varphi_{\mathrm{a}}(\eta)}{\mathrm{d}\eta}. \tag{2.1.7}$$

Here, λ is the wavelength of the carrier frequency. Using the geometry defined in Figure 2.1.1, the slant range distance R at time η can be describes as:

$$R(\eta) = \sqrt{(R_{\mathrm{e}}\sin\beta_{\mathrm{e}})^2 + (R_{\mathrm{s}}\sin\omega_{\mathrm{s}}\eta)^2 + (R_{\mathrm{s}}\cos\omega_{\mathrm{s}}\eta - R_{\mathrm{e}}\cos\beta_{\mathrm{e}})^2} \tag{2.1.8}$$

$$\Leftrightarrow R(\eta) = \sqrt{R_{\mathrm{e}}^2 + R_{\mathrm{s}}^2 - 2R_{\mathrm{s}}\cos\omega_{\mathrm{s}}\eta R_{\mathrm{e}}\cos\beta_{\mathrm{e}}}. \tag{2.1.9}$$

For small angles, sine and cosine can be approximated by the first two terms of a Taylor Series as $\sin\omega_{\mathrm{s}}\eta \approx \omega_{\mathrm{s}}\eta$ and $\cos\omega_{\mathrm{s}}\eta \approx 1 - (\omega_{\mathrm{s}}\eta)^2/2$. Thus, the range equation (2.1.9) becomes

$$R(\eta) = \sqrt{\underbrace{R_{\mathrm{e}}^2 + R_{\mathrm{s}}^2 - 2R_{\mathrm{s}}R_{\mathrm{e}}\cos\beta_{\mathrm{e}}}_{:=R_0} + R_{\mathrm{s}}\omega_{\mathrm{s}}^2\eta^2 R_{\mathrm{e}}\cos\beta_{\mathrm{e}}}. \tag{2.1.10}$$

Assuming that the Earth is locally spherical and a constant orbit altitude is maintained over the acquisition, $R_{\mathrm{s}}\omega_{\mathrm{s}}$ is the satellite velocity v_{s} and $R_{\mathrm{e}}\omega_{\mathrm{s}}\cos\beta_{\mathrm{e}}$ is the beam footprint velocity v_{g} on the ground [13]. In addition, the pseudo velocity $v_{\mathrm{r}} = \sqrt{v_{\mathrm{s}}v_{\mathrm{g}}}$ is introduced as the effective radar velocity in order to model the range equation with the following hyperbola:

$$R(\eta) = \sqrt{R_0^2 + (v_{\mathrm{r}}\eta)^2}. \tag{2.1.11}$$

For low squint angles, the parabolic form, given by a second order Taylor series expansion is a valid approximation:

$$R(\eta) \approx R_0 + \frac{(v_{\mathrm{r}}\eta)^2}{2R_0}, \tag{2.1.12}$$

where R_0 is the distance of closes approach. The approximation leads to following azimuth (Doppler) frequency:

$$f_{\mathrm{D}}(\eta) = -\frac{2v_{\mathrm{r}}^2}{R_0\lambda}\eta. \tag{2.1.13}$$

This equation shows, that the signal in azimuth also has the characteristics of a linear frequency modulated pulse with a chirp rate of

$$K_{\mathrm{a}} = \frac{2v_{\mathrm{r}}^2}{R_0\lambda}. \tag{2.1.14}$$

Much like in range, the focusing in azimuth is done by matched filtering, which means that the geometric resolution is no longer dependent on the distance R. Instead, the resolution in azimuth directly relates to the Doppler bandwidth Δf_{D}, which is the frequency excursion experienced while a given target is illuminated by the -3 dB antenna beam [13]:

$$\Delta f_{\mathrm{D}} = K_{\mathrm{a}}T_{\mathrm{a}} = K_{\mathrm{a}}\cdot\frac{\phi_{\mathrm{bw}}R_0}{v_{\mathrm{g}}} = K_{\mathrm{a}}\cdot 0.886\cdot\frac{\lambda R_0}{L_{\mathrm{a}}v_{\mathrm{g}}} = 0.886\cdot\frac{2v_{\mathrm{s}}}{L_{\mathrm{a}}}. \tag{2.1.15}$$

Again, note that the above result is an approximation for low squint angles and a rectangular window in the azimuth frequnecy domain spanning the -6 dB bandwidth (two-way -6 dB antenna beam). The Resolution is given by [13]

$$\delta_{\mathrm{a}} = 0.886 \frac{v_{\mathrm{g}}}{\Delta f_{\mathrm{D}}} \gamma_{\mathrm{w},a} = \frac{L_{\mathrm{a}}}{2} \frac{v_{\mathrm{g}}}{v_{\mathrm{s}}} \gamma_{\mathrm{w},a}. \tag{2.1.16}$$

$\gamma_{w,\mathrm{a}}$ is a factor that accounts for broadening of the impulse response width due to weighting with a window function. Since $\gamma_{w,\mathrm{a}} v_{\mathrm{g}}/v_{\mathrm{s}} \approx 1$, the resolution in azimuth is often quoted as $\delta_{\mathrm{a}} = L_{\mathrm{a}}/2$.

2.1.3 Synthetic Aperture

To improve the geometric resolution of a SAR system, signal processing is used to effectively synthesize a more narrow beamwidth in azimuth. The equivalent effective antenna length resulting from equation (2.1.5) is what is called the Syntetic Aperture length L_{s}. It is the distance the sensor travels during the time a target is illuminated by the radar beam (see Fig. 2.1.3). The Synthetic Aperture length can be thousands of meters long in the spaceborne case and is described by [13] as:

$$L_{\mathrm{s}} = 0.886 \cdot \frac{R(\eta_{\mathrm{c}}) \cdot \lambda}{L_{\mathrm{a}}} \cdot \frac{v_{\mathrm{s}}}{v_{\mathrm{g}}}, \tag{2.1.17}$$

where $R(\eta_{\mathrm{c}})$ is the slant range to a target at the time it crosses the beam center. A method by which the previously discussed Doppler history of a target can be exploited to focus the signal, is described in Section 2.2.4.

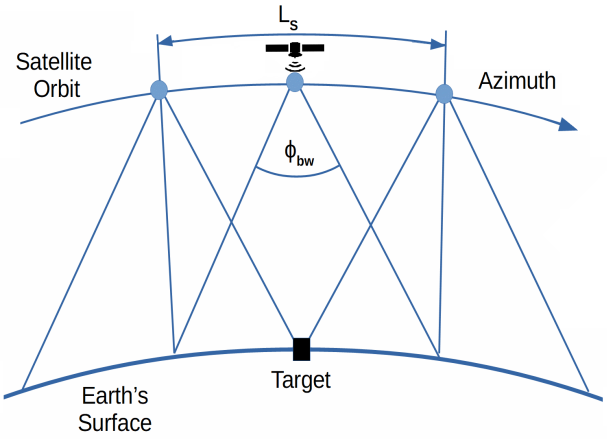

Figure 2.1.3: Synthetic aperture length.

2.2 Range Doppler Algorithm

Fundamentally, the radar signal received by the SAR-antenna is a voltage as a function of time. This raw-data recording is converted into a singlelook complex (SLC) images by means of digital signal processing. The SAR processing method used for SIR-C data is called the Range Doppler Algorithm (RDA). It was originally developed for the SEASAT SAR system in 1978 and is arguably the simplest and most commonly used SAR processing algorithm to this day [13]. It is based on two separate matched filtering operations in the frequency domain of both range and azimuth.

As following sections will show, a point target will appear as a hyperbolic shaped reflection as it moves through the synthetic aperture (see Eq. (2.1.11) and the approximation in Eq. (2.1.12)). In other words, the target energy locus will migrate through the memory cells in range, which must be corrected prior to focusing the image along the azimuth direction. The name Range Doppler Algorithm stems from the fact that this Range Cell Migration Correction (RCMC) is done in the range time and azimuth frequency domain. Since the frequency modulation in azimuth is caused by the Doppler effect this configuration is called the Range-Doppler-Domain. The RDA processing sequence is given in Fig. 2.2.1. The steps are visualized using simulated SAR data for a single point target. A sinc-like antenna patter in azimuth and a rectangular window in range was used to produce the visualized results. Real SAR data naturally contain the radar backscatter of a multitude of different targets in each sample.

2.2.1 Two Dimensional Signal

In order to synthesize a two dimensional image out of the one dimensional voltage recording, the waveform is discretized by the sampling rate f_s, and written into successive rows in the signal memory. The segmentation is done in accordance with the transmit/receive cycles, where each row represents the received ground echo of one radar pulse. In other words, the azimuth dimension is sampled by the pulse repetition frequency (PRF). By this arrangement, a 2D memory matrix is obtained, in which the samples in the vertical axis represent a time difference of $1/f_\mathrm{s}$ whereas the horizontal samples are separated by the pulse repetition interval $1/\mathrm{PRF}$. Each column therefore corresponds to the same range from the sensor (Eq. (2.2.1)), while the vertical time axis can be converted to azimuth distance from the nadir point by Eq. (2.2.2):

$$R(\tau) = \frac{c\tau}{2} \tag{2.2.1}$$

$$x(\eta) = v_\mathrm{g}\eta, \tag{2.2.2}$$

where τ is fast time and η is slow time. From Equation (2.1.11) we know, that the instantaneous slant range $R(\eta)$ changes as the sensor approaches and passes the target. This is the key principle of SAR operation, since azimuth resolution is directly related to the resulting Doppler shifts. An inevitable consequence however, is that a point target response will necessarily occur at different

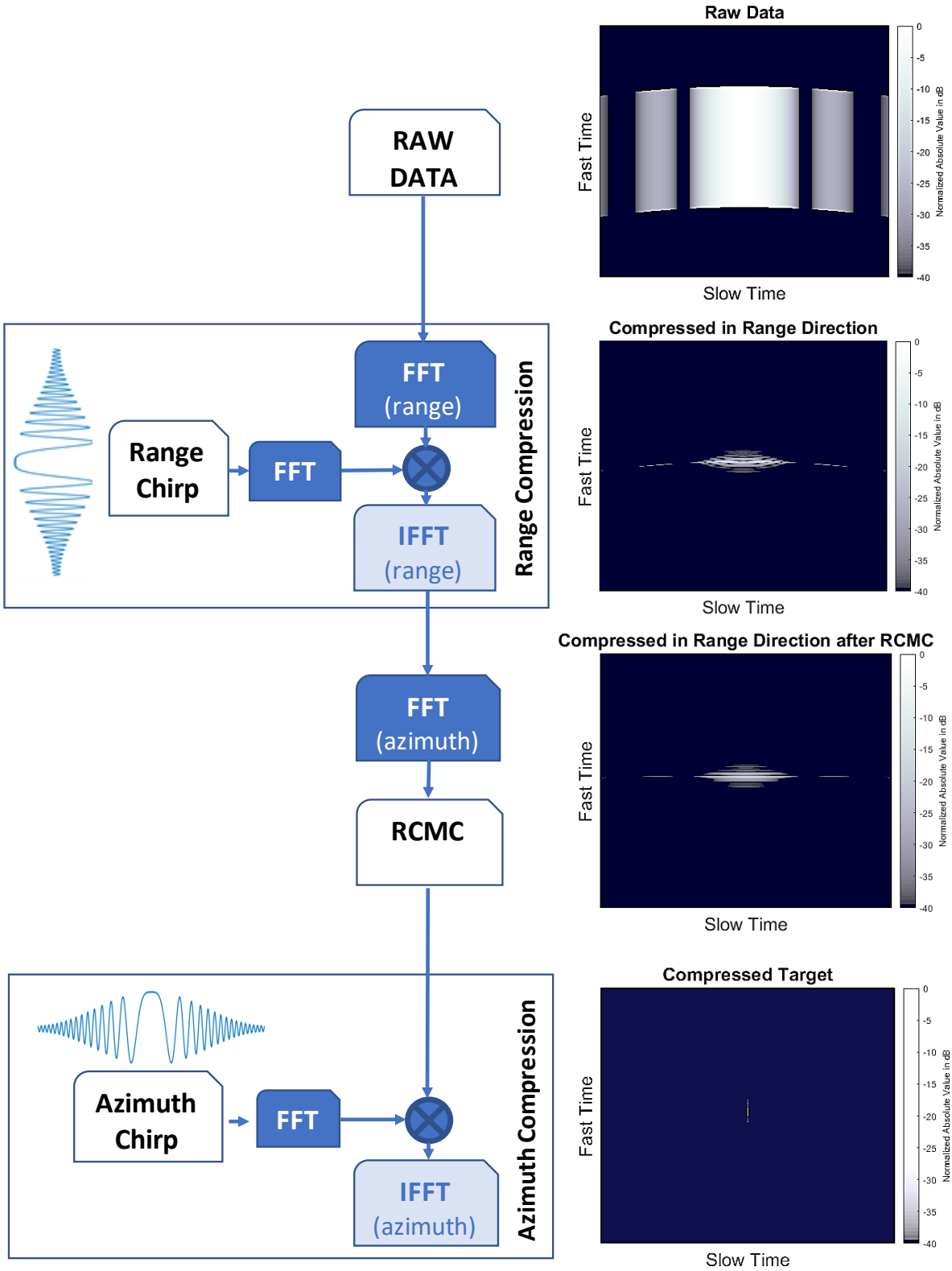

Figure 2.2.1: Range Doppler Algorithm.

ranges for different pulses [14]. The instantaneous slant range is a function of the slow time and can be approximated by Equation (2.1.12) for the low squint case. As a result of the change in slant range, a point target's locus of energy also migrates through the range cells in the memory matrix.This phenomenon, known as Range Cell Migration (RCM), is shown in Figure 2.2.2.The signals along the slow and fast time axis are both characterized by a FM chirp. In the range dimension this frequency chirp is due to the modulation discussed in Section 2.1.1 whereas the azimuth chirp is caused by the Doppler effect. Note that the illustration in Fig. 2.2.2 is not to scale. The radar echo of a point target is usually captured in hundreds of range and azimuth samples, while the range cell migration only changes by a few cells.

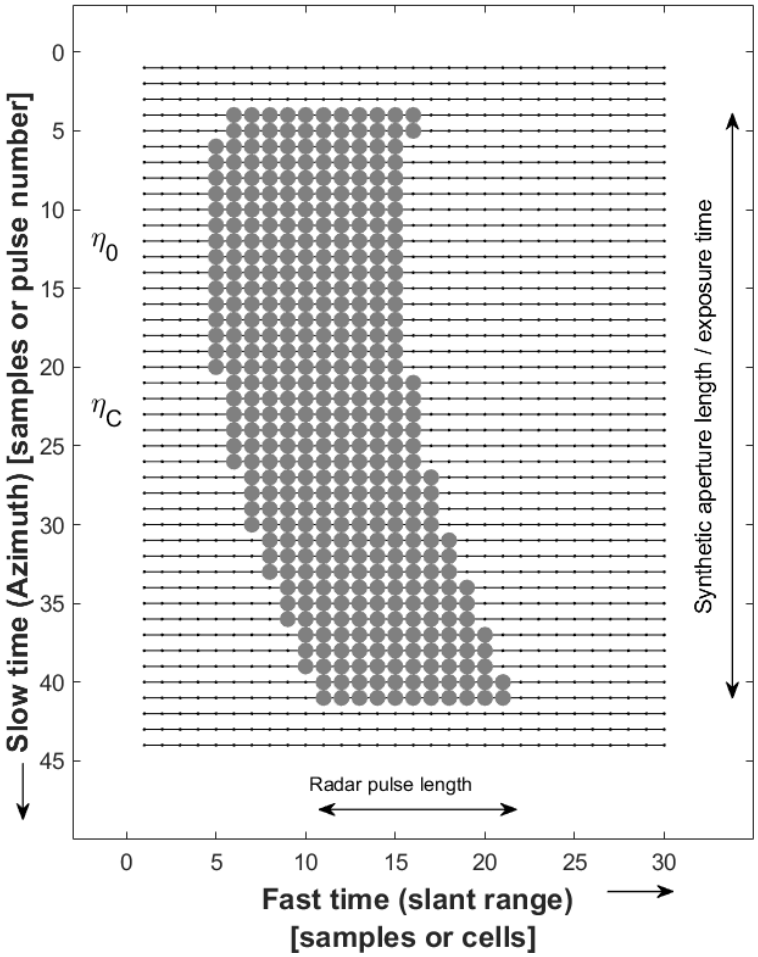

Figure 2.2.2: Range Cell Migration (RCM) of a point target in a two-dimensional data matrix (illustration not to scale).

2.2.2 Range Compression

The received signal is a real valued waveform that still contains the radar carrier frequency $\cos(2\pi f_0 \tau)$. After f_0 is removed, a quadrature demodulator produces the complex baseband signal. This is what is referred to as the raw data, which consists of the complex reflectivity of the surface convolved with the FM chirp. To recover the complex reflectivity of the target, the signal from each transmitted pulse is passed through a matched filter. Matched filtering is performed by a convolution of the complex conjugated, time reversed range reference function, which is a replica of the transmitted chirp itself (Fig. 2.2.3). This process is usually done in the frequency domain by multiplying the Discrete Fourier Transform (DFT) of the matched filter and zeropadded data. In the simplest case, the spectrum of the matched filter is confined by a rectangular window. This causes a substantial amount of the target energy to leak into side lobes and impedes the detection of weak targets in the vicinity of strong ones. To reduce this effect, windowing, for example with a raised cosine squared window [15], is applied to the spectrum of the matched filter. This however comes at the cost of broadening the Impulse Response Width, which directly relates to the geometric resolution of the SAR image. The Range Compression is complete after the signal has been transformed back into the time domain by a Inverse Fast Fourier Transform (IFFT) along the range dimension.

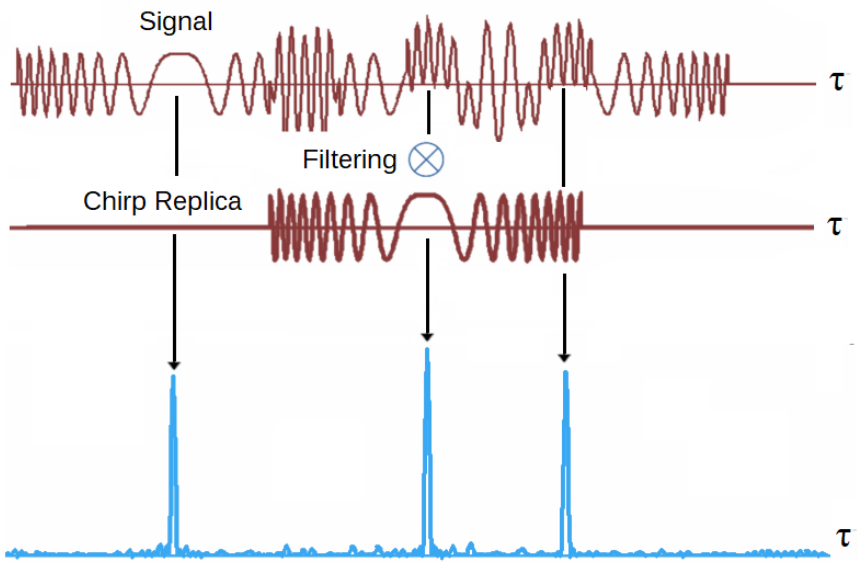

Figure 2.2.3: Pulse compression principle.

2.2.3 Range Cell Migration Correction

As discussed in Section 2.2.1, the signal from a point target will migrate in range, as it moves through the synthetic aperture. The shape of this curvature is determined by the precise flight

trajectory of the target as seen by the air or spacecraft carrying the radar sensor. The locus of the range cells is the curve $R(\eta)$, which usually can be approximated by Equation (2.1.12). In addition, there may be linear drifts due to an elliptical orbit and earth rotation [16]. Before the signal can be focused in azimuth, it must be migrated back, so that the energy from point targets is situated at the same range bin. This is called Range Cell Migration Correction (RCMC) and can be implemented in different ways [13]. As indicated by the name, the RDA performs RCMC in the range-Doppler domain, which is also the most distinguishing feature of this algorithm. Figure 2.2.4 depicts the range migration in the range- Doppler domain. Targets 1 and 2 as well as targets 3 and 4 are located at the same range to the flight path. It becomes apparent, that for each slant range of closest approach ($R_0 = R(\eta_0)$), a whole family of target trajectories are corrected [13]. That is, all targets with the same R_0 are corrected simultaneously. RCMC is a function of azimuth (Doppler)

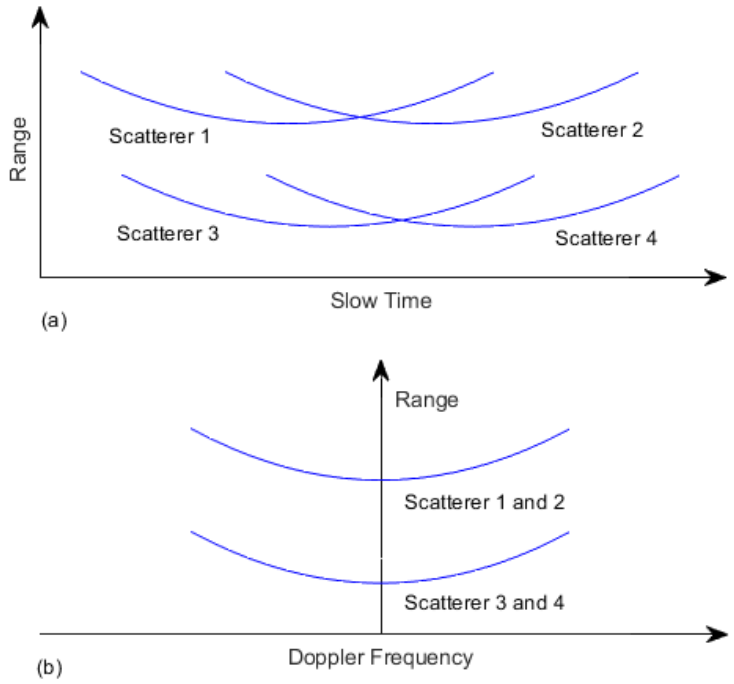

Figure 2.2.4: (a) Range migration in the range slow time domain. (b) Range migration in the range doppler domain [17].

frequency f_{D} and is done by shifting the samples according to Equation (2.2.3) [13].

$$\Delta R(f_{\mathrm{D}}) = \frac{\lambda^2 R_0 f_{\mathrm{D}}^2}{8 v_r^2}. \tag{2.2.3}$$

2.2.4 Azimuth Compression

Azimuth Compression is the process by which SAR data is focused in the along track dimension. The approach is very similar to range compression as the signal is convolved with a Matched Filter that consists of the complex conjugated time reversed Doppler signature of the SAR system. Since the data has already been transformed to range Doppler coordinates by the previous step, the filter can be applied conveniently by multiplication in the azimuth frequency domain. The matched filter can be analytically derived to [13]

$$H_{\mathrm{a}z}(f_{\mathrm{D}}) = \exp\left(-j\pi\frac{f_{\mathrm{D}}^2}{K_{\mathrm{a}}}\right) \tag{2.2.4}$$

The azimuth FM rate K_{a} is determined by the change in the Doppler frequency:

$$K_{\mathrm{a}} = \frac{2}{\lambda}\frac{d^2R(\eta)}{d\eta^2}\;|_{\eta=\eta_{\mathrm{c}}} = \frac{2v_{\mathrm{r}}^2\cos^3(\phi_{\mathrm{c}})}{\lambda R_0}, \tag{2.2.5}$$

where η_{c} is the Doppler Centroid, which refers to the instantaneous Doppler frequency at the moment the target crosses the middle of the antenna beam. For low squint angles ϕ_{c} Equation (2.2.5) can be reduced to:

$$K_{\mathrm{a}} \approx \frac{2v_{\mathrm{r}}^2}{\lambda R_0} \tag{2.2.6}$$

A detailed derivation of the azimuth matched filter equations is described by Cumming and Wong [13]. The matched filters used in the RDA are often designed in the time domain. Since the signal in azimuth is weighted by the antenna pattern a window approximating the azimuth beam pattern is applied to the Filter in order to match the shape of the data. The Doppler bandwidth is usually greater than needed to achieve approximately square pixels. Common ways to use this "surplus" resolution are pixel averaging or Multilooking. Multilooking is a technique where the spectrum is divided into non-overlapping sections called sublooks. Each sublook produces an uncorrelated copy of the full resolution image when transformed back to the time domain. By averaging sublooks or azimuth pixels, the "extra-bandwidth" can be used to trade off spatial resolution for reduced speckle noise.

2.3 Phased Array Antennas

Array antennas are configurations of several individual emitters in a geometrical order. If the spatial separation of the radiating elements is within distances on the order of the transmitted wavelength, their signals are combined in order to improve the performance over that of a single antenna. The electromagnetic waves of the individual radiators superpose coherently at each point in space so that their individual contributions add in the preferred direction and cancel in other directions. Even before they are combined into an array antenna, all electromagnetic emitters have directional

characteristics as opposed to radiating and receiving power equally in all directions. As depicted in Figure 2.3.1, illumination in the center of the SAR image is high but decreases to the edges in the range direction. This is caused by the directivity of the antenna in the elevation plane. The

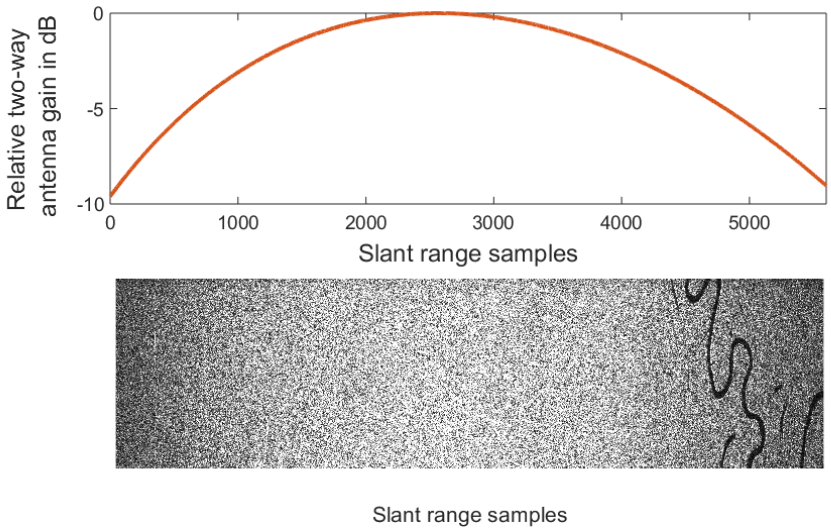

Figure 2.3.1: Antenna elevation pattern spanning over range.

directivity of an array at far zone is expressed by the directional pattern of one of its radiating elements and an array factor. The array factor $AF(\theta, \phi)$ describes the collective complex-valued far-field radiation pattern if all antenna elements in the array are replaced with isotropic radiators [18]:

$$AF(\theta, \phi) = \sum_{i=1}^{N} I_i \cdot e^{-j\psi_i} \cdot e^{j\beta x_i \cos\theta \sin\phi} \cdot e^{j\beta y_i \sin\theta} \cdot e^{j\beta z_i \cos\theta \sin\phi}. \tag{2.3.1}$$

Since in reality there are no isotropic radiators, the array factor must be multiplied by a radiating element factor in order to obtain the actual antenna far field pattern:

$$D_{\text{array}}(\theta, \phi) = AF(\theta, \phi) \cdot D_{\text{element}}(\theta, \phi). \tag{2.3.2}$$

Here, I_i and ψ_i are amplitude and phase of the i^{th} element's feed current, $\beta = 2\pi/\lambda$ is the wavenumber, and the vector $\vec{p_i} = (x_i, y_i, z_i)^T$ describes the location of the i^{th} element with respect to the origin. In the coordinate system used for equation (2.3.1), the positive elevation angle $+\theta$ tilts toward the +Y-axis in the elevation plane (Y-Z plane), the positive azimuth angle $+\phi$ is defined toward the +X-axis in the azimuth plane (X-Z plane) and the +Z-direction is normal to the antenna aperture on the radiation side. The definition is also shown in Figure 2.3.3. To steer the beam in the direction of (θ, ϕ), the phase of the supply currents must satisfy the equation

$$\psi_i = -\beta \vec{p_i} \cdot \begin{pmatrix} \cos\theta \sin\phi \\ \sin\theta \\ \cos\theta \sin\phi \end{pmatrix}. \tag{2.3.3}$$

This is the principle of beam steering of a phased array. In addition, phase-shifters can be used to manipulate the shape of the antenna beam itself. By applying complex weights to the individual signals of the antenna elements, a variety of different beam patterns can be achieved. This is known as beamforming and generally aims to produce a narrow main beam with high gain at the center and low sidelobe levels in all other directions [18]. In the case of SIR-C, beams with various beam widths were created by purposefully spoiling the phase away from the phase relationship above. This practice was given the appropriate name of "beam spoiling" in the SIR-C documentation [19]. Additionally, the amplitude of the radiating elements can be tapered towards the edges of the array in order to adjust sidelobe heights. This however, comes at the expense of a broader main beam and consequently a lower antenna gain. The compromise is determined by the tapering function. In SIR-C, amplitude tapering is achieved by the distribution network, depicted in Figure 2.3.2. On top of that, the antenna has individual power amplifiers (Transmit Receive Modules). These T/R modules are a distinguishing feature of active antennas, in contrast to the traditionally passive antenna which does not provide additional signal amplification [20].

2.3.1 The SIR-C Active Phased Array Antenna

SIR-C was the first dual frequency spaceborne imaging sensor with simultaneous quad polarization capability. The system was composed of two single frequency synthetic aperture radars which allowed for up to eight different measurements at the same time [4]. L-band ($24.038\,\mathrm{cm}$ center wavelength) and C-band ($5.664\,\mathrm{cm}$ center wavelength):

- horizontal transmit-horizontal receive (HH),
- horizontal transmit-vertical receive (HV),
- vertical transmit-horizontal receive (VH),
- and vertical transmit-vertical receive (VV).

The system was designed with user configurability, in that prior to each datatake the system ressources could be reconfigured to best support a particular acquisition mode or manage shuttle power consumption. The options in configuring the system included frequency and polarization selection (mode), transmit pulse width, antenna beamwidth and system resolution (three selectable bandwidths of $10\,\mathrm{MHz}$, $20\,\mathrm{MHz}$ and $40\,\mathrm{MHz}$). Both L- and C-band antennas are part of a planar active phase array with dimensions of $12\,\mathrm{m}$ in flight direction and $3.7\,\mathrm{m}$ in cross track. The width in cross track is split between L and C band antenna proportional to their wavelengths [2]. The Space Radar Laboratory payload also employed an X-SAR slotted waveguide antenna, further reference to which, however, will not be made here. Further details about the antenna system are listed in Table 2.3.1. The SIR-C antenna was installed in the space shuttle cargo bay at an angle of $14°$ mechanical tilt. Together with the nominal roll angle of $206°$, this translates into a $40°$ look angle (off-nadir) for the antenna boresight, prior to any electronic steering. Each array was composed of 18 panels that

are arranged in a 9 by 2 pattern for L-band and in a 18 by 1 layout for C- band (Fig. 2.3.3 and Fig. 3.3.3). In azimuth direction (along flight), both antennas are divided into three sections, historically called outer leaf, center leaf and inner leaf. Each leaf consists of six panels, which in turn contain a uniform grid of dual- polarized microstrip antenna radiators. The L-band panels are comprised of 6 by 9 elements, while the C-band panels have 18 by 18 elements. Each row of these radiators in a panel forms a unit called a stick, and can be independently controlled. A stick has two feed points, one for vertical polarization excitation and the other for horizontal excitation. As illustrated in Figure 2.3.2 every feed is equipped with its own phase shifter, followed by a Transmit/Receive (TR) module. There are 14 TR- modules for every 18 sticks, each of which consists of a low noise amplifier for receiving and a high power amplifier for transmission [20]. The L-band antenna is comprised of an array of nine sticks in the along-track direction and 18 sticks in the cross-track direction. The C-band antenna has 18 sticks each in azimuth and elevation. By controlling the relative phase of signals from each element, both antennas are able to manipulate the beam width electronically (phase weighting/phase spoiling) or to steer the beam in a specific direction. This layout means that the collective far field pattern of all radiating elements is determined by a matrix of 9x18 phase shifter values in L-band and 18x18 values for the C-band array. Electronic steering enables off-broadside angles between ±23° in elevation, resulting in (off-nadir) look angles between $17°$ and $63°$. Additional roll maneuvering of the space shuttle can extend this range, if higher (or lower) look angles are needed.

2.4 Datatakes

SIR-C data is acquired at a nominal altitude of $215\,\mathrm{km}$ $\pm 25\,\mathrm{km}$, with swath widths varying from 15 to $90\,\mathrm{km}$, depending on the radar mode used to collect the data. The swath velocity is approximately $7.5\,\mathrm{km\,s^{-1}}$ [22]. Acquisitions are organized into so called "datatakes", which lasted anywhere between 1 minute and 25 minutes. The datatake ID is indicated by xxx.yy, where "xxx" represents the orbit number and "yy" the datatake sequence number within an orbit. Datatakes are processed into single-look complex (SLC) and multi-look complex (MLC) products by the imaging algorithm. A standard SLC produced by the current SIR-C processor prototype is composed of 21000 radar pulses.

2.5 Radar Backscatter Conventions

The radar backscatter β describes the ability of a single discrete scatterer to reflect the signal energy back towards the sensor. It is defined as the ratio between the scattered power density S_s and incident power density S_i

$$\beta = 4\pi R^2 \frac{S_\mathrm{s}}{S_\mathrm{i}}. \tag{2.5.1}$$

Parameter	**L-band** (1250 MHz)	**C-band** (5300 MHz)
Aperture Length	12 m	12 m
Aperture Width	2.9 m	0.7 m
Array Element Spacing (el.)	16.18 cm	3.94 cm
Array Element Spacing (az.)	134 cm	67 cm
Antenna Gain	36.4 dB	42.7 dB
Electronic Sterring Range	±23°	±23°
Elevation Beamwidth	5° to 16°	5° to 16°
Azimuth Beamwidth	1°	0.25°
Peak Radiate Power	4400 W	1200 W
Slant Range Resolution (10 MHz)	14.9 ±2.9 m	14.5 ±2.8 m
Slant Range Resolution (20 MHz)	8.3 ±0.3 m	7.9 ±0.3 m
Azimuth Range Resolution (10 MHz)	7.6 ±0.9 m	7.7 ±0.8 m
Azimuth Range Resolution (20 MHz)	8 ±1.1 m	8 ±1.1 m
Maximum Look Angle Degrees	>60°	>60°
Swath Width	15 to 160 km	15 to >160 km
Orbit Characteristics		
Nominal Altitude:	215±25 km	
Eccentricity:	≤ 0.002°	
Inclination:	57°	
Attitude Measurement Error (3σ)		
Pitch:	±1.784°	
Yaw:	±1.43°	
Roll:	±1.24°	
Attitude Drift Rate Error (3σ)		
Pitch:	±0.03 °/ sec	
Yaw:	±0.03 °/ sec	
Roll:	±0.03 °/ sec	
Radar Characteristics		
Pulse bandwidth:	10 MHz, 20 MHz	
Pulse duration:	33.8 µs, 16.9 µs, 8.44 µs	
Sampling rate:	45 MHz, 22.5 MHz	
PRF:	1344 Hz, 1395 Hz, 1440 Hz, 1488 Hz, 1512 Hz, 1620 Hz, 1647 Hz, 1736 Hz	

Table 2.3.1: SIR-C orbit characteristics and radar specifications [2, 4, 21].

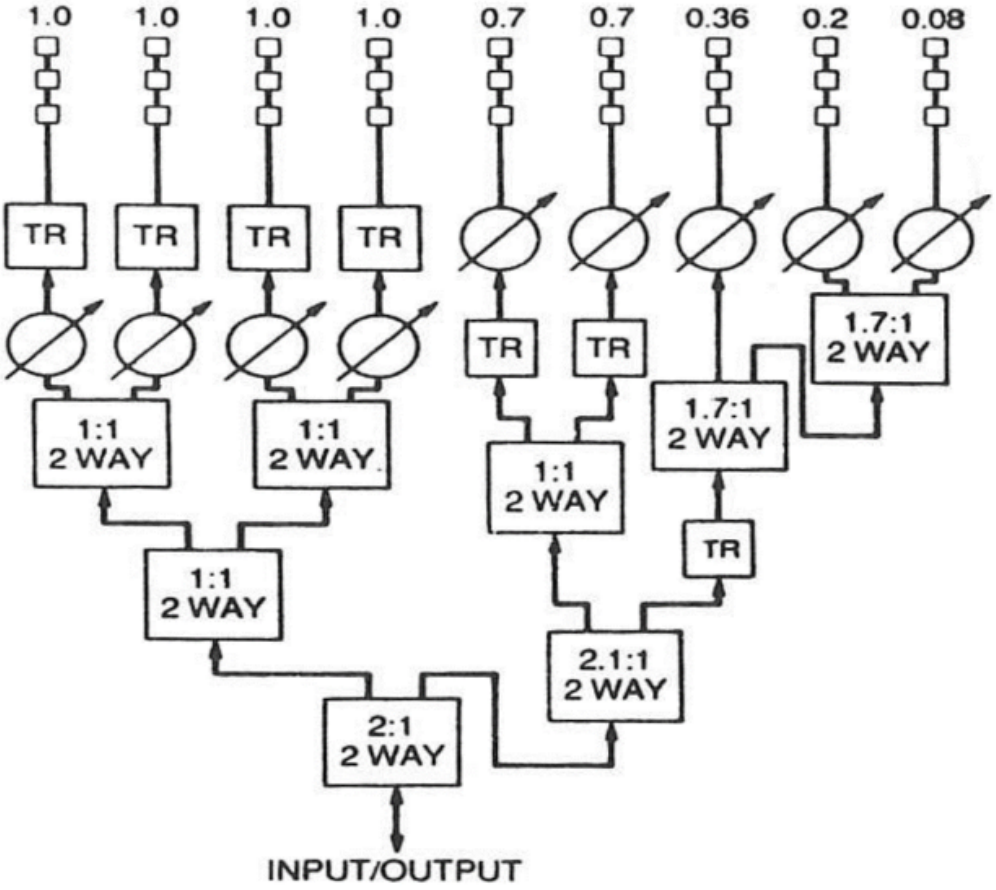

Figure 2.3.2: SIR-C antenna feed system with TR-modules and phase-shifters: Half of the symmetrical design (Image Credit: Jet Propulsion Laboratory [20]).

The term $4\pi R^2$ refers to the cross sectional area, a perfectly isotropic reflecting sphere would need in order to produce a radar response signal of equal strength. When the Radar response is extended from a single discrete scatterer to natural terrain, the radar reflectivity is expressed as a backscatter ratio estimate per reference area [9, 23, 24]. Three SAR conventions have been established to describe radar reflectivity arising from distributed surfaces:
"Beta nought" β^0, or "radar brightness", is the reflectivity normalized with respect to the pixel area A_β in the slant range plane. If the SAR image pixel is in slant range and azimuth coordinates, then β^0 is the observed mean radar reflectivity per pixel. This normalization provides the most natural radar observable [24] since the reference area is determined only by the characteristics of the SAR system. In contrast to other conventions, beta nought does not rely on knowledge of the local incidence angle [24].

$$\beta^0 = \frac{\beta}{A_\beta}. \tag{2.5.2}$$

"Sigma nought" σ^0, or normalized radar cross section, is defined as

$$\sigma^0_{\mathrm{E}} = \frac{\beta}{A_\sigma} = \beta^0 \frac{A_\beta}{A_\sigma} = \beta^0 \sin(\alpha_{\mathrm{E}}), \tag{2.5.3}$$

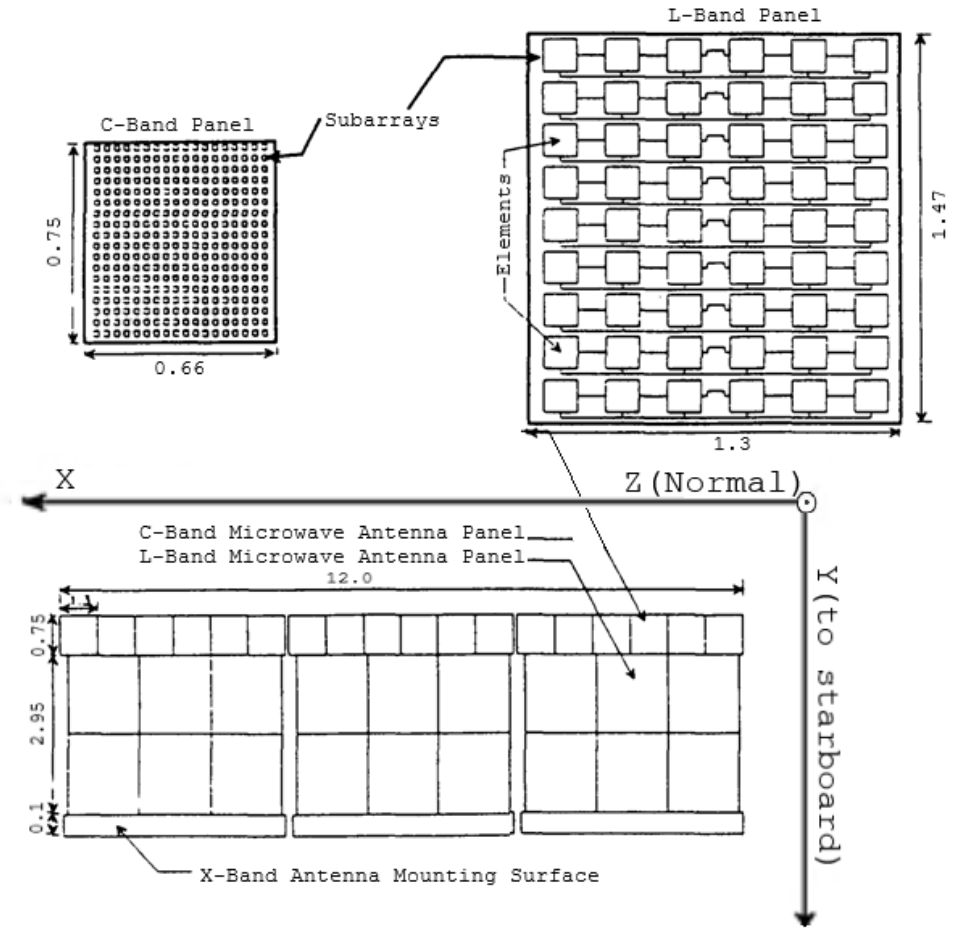

Figure 2.3.3: SIR-C antenna layout (Image Credit: Jet Propulsion Laboratory [2]).

where α_{E} is the local incidence angle and the subscript E denotes an ellipsoidal model of the ground [23]. As illustrated in Figure 2.5.1, the reference area A_σ is locally tangent to the ground, i.e. a resolution cell in ground range coordinates.
If the reference area is perpendicular to the direction of incidence the resulting normalization is *"gamma nought"* γ^0 (see Fig. 2.5.1)

$$\gamma^0_{\mathrm{E}} = \frac{\beta}{A_\gamma} = \beta^0 \frac{A_\beta}{A_\gamma} = \beta^0 \tan(\alpha_{\mathrm{E}}). \tag{2.5.4}$$

The conventions σ^0 and γ^0 require a model of the Earth's surface since their definitions include the local incidence angle. Usually the Earth is modeled as an ellipsoid according to the following equation:

$$\frac{x^2 + y^2}{R_{\mathrm{e}}^2} + \frac{z^2}{R_{\mathrm{p}}^2} = 1. \tag{2.5.5}$$

The original SIR-C processor used the Clarke 1866 oblate ellipsoid model, which is given by

$$R_{\mathrm{e}} = 6\,378\,206.4\,\mathrm{m},$$

and

$$R_{\mathrm{p}} = 6\,356\,583.8\,\mathrm{m}.$$

The x, y, z coordinates are of the rotating Greenwich true of date coordinate system [25], which is defined as follows:

Origin: The center of the Earth

XY-plane: The Earth's true of date equator

X-axis: Directed towards the prime meridian

Z-axis: Directed along the Earth's true of date rotational axis and is positive north

Y-axis: Completes a right-handed coordinate system

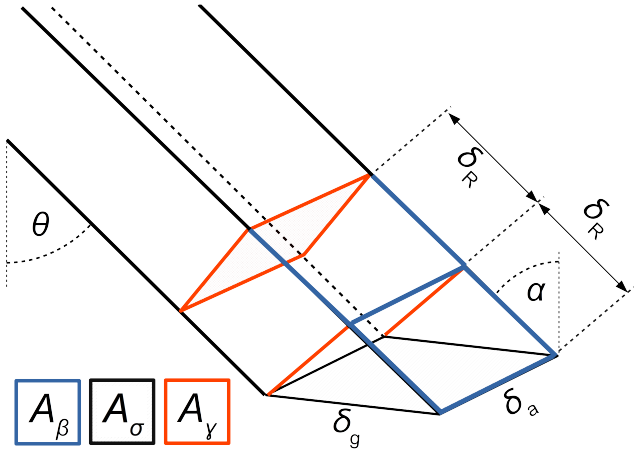

Figure 2.5.1: Normalization areas for SAR backscatter.

2.6 SAR Radar Equation

The radar equation for the signal to noise ratio of a monostatic radar system can be written as

$$\mathrm{SNR} = \frac{P_{\mathrm{t}} \int [G_{\mathrm{t}}(\theta,\phi)\sigma^0(\theta,\phi)A_{\mathrm{e}}(\theta,\phi)/(4\pi R^2)^2]\,\mathrm{d}A}{FkTB_{\mathrm{n}}}, \tag{2.6.1}$$

with the integral taken over the footprint of the radar beam and

P_{t}: The power radiated by the antenna

$G_{\mathrm{t}}(\theta, \phi)$: Directional gain for a transmitting antenna

$\sigma^0(\theta, \phi)$: Backscatter coefficient

R: Distance from the radar to the target

F: Operating noise factor

k: Boltzmann's constant

T: Total source of equivalent noise temperature at the radar carrier frequency

B_{n}: Equivalent noise bandwidth

$A_{\mathrm{e}}(\theta, \phi)$: Effective receiver aperture

The effective receiver aperture is usually written as

$$A_{\mathrm{e}} = \frac{G_{\mathrm{r}} \lambda^2}{4\pi}, \tag{2.6.2}$$

for the carrier wavelength λ. Equation (2.6.1) can be simplified according to [14], if the SNR is considered for a single SAR resolution cell $\delta_{\mathrm{a}} \delta R_{\mathrm{g}}$ with isotropic mean backsatter σ^0. The gain $G_{\mathrm{t}}(\theta, \phi)$ is taken as constant across δR_{g} and the (single pulse) radar equation becomes:

$$\mathrm{SNR}_0 = \frac{P_{\mathrm{t}} \lambda^2 G_{\mathrm{t}} G_{\mathrm{r}} \sigma^0 \delta_{\mathrm{a}} \delta R_{\mathrm{g}}}{(4\pi)^3 R^4 F k T B_{\mathrm{n}}}. \tag{2.6.3}$$

The same terrain element $\delta \mathrm{a} \delta R_{\mathrm{g}}$ is sampled by N_{A} different pulses before it leaves the radar beam again. The envelope of each pulse is sampled another $N_{\mathrm{R}} = \tau_{\mathrm{p}} f_{\mathrm{s}}$ times, producing a total of $N_{\mathrm{i}} = N_{\mathrm{A}} N_{\mathrm{R}}$ data samples. To create a single focused resolution cell, all of these samples are processed coherently by the image formation algorithm, hence improving the SNR to

$$\mathrm{SNR}^{\mathrm{I}} = N_0 \cdot \mathrm{SNR}_0. \tag{2.6.4}$$

The azimuth samples can be expressed as

$$N_{\mathrm{A}} = \mathrm{PRF} \cdot t_{\mathrm{A}} = \mathrm{PRF} \cdot \frac{0.886 R \lambda}{L_{\mathrm{a}} v_{\mathrm{g}}}, \tag{2.6.5}$$

where t_{A} is the time a given terrain point is in view of the radar and v_{g} is the speed of the radar footprint on the ground. The factor 0.886, which is a guide value to calculate the 3dB beamwidth of an aperture antenna, will subsequently be rounded to one. This is a valid approximation since the relevant swath width usually extents well beyond the 3dB limits of the antenna beam. The range samples can be written as

$$N_{\mathrm{R}} = f_{\mathrm{s}} \tau_{\mathrm{p}} = B_{\mathrm{R}} \tau_{\mathrm{p}} \approx B_{\mathrm{n}} \tau_{\mathrm{p}}, \tag{2.6.6}$$

where B_{R} is the pulse bandwidth. If eq. (2.6.6) is substituted with the average power over an entire transmit-receive-cycle $P_{\mathrm{ave}} = P_{\mathrm{t}} \cdot \mathrm{PRF} \cdot \tau_{\mathrm{p}}$, the expression appears as

$$N_{\mathrm{R}} = B_{\mathrm{n}} \frac{P_{\mathrm{ave}}}{P_{\mathrm{t}} \mathrm{PRF}}. \tag{2.6.7}$$

With $\delta_{\mathrm{a}} = L_{\mathrm{a}}/2$ (see Section 2.1.2), the total number of samples N_{I} per resolution cell becomes

$$N_{\mathrm{I}} = \frac{B_{\mathrm{n}} P_{\mathrm{ave}} R \lambda}{P_{\mathrm{t}} 2 v_{\mathrm{g}} \delta x}, \tag{2.6.8}$$

Substitution of Equation (2.6.8) into Equation (2.6.4) finally results in the SAR radar equation for average signal to noise ratio of a SAR image point [14]:

$$\mathrm{SNR}^{\mathrm{I}} = \frac{P_{\mathrm{ave}} \lambda^3 G_{\mathrm{t}} G_{\mathrm{r}} \sigma^0 \delta R_{\mathrm{g}}}{2(4\pi R)^3 v_{\mathrm{g}} F k T}. \tag{2.6.9}$$

2.7 Radiometric Calibration

Radiometric calibration provides the means for relating the SAR image pixel numbers directly to the radar cross section (RCS) or a radar backscatter coefficient ($\beta^0, \sigma^0, \gamma^0$), respectively, for point targets and distributed targets. This is essential for the quantitative use of the pixel information present in SAR imagery [26]. While early acquisitions focused mainly on qualitative information for reconnaissance and target detection, the modern applications tend to stress the measurement aspect of SAR for derivation of geophysical parameters [9]. The number of applications for SAR as a remote sensing tool has rapidly expanded into fields like oceanography, forestry, agriculture, climate change research, environmental monitoring, 2-D and 3-D mapping, change detection and planetary exploration [12]. Next to the measurement aspect, radiometric calibration is also the prerequisite for proper comparison between images acquired with different SAR sensors. The general calibration process in the case of SIR-C hast 3 steps: Radiometric Correction, Polarimetric Calibration and absolute calibration [11, 27, 4]. The JPL calibration requirements are given in Table 2.7.1.

Radiometric Correction, or Normalization, refers to the compensation of relative radiometric effects inherent to the system. SAR data usually has substantial variation in the range direction caused by several factors [13]. First, there are relative effects due to the antenna directivity pattern and other electronic radar subsystems. The various contributions to overall radar gain include thermal drifts in amplifiers and phase shifters, losses in cables etc. Second, atmospheric and ionospheric effects. Finally, there are geometrical considerations such as the $1/R^4$ law[1] and the term $1/\sin(\alpha)$, which accounts for the change in the illuminated ground area as a function of the

[1] In the case of processed SAR Images the signal strength is proportional to $1/R^3$ rather than $1/R^4$ (see Sec. 2.6)

incidence angle α (conversion to normalized radar cross section, see Sec.2.5). Once an estimate of the above factors is obtained as a function of range, a radiometric correction vector is applied to the measured radar signal. In SIR-C, this is done in the post processing stage, i.e. the correction vector is applied to the full-resolution complex image data [28].

Multichannel sensors require additional *polarimetric calibration*, as the cross talk between polarization and or frequency channels introduces further uncertainty to the signal. The measured signal response (voltage) of a target can be described as the complex matrix

$$\mathbf{Z} = \mathbf{RST} + \mathbf{N}, \tag{2.7.1}$$

where **S** is the scattering matrix distorted by the radar receive and transmit systems **R** and **T**; **N** is an additive noise term [14].

- According to the reciprocity theorem, the scattering matrix **S** is symmetric, in that, HV and VH observations should be equal. Thus, the next step for quad-pol data is symmetrization of the HV and VH channels. The symmetrization parameters are estimates for the channel balance between HV and VH measurements [13].

- The HH and VV channels are balanced in amplitude and phase. The channel-to-channel amplitude and phase imbalance is the uncertainty in the estimate of backscatte-coefficient-ratio and phase difference respectively, between two image pixels from two different polarization images [14].

Absolute Calibration is characterized by the uncertainty in the estimate of the backscatter coefficient from an image pixel as a result of system induced errors [11]. In the context of SAR, the calibration process is often divided into two categories:

- Internal calibration refers to the measurement and subsequent compensation of the various losses and gains in the different radar subsystems, using injected calibration tone signals injected into the data stream by built in devices [14].

- External calibration involves the comparison of the radar response from unknown targets with the known responses from several calibration targets. A general distinction can be made between techniques based on point targets and methods that use distributed calibration targets with known backscatter characteristics. The two types of point targets used for SIR-C were passive trihedral corner reflectors and Polarimetric Active Radar Calibrators (PARCs) [29]. A popular calibration site for distributed targets is the amazonian rain forest (see Sec. 4.1.1)

Through absolute calibration, the gray-scale values in SAR images are converted from being qualitatively representative of the signal to being quantitatively representative of radar backscatter value. It is only at this point that meaningful comparison between targets imaged with different

SAR sensors is possible.

Absolute calibration	±3.0 dB
Cross-swath calibration	±1.0 dB
Amplitude imbalance	±0.4 dB
Phase imbalance	±10°
Cross-talk	<-30 dB

Table 2.7.1: Calibration goals for SIR-C data [4].

2.7.1 Calibration of SIR-C Data

Calibration of SIR-C image data presented several challenges The SIR-C radar image data presented several challenging problems from a calibration standpoint. A more detailed review of the following aspects can be found in [28].

- SIR-C was the first multi-frequency, multi-polarization sensor in space to acquire eight different measurements simultaneously.
- SIR-C was configured in many different data acquisition modes, which were combinations of the available frequencies, polarizations, pulse bandwidths pulse lengths, and pulse repetition frequencies.
- The radar is an electronically steered, active phased array antenna. Since different electronic elements were used for transmit and receive, the array is not necessarily reciprocal like a passive antenna.
- The characteristics of the electronic antenna elements, in particular the amplifiers for transmit and receive, showed the tendency to drift with temperature.
- The antenna provided a challenge for radiometric correction as it was programmed to electronically steer to 256 different beam positions, over a range of 20 degrees in elevation and used eight different phase weighting functions in order to create various beamwidths.

According to [28] the gain K_s imposed by the radar on the backscatter can be described as follows:

$$K_\mathrm{s} = \frac{P_\mathrm{t} G_\mathrm{t}^\mathrm{A}(\theta,\phi) G_\mathrm{r}^\mathrm{A}(\theta,\phi) \lambda^2 G_\mathrm{r}^\mathrm{E} G_\mathrm{p}(x,y)}{(4\pi)^3 R^4 L_\mathrm{s} L_\mathrm{a}}, \tag{2.7.2}$$

where P_t is the transmission power, $G_\mathrm{t}^\mathrm{A}(\theta,\phi)$ and $G_\mathrm{r}^\mathrm{A}(\theta,\phi)$ are the antenna gains on transmit and receive as a function of elevation and azimuth angle θ,ϕ; G_r^E is the electronic gain; $G_\mathrm{p}(x,y)$ is the processor gain at for the pixel location x,y in the SAR image; L_a and L_s are loss terms for

signal attenuation due to propagation through system components (cables etc.) and the atmosphere. R is the range delay (which is corrected independently). In the SIR-C calibration report [4] the variations of K_s, in the along-track dimension were deemed negligible, so that only the range-dependent terms need to be corrected. This leaves the Antenna Gain Pattern (AGP) $G_{\mathrm{t}}^{\mathrm{A}}(\theta)G_{\mathrm{r}}^{\mathrm{A}}(\theta)$ as the largest sources of relative cross-swath calibration uncertainty. All remaining terms in equation (2.7.2) are constant across range and can be corrected independently.

3 SIR-C Antenna Model

In this chapter the equations are presented, which determine the radiation patterns for each frequency band and polarization channel. First, some background is provided, to establish the motivation behind the general approach. Subsequently, the steps required to obtain the phase values are presented and an algorithm of implementing the 4-bit phase-shifter control is given.

3.1 Background

Antenna pattern correction is a central part of the calibration effort and poses a particularly intricate problem in the case of SIR-C. Over the course of the two SRL missions, two active phased arrays acquired polarimetric L- and C-band data at a wide range of incidence angles and swath widths. This level of variability requires an accurate model of the system and extensive analysis of data from multiple calibration sites. The original Antenna Pattern Generation Software (APGS) was devised by then JPL-Engineer Yunjin Kim and combined five data files to calculate the antenna pattern [30]:

- The Antenna State Matrix contained the on/off settings for all amplifiers, and phase shifter bits over the entire mission.
- The Device Failure Map contained status information about device failure for all amplifiers and phase shifters in the antenna array.
- The Antenna Temperature Profile was a record of the estimated antenna temperature.
- The Stick Current Test Data file contained the measured current profiles over each stick in the antenna array.
- The Phase Shifter Test Data file contained the measured phase shift verses the commanded phase shift for each phase shifter bit.

According to the SIR-C calibration report [4], the APGS achieved excellent results, reducing the residual relative cross track uncertainty well below the stated goal of $\pm 1\,\mathrm{dB}$. However, this software and many of the pertinent data records have since been lost when the old SIR-C Ground Data Processing System became inoperable in 2005 [7]. Coupled with the issues described in Section 1.3 these circumstances conspire to make exact replication impossible. Hence, a number

of different approaches were pursued to implement a model capable of recreating these original results as close as possible.

Initially, the actual in-flight elevation patterns were estimated from large uniformly distributed targets from the amazonian rain forest. The idea was to create a comprehensive database, that contains every deployed antenna beam, along with a look up table for all datatakes. This approach failed mainly due to the fact, that there is a virtually endless number of SIR-C antenna configurations but only very limited availability of rain forest scenes. On top of that, the screening for suitable image candidates was unreasonably time consuming. Even with software solutions screening for- and download of suitable scenes would have taken up several weeks, given that the the volume of the SIR-C data collection exceeds $93\,\mathrm{Tbit}$ for the unprocessed binary files alone. A different methodology was necessary. After ASF received additional JPL-Documentation that outlined the equations used in the original antenna model [31, 19, 32], a similar mathematical approach was adopted.

3.2 Antenna Gain Pattern

The radiation patterns observed in the SIR-C SAR images depend on:

1. Frequency band: Usage of the L-band or C-band active phased array antenna.
2. Beam forming (Phase shifter values):

   Beam spoiling

   Beam steering
3. Polarization: HH, HV, VH, VV.
4. Receive- or transmit-pattern.
5. In terms of the antenna model: Ideal values vs. experimentally obtained probe data (phase shifts, current distribution across the radiation elements, transmit/receive-power).

Modeling of the Antenna Gain pattern involved some unique technical difficulties given the complexity of the radar system. The core of the antenna pattern generation is the calculation of the phase shifter values based on [31, 19], using real phase measurements recovered from a JPL-internal probe test report [32]. If not modeled properly, electronic beamforming, in which a phase weighting is applied across the aperture to change the beam direction and shape, results in large calibration errors. The SIR-C antenna had the ability to electronically steer to 256 beam positions over a range of ±23 degrees and to adjust the beamwidth between 5 to 16 degrees. [4]. A few

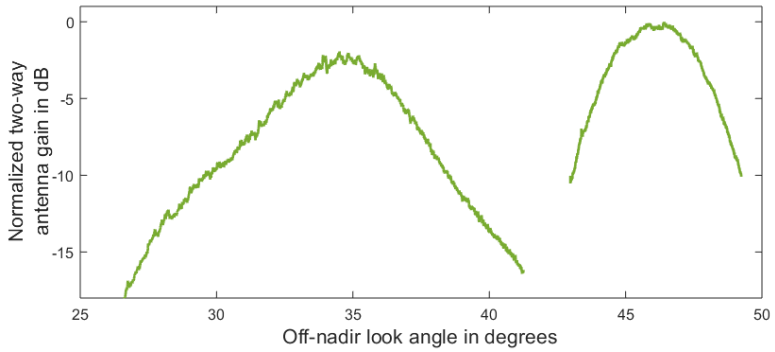

Figure 3.2.1: Measurements of two SIR-C antenna patterns in elevation (C-band, H-co-polarization, two-way). The right-hand pattern in the figure corresponds to the C-band H-polarized two-way pattern for $-5°$ beam steering and $150°$ beam spoiling. The left-hand pattern in the figure corresponds to the C-band H-polarized two-way pattern for $6.5°$ beam steering and no beam spoiling. The measurements were taken over the Amazon rain forest (see Chap. 4).

examples in Figure 3.4.2 demonstrate how much the beam patterns change between different data-takes. An example of two SIR-C measured in-flight antenna patterns is shown in Figure 3.2.1.

3.2.1 Phase spoiling

The main cause of the frequent changes observed in Figure 3.4.2 are changes in swath width due to the effects of electronic beam steering and phase spoiling. Phase spoiling is a beam forming technique for phased array antennas [33], where the in phase shifts between adjacent radiating elements are weighted to manipulate the shape of the antenna beam. In the context of this work, the term "beam spoiling" refers to phase weighting symmetric to mechanical boresight (change in beam width), while "electronic beam steering" is used to describe a change in direction without altering the beam width. Phase spoiling was used to achieve a more uniform antenna pattern for wide-swath data acquisitions. The L-band and C-band array of the SIR-C antennas employed a total of eight sine-weighted phase distributions to achieve different beam patterns (see Fig. 3.4.2). Expanding the beam width, comes at the expense of a lower antenna gain and consequently lower peak signal to noise ratio.

3.3 Antenna Phase Shifter Bits Calculation

As discussed in Section 2.3, the directivity of an array at far zone is expressed by the directional pattern of one of its radiating elements and an array factor.

$$D_{\text{array}}(\theta, \phi) = AF \cdot D_{\text{element}}(\theta, \phi) \tag{3.3.1}$$

For a planar array, such as the SIR-C antenna, the normalized array factor can be written as:

$$AF(\hat{r}) = \sum_{i=1}^{N} I_i \cdot e^{j\psi_i} e^{j\beta \vec{p}_i \cdot \hat{r}}, \tag{3.3.2}$$

where I_i and ψ_i are amplitude and phase of the i^{th} element's supply current, $\beta = 2\pi/\lambda$ is the wavenumber, $\hat{r}$ is the directional unit vector in spherical coordinates, and $\overrightarrow{p}_i$ is the vector describing the location of the i^{th} element with respect to the origin. The directional angles of the spherical coordinate system are consistent with the definition shown in Figures 3.3.3 and 4.1.4. The array factor is defined for a transmitting antenna, with the convention $E_{\text{h}}(r,t) = \hat{E}_{mrh} exp(j\omega t) exp(-j\beta R)$ for a time harmonic EM plane wave. The first exponent describes the time harmonic with angular frequency ω while the second exponent denotes spatial delay (negative phase) or advance (positive phase) as the wave traverses over the distance R [19]. To steer the beam in the direction $\hat{r}$, the phase of the supply currents must satisfy the equation

$$\psi_i = -\beta \vec{p}_i \cdot \hat{r}. \tag{3.3.3}$$

In addition to controlling the direction of the antenna beam, phase shifters can also be used to deliberately spoil the phase relationship in equation (3.3.3). Spoiling of the phase relationships lowers constructive interference between the radiating elements, effectively broadening the beam at the expense of peak antenna gain. Phase spoiling can be introduced to equation (3.3.2) as follows:

$$AF(\hat{r}) = \sum_{i=1}^{N} I_i \cdot e^{j\psi_i} \cdot e^{-j\Phi_i} e^{j\beta \vec{p}_i \cdot \hat{r}} \tag{3.3.4}$$

$$\psi_i = -\beta \vec{p}_i \cdot \hat{r} + \Phi_i. \tag{3.3.5}$$

The relation between unit vector $\hat{r}$ and the (steering) angles in azimuth ϕ and elevation θ is as follows:

$$\hat{r} = -\hat{x} \cos\theta \sin\phi + \hat{y} \sin\theta + \hat{z} \cos\theta \sin\phi, \tag{3.3.6}$$

where $\hat{x}$, $\hat{y}$ and $\hat{z}$ are the unit vectors of the cartesian coordinate system defined in Figure 3.3.3. The origin of the coordinate system is placed at the reference element of the antenna array under consideration (marked as "Ref" in Figure 3.3.3). Since the SIR-C antenna has equal-spaced

elements, the positional vector $\vec{p}_i$ can be expressed in cartesian coordinates as

$$\text{L-band: } \vec{p}_{\mathrm{l}}(m,n) = \hat{x} \cdot m \cdot d_{\mathrm{a,l}} - \hat{y} \cdot n \cdot d_{\mathrm{e,l}}; \tag{3.3.7}$$

$$\text{C-band: } \vec{p}_{\mathrm{c}}(m,n) = \hat{x} \cdot m \cdot d_{\mathrm{a,c}} + \hat{y} \cdot n \cdot d_{\mathrm{e,c}}, \tag{3.3.8}$$

Here, d_{a} and d_{e} represent the element spacing, while m and n denote the location of the elements in azimuth (X-axis) and elevation (Y-axis) respectively [19]. The phase spoiling term for SIR-C applies only to the elevation direction and is described by

$$\Phi_i = \Phi(n) = \frac{2\pi k}{360} \sin\left(\frac{\pi n}{17}\right) \tag{3.3.9}$$

Where k = 0,60,90,120,150,180,210,270 and n = 0....,17. With $\beta = \frac{360}{\lambda}$ the final phase shifter equations is obtained by substituting equations (3.3.6), (3.3.7) and (3.3.8) into the phase equation (3.3.5):

$$\text{L-band: } \psi_{\mathrm{l}}(m,n) = \frac{360}{\lambda_{\mathrm{l}}} m d_{\mathrm{a,l}} \cos(\theta)\sin(\phi) + \frac{360}{\lambda_{\mathrm{l}}} n d_{\mathrm{e,l}} \sin(\theta) + k \sin\left(\frac{\pi n}{17}\right) \tag{3.3.10}$$

$$\text{C-band: } \psi_{\mathrm{c}}(m,n) = \frac{360}{\lambda_{\mathrm{c}}} m d_{\mathrm{a,c}} \cos(\theta)\sin(\phi) - \frac{360}{\lambda_{\mathrm{c}}} n d_{\mathrm{e,c}} \sin(\theta) + k \sin\left(\frac{\pi n}{17}\right) \tag{3.3.11}$$

To obtain the far-field pattern of an array antenna, the array factor must be multiplied by a radiating element factor. In this case, a stick of the L-band or C-band array is considered a radiating element, since the sub-array comprising the stick is fed by a single phase shifter (see Sec. 2.3.1). The stick patterns (element factors) were obtained experimentally for each frequency, (L-band or C-band) in H- and V-polarization. The directional characteristics in azimuth and elevation are shown in Fig. 3.3.1 to Fig. 3.3.2. The stick patterns were measured using the SIR-C array as receiver. Since the sticks consist of a passive sub-array, the patterns are assumed to be reciprocal for receive and transmit mode. In contrast to the traditionally passive antenna, which does not provide additional signal amplification, reciprocity is not a valid assumption for active arrays. The difference between transmit and receive pattern is addressed in Section 3.4.1.

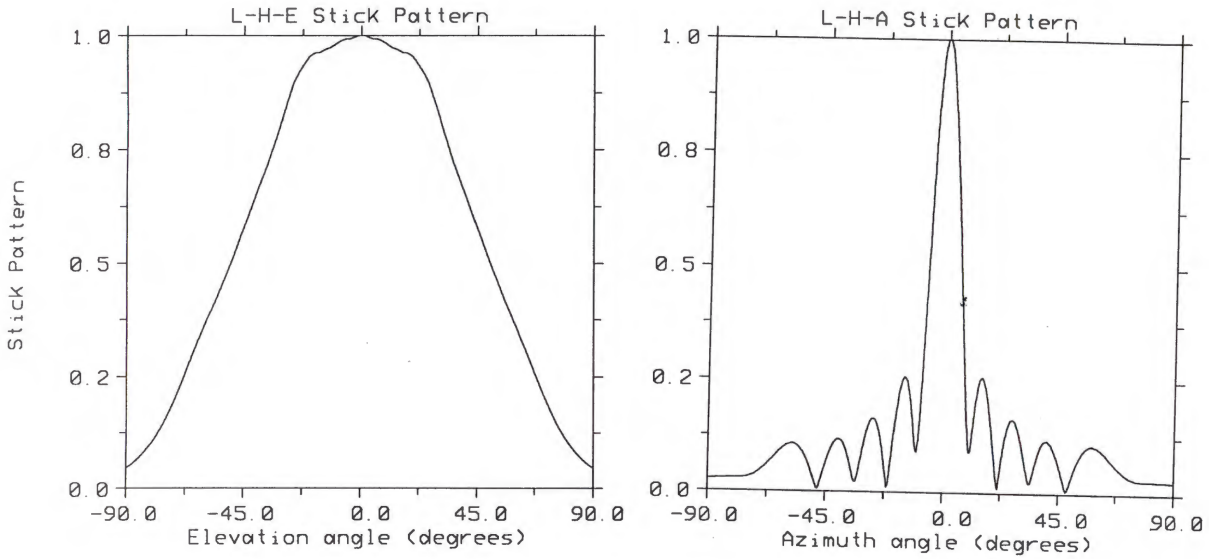

(a) Elevation and azimuth stick patterns of L-band horizontal polarization.

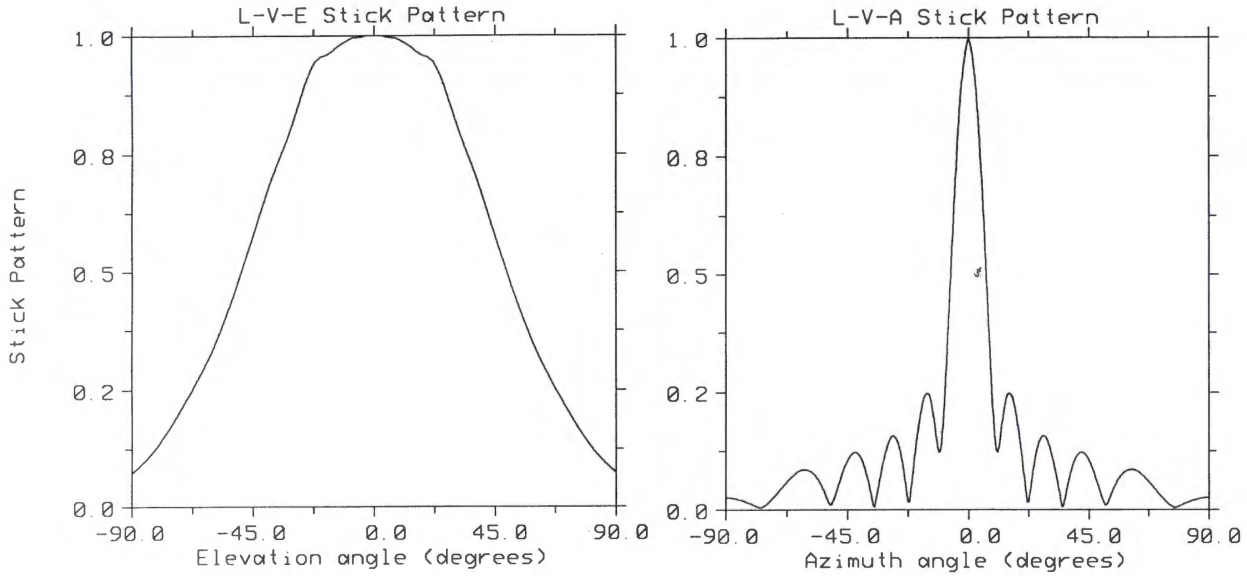

(b) Elevation and azimuth stick patterns of L-band vertical polarization.

Figure 3.3.1: SIR-C stick patterns L-band (relative antenna gain). Image credit: Jet Propulsion Laboratory [34].

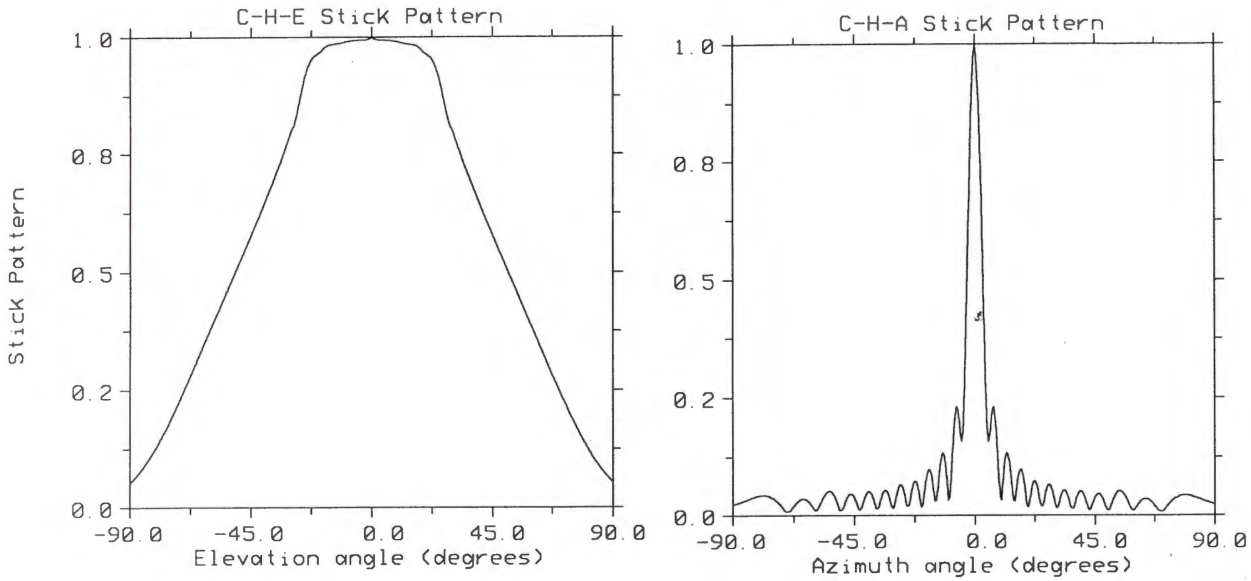

(a) Elevation and azimuth stick patterns of C-band horizontal polarization.

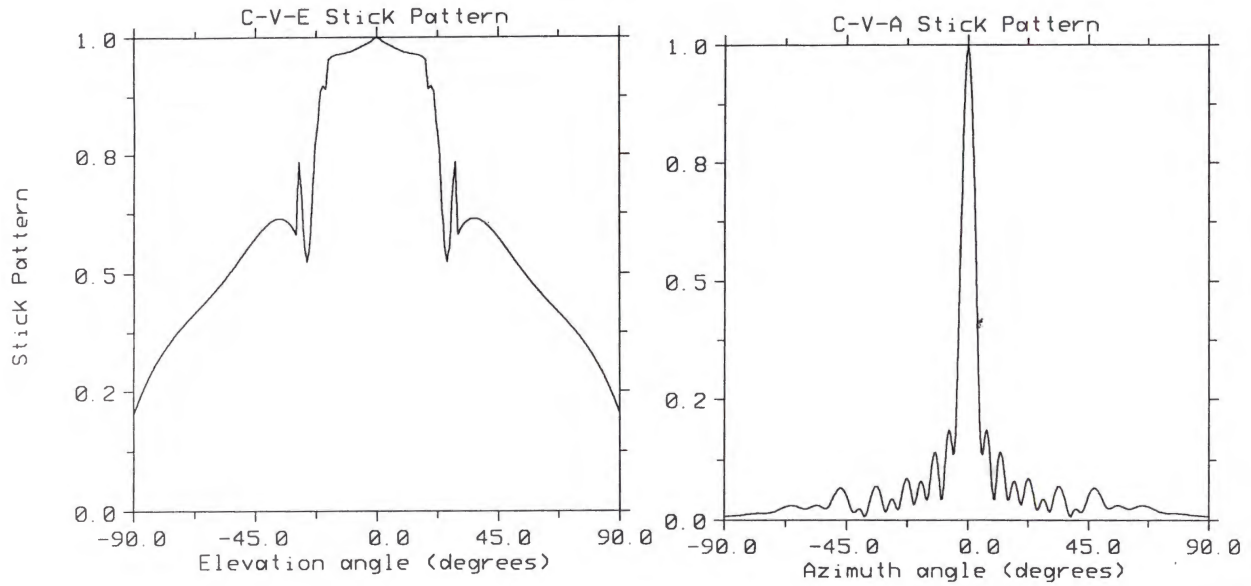

(b) Elevation and azimuth stick patterns of C-band vertical polarization.

Figure 3.3.2: SIR-C Stick patterns C-band (relative antenna gain). Image credit: Jet Propulsion Laboratory [34].

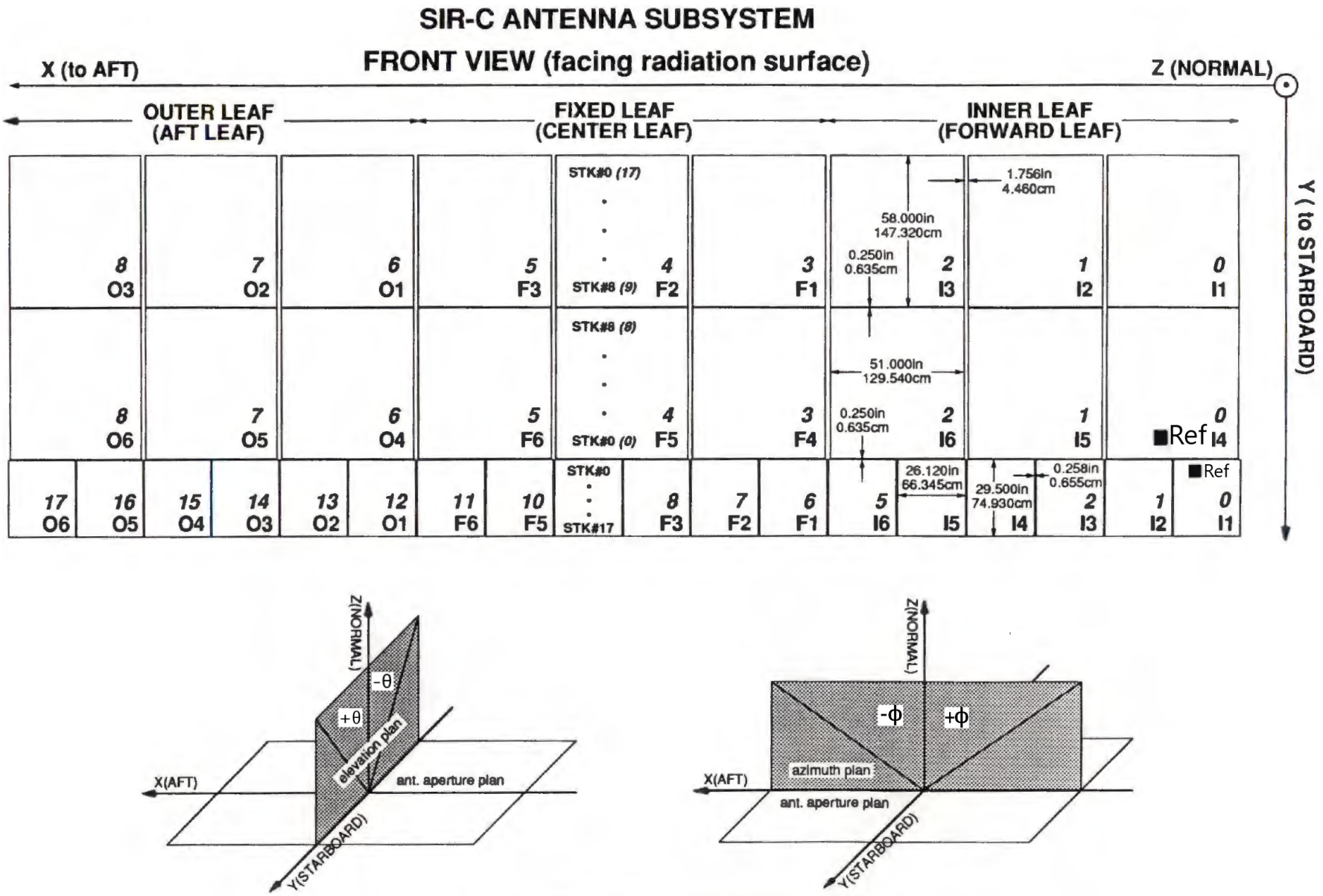

Figure 3.3.3: Antenna panel configuration and coordinate system definition for the L-band and C-band array antenna (Image Credit: Jet Propulsion Laboratory [20]).

3.4 Implementation

While the model is capable of producing 3D patterns (see Fig. 3.4.2), only the relevant two dimensional cross-section, that is the Y-Z-Elevation plane, will be discussed in this section. The key component of the antenna pattern generation algorithm (APGA), is the calculation of the phase shifter values for the L-band and C-band array sticks. The phase shifters are controlled by a 4-bit number (22.5° per bit), which is obtained by the following procedure [31, 19]:

1. The phase shifts for each radiation element are calculated according to equation (3.3.10). The results are stored in 16 bit integers, in which the four most significant bits after round-off are assigned as the bits for the phase shifter. Round-off to the next full 22.5° is done by subtracting 11.25° in binary.

2. The results obtained from equation (3.3.10) are the values by which the phase would need to be advanced in order to generate the desired antenna pattern. Since real phase shifters only provide delays, not advances, withing 0 and 360°, the results need to be converted according to equation (3.4.1), to achieve an equivalent relative phase difference between radiators.

$$\tilde{\psi}(m,n) = 360^\circ - \psi(m,n)_{360^\circ} \tag{3.4.1}$$

   Where $\psi(m,n)_{360}$ is the modulo(360)-operation. This entire procedure can be implemented by taking the 2's complement of the 16 bit integer.

3. Assign the 4 most significant bits to the phase shifter. The commanded phase shift is accordingly:

$$\tilde{\psi}(m,n) = 22\ 5^\circ \cdot \text{npsv}(1) + 45^\circ \cdot \text{npsv}(2) + 90^\circ \cdot \text{npsv}(3) + 180^\circ \cdot \text{npsv}(4) \tag{3.4.2}$$

   where npsv(i) are the bit values of the 4 bit phase shifter number.

3.4.1 Ideal Data vs. Test Data

Both L- and C-band arrays are composed of 18 panels that must all be in phase to form a beam. To verify that both L- and C-band arrays are able to steer the beam with the required accuracy, all phase shifters of the entire array were tested in a pre-flight campaign in 1993. In testing, each of the four bits commanding the phase-shifters was excited separately and the phase change was recorded using a probe. Table 3.4.1 shows an excerpt of the results. The full probe test report contains the phase shifts for all command bits in each phase shifter (C- and L-band H-pol. and V-pol.). The average value per bit is calculated from the entire array data and compiled in a formatted text file . These data are used by the APGA to calculate $\phi(m,n)$ according to equation (3.4.2), where the factors $22\ 5^\circ, 45^\circ, 90^\circ, 180^\circ$ are replaced by the probe measurements. Next to the phase shift

measurements the probe test report also details the measured current profiles over each stick in the antenna array. Like the phase-shifter data, the average amplitude and phase of the stick currents are accessed by the APGA to improve the calculation of the array factor. Stick current test data are available as a total of eight formatted text files (H-pol. and V-pol. -transmit, H-pol. and V-pol.-receive, for C-Band and L-band). Copies of these files and the complete phase-shifter performance tables are found in Appendix B. Figure 3.4.1 illustrates the difference between an ideal current profile and the average probe data amplitude measurements. Figure 3.4.3 shows how the usage of probe data improves the overall accuracy of the antenna model.
To conclude, the final antenna patterns are calculated by combining the probe data and the pre-measured stick patterns. That is, the array factor is calculated from the probe data and the stick locations for transmit and receive. Then, the array factors are multiplied by the stick pattern and subsequently added in decibels to yield the two-way antenna pattern. The APGA returns a two dimensional cross section of the full two-way directional characteristic. A selection of exemplary antenna patterns are shown in Figure 3.4.2. In the default case the pattern is obtained by cutting through the elevation plane, but other cross sections can be specified by the user.

Stick #	**L-band (probe)**	**L-band (command)**	**C-band (probe)**	**C-band (command)**
	[deg]	[deg]	[deg]	[deg]
0	1.07	0	-9.23	0
1	23.08	22.5	22.58	22.5
2	49.32	45	52.27	45
3	66.52	67.5	73.05	67.5
4	90.27	90	92.61	90
5	115.95	112.S	113.80	112.S
6	140.73	135	128.49	135
7	159.94	157.S	152.68	157.5
8	-175.19	180	170.48	180
9	-181.31	180	-147.21	-157.S
10	-156.05	-157.5	-130.43	-135
11	-131.89	-135	-109.44	-112.5
12	-114.04	-112.5	-89.36	-90
13	-94.00	-90	-61.64	-67.5
14	-66.47	-67.5	-45.82	-45
15	-40.73	-45	-30.02	-22.5
16	-23.81	-22.S	-7.01	0
17	-0.98	0	27.87	22.5

Table 3.4.1: Exemplary phase shift measurements of the first 16 sticks for a commanded steering angle of 5° in elevation. This data is a small excerpt from the full JPL probe test report [32]. A copy of the complete phase-shifter performance tables is included in Appendix B.

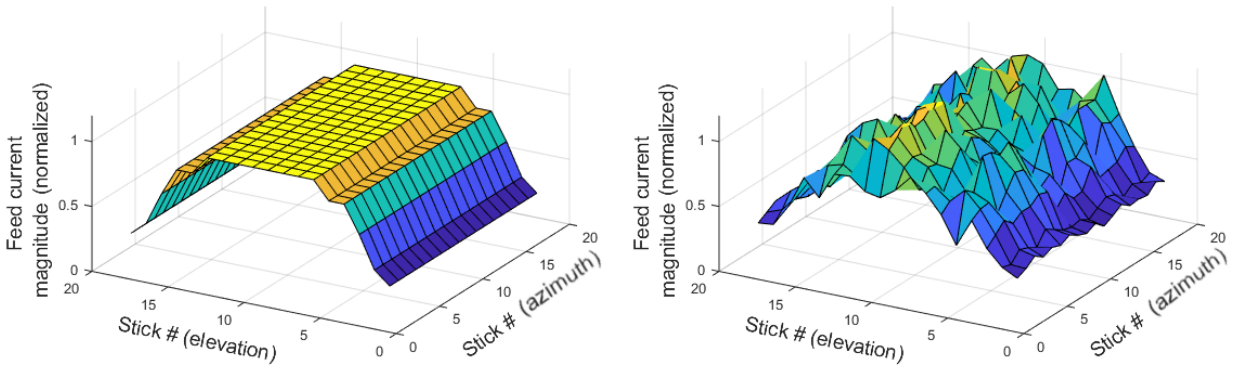

(a) Test data

(b) Ideal data

Figure 3.4.1: Normalized feed current distribution for C-band, transmit, H-polarization. (a): Nominal feed current amplitude values. (b): Measured feed current amplitude values.

Device Failure

Over the course of the SIR-C missions, defects in phase shifters, low noise amplifiers, high power amplifiers, and several other elements have caused failures in individual sticks of the array antenna. To adressed this problem the original SIR-C APG-Software accessed a Device Failure Map (DFM) that contained a failure time line for all amplifiers and phase-shifters in the antenna array. Device failures were determined by the original SIR-C calibration processor using different indicators such as temp/voltage/current data, roll null range line data, and distributed target analysis [30]. Failures of the transmit/receive amplifiers were characterized as complete failures of the particular device while phase-shifter failures were quantized to the individual bits of the command word.
At the time of this thesis, it is believed that the original DFM has been lost along with the SIR-C calibration processor. The effects of isolated device failures however, are expected to cause only minor degradation of the in-flight antenna pattern. Nevertheless, the current version of the APGA features a subroutine that takes complete device failures into account by setting the respective stick current to zero. To this end, the APGA reads the stick On/Off status from formatted text files for L- or C-band, polarization and receive/transmit-mode. If the pertinent information becomes available the aforementioned files can be updated accordingly (1: TR(n,m) working (default) , 0: TR(n,m) defective).

Thermal Drift

Pre-flight testing of the antenna revealed that the antenna gains for each polarization and frequency were a function of the antenna temperature [4]. During the SIR-C mission detailed temperature records were compiled to track the thermal drift of the active array amplifiers. Even though the antenna model includes a subroutine that compensates thermal drift based on pre-flight probe

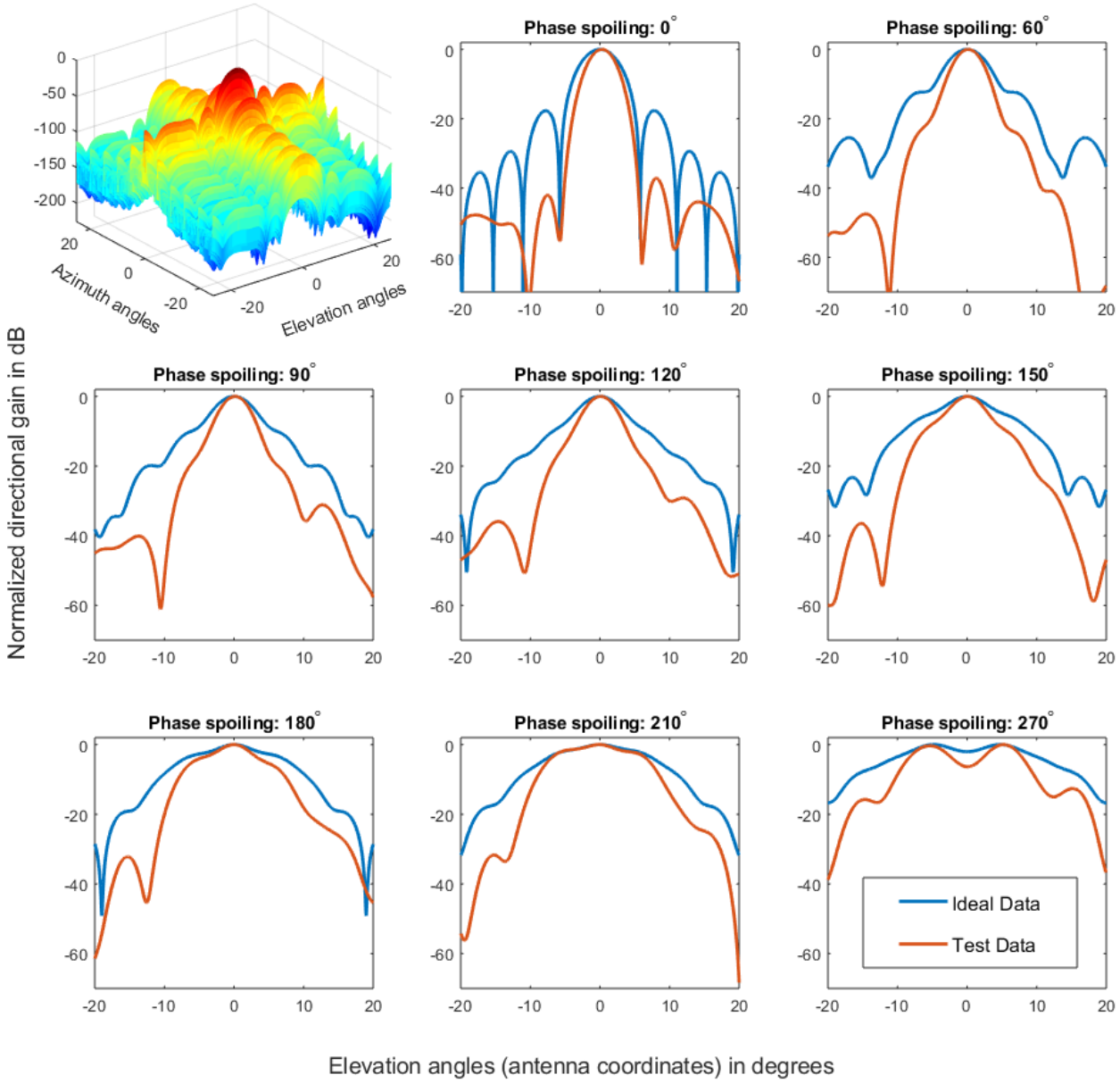

Figure 3.4.2: Exemplary antenna reference patterns in elevation for the C-band array in H-co-polarization mode. The Patterns were generated for a electronic steering angle of 0° with eight different beamspoiling numbers (amplitude of the phase weighting window). The blue lines represents the ideal antenna elevation patterns while the red lines were calculated with test data. The observed difference is due to the use of nominal vs. measured feed current amplitude and phase values.

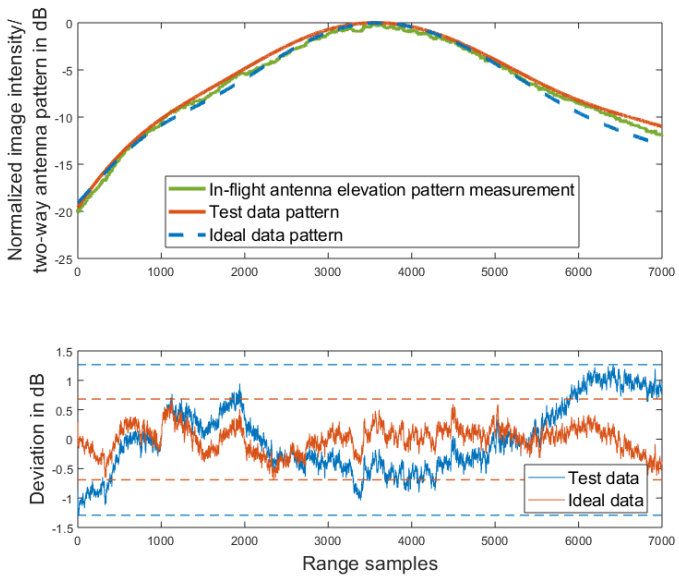

Figure 3.4.3: Plots of two SIR-C antenna model reference patterns (C-band, H-co-polarization, two-way). In the first plot, the pattern depicted by the red solid line corresponds to the C-band H-polarized two-way pattern calculated with data from the JPL-probe test report. The blue dashed line is the same pattern calculated with the nominal amplitude and phase values. The green curve represents a measurement of the SIR-C elevation pattern taken over the Amazon rain forest (see Chap. 4). The second plot shows the deviation between reference pattern and measurement for test data and ideal data, respectively, in red and blue. Using the test data pattern improves the maximum distance between pattern and range profile in a rain forest scene by ca. $0.2\,\mathrm{dB}$ on average.

data, the effects of temperature can be neglected in the context of Antenna Pattern Generation. This is due to the fact that only a single temperature reading is available per array, rather than a temperature map across the different TR-modules. Hence, the effects of temperature on the antenna pattern were considered in the original model by a scaling factor, that is constant across all TR-modules of the antenna. Since the current version of the APGA is only concerned with radiometric normalization. i. e. producing a normalized antenna gain pattern, a scalar has no effect on the final result. The temperature correction subroutine is relevant in the wider context of absolute the radiometric calibration.

4 Antenna Model Verification

This chapter describes the steps involved in deriving in-flight antenna patterns of SIR-C in order to verify the antenna model in elevation. The estimates are measured from real SIR-C acquisitions over the amazon basin in Brazil. Furthermore, the implementation of an automatic masking algorithm is discussed, which is used to free the used images from disturbances like rivers and lakes.

4.1 In-Orbit Antenna Measurements

In-orbit measurements of the antenna elevation pattern are based on the observed radiometric variation in the range direction of a radar image. The directional antenna gain imposed on the backscatter can be derived, for example, from previously deployed reflector arrays on the ground. Usually tough, more readily available targets, such as distributed uniform scatters like the amazonian rain forest are utilized. Based on [35, 36, 37] a three step approach was devised:

1.) Selection of suitably homogeneous images.

2.) Extraction of the range profile.

3.) Derivation of the in-orbit antenna elevation pattern. this involves conversion to look-angle coordinates, correction of range spreading loss and conversion to gamma nought.

4.1.1 Image Selection

Accurate estimation of the antenna elevation pattern requires several SAR-Acquisitions of distributed targets with well-known backscatter properties. A popular location for such acquisitions is the Amazon basin which has been used for SAR calibration in the past. The rain forest is a large, flat, and uniform target, but most importantly it warrants the assumption that the backscattering coefficient γ^0 is constant across such images. If range spreading loss is accounted for, the remaining amplitude variation in the range direction of the uncorrected SAR image represents the two-way in-flight antenna pattern $G = G_t G_r$ [35]. The selected scenes were generated as standard SLC products in slant range-azimuth coordinates. To avoid distortions in the range profile test sites had to be free from rivers, clear cuts and other large geological features. For this purpose, an

additional screening process, based on a χ^2-similarity test, was applied to guarantee similarity in signal-distribution across the image. Only the best parts in terms of homogeneity are selected for further processing.

4.1.2 Range Profile: χ^2-Similarity Test

Since SAR-images cover vast areas, perfectly uniform images are rare even in the Amazon. For this reason, a subroutine was implemented that identifies and removes nonuniform parts in the images before the range profile is calculated. The screening process is based on [36], where the image is divided into multiple cells, so that they can be examined using the χ^2 -similarity test. Effectively, this test compares the histogram of the cell under consideration with the histogram of the entire corresponding row of cells (see Fig. 4.1.1). The χ^2 -parameter is calculated for each cell using the following equations:

$$\chi^2_{i,j} = \sum_{l=1}^{N} \frac{(C_l^{i,j} - \boldsymbol{C}_l^i)^2}{C_l^{i,j} + \boldsymbol{C}_l^i} \tag{4.1.1}$$

$$\boldsymbol{C}_l^i = \frac{1}{J} \sum_{j=1}^{J} C_l^{i,j} \tag{4.1.2}$$

$C_l^{i,j}$ represents the measured histogram at the l^{th} bin of the cell in the i^{th} row and j^{th} column. Rows and columns are aligned with azimuth- and range-direction respectively. $\boldsymbol{C}_l^i$ is the measured histogram of the entire i^{th} row area. It is obtained by Equation (4.1.2), where J is the number of columns. Cells with low values of χ^2 are considered to be similar to the majority of the i^{th} row. If $\chi^2_{i,j}$ exceeds a threshold, the associated Cell is marked as nonuniform and subsequently removed from the image. The threshold was chosen empirically and set to three standard deviations below or above the mean. Standard deviation and mean are calculated from all the χ^2 values in the corresponding row of cells. Additional screening steps compare mean power between the cell under test and a 5x5 window of surrounding cells. If a deviation of more than 50% is found, the associated pixels are removed as well. The image shown in Fig. 4.1.2 demonstrates that the algorithm successfully filters out nonuniform regions, such as the river.

The remaining parts of the image are collapsed to a single range profile, by averaging in the azimuth direction. For a standard SLC produced by the SIR-C processor, this means averaging as much as 21000 values per range sample .

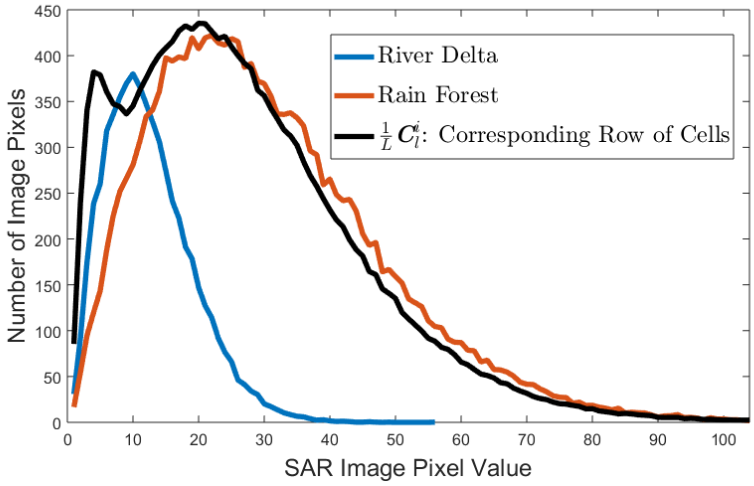

Figure 4.1.1: Exemplary histograms of an image cell containing a river (blue), a section of the Amazon rain forest (red), and the entire corresponding row divided by the number of cells in azimuth (black).

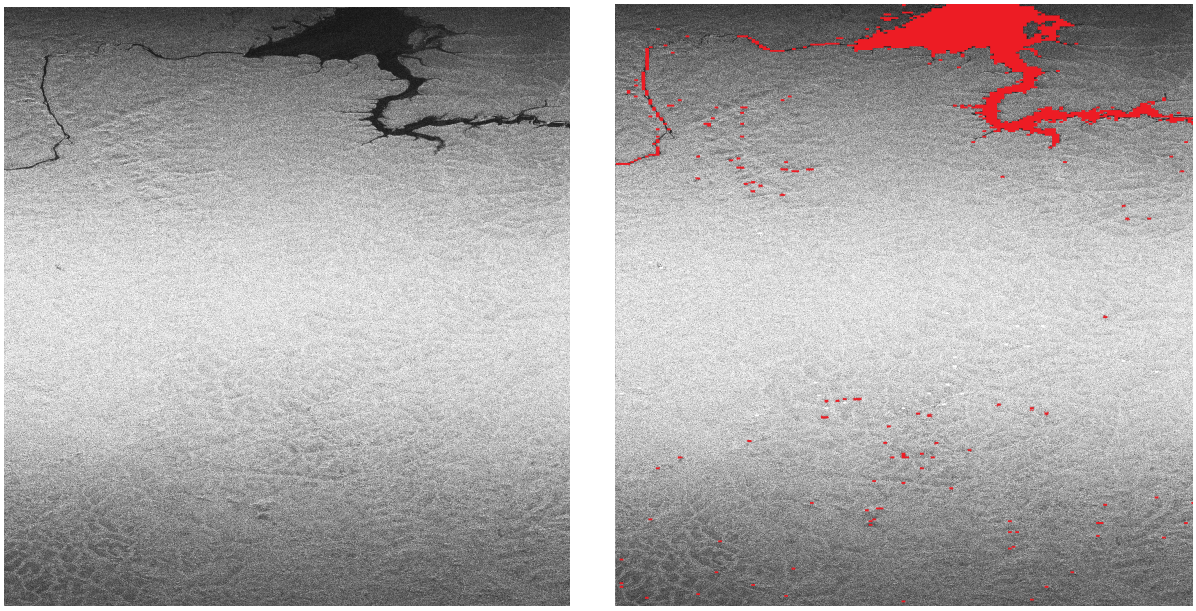

Figure 4.1.2: Similarity screening algorithm: On the left hand side, an exemplary acquisition over the Amazon rain forest is shown. The image on the right hand side depicts the same scene after the similarity screening. The cells associated with χ^2-values above the threshold (colored in red) will subsequently be assigned "not a number" (NaN).

4.1.3 Derivation of the Antenna Elevation Pattern

As per the SAR radar equation discussed in Section 2.6, the backscatter coefficient β^0 is related to the antenna elevation pattern by Equation (4.1.3):

$$\beta^0 = \mathrm{DN}_i^2 \cdot K \cdot \frac{(R_0 + i \cdot dR)^3}{R_0^3} \cdot \frac{1}{G_\mathrm{t}(\theta_i) G_\mathrm{r}(\theta_i)}, \tag{4.1.3}$$

where R_0 is the slant range to the first pixel, i is the range pixel index, dR is the slant range pixel spacing and K is a constant calibration factor. Substitution with Equation (2.5.4) results in:

$$\gamma^0 = \mathrm{DN}_i^2 \cdot K \cdot \frac{(R_0 + i \cdot dR)^3}{R_0^3} \cdot \frac{1}{G_\mathrm{t}(\theta_i) G_\mathrm{r}(\theta_i)} \cdot \tan(\alpha_i). \tag{4.1.4}$$

The assumption that gamma is constant across the selected scenes further reshapes Equation (4.1.4) to:

$$G(\theta_i) = G_\mathrm{t}(\theta_i) G_\mathrm{r}(\theta_i) = \mathrm{DN}_i^2 \cdot \frac{(R_0 + i \cdot dR)^3}{R_0^3} \tilde{K} \cdot \tan(\alpha_i). \tag{4.1.5}$$

The principle behind Equation (4.1.5) is illustrated in Figure 4.1.3. The antenna look angles θ_i corresponding to pixel i, as well as the local incidence angles α_i are calculated using the cosine theorem:

$$\theta_i = \arccos\left(\frac{R_\mathrm{s}^2 + R_i^2 - R_{\mathrm{e},i}^2}{2 \cdot R_\mathrm{s} \cdot R_i}\right), \tag{4.1.6}$$

$$\alpha_i = 180 - \arccos\left(\frac{R_{\mathrm{e},i}^2 + R_i^2 - R_\mathrm{s}^2}{2 \cdot R_i \cdot R_{\mathrm{e},i}}\right), \tag{4.1.7}$$

$$R_i = R_0 + i \cdot dR = R_0 + i \cdot \frac{c}{2 \cdot f_\mathrm{s}}, \tag{4.1.8}$$

where R_s is the magnitude of the spacecraft position relative to the earth center, R_i is the slant range per pixel, c is the speed of light, f_s is the range sampling frequency and $R_{\mathrm{e},i}$ are the Earth radii per pixel calculated according to the ellipsoid model (Eq. (2.5.5)).

In order to compare antenna pattern estimates obtained with Equation (4.1.5), the individual gamma profiles are converted into a common coordinate system. One way to do this is by subtraction of the off-nadir boresight look angle. As a result, antenna patterns derived from different images are all centered around zero degrees. The calculation is done as follows:

1. The necessary parameters including electronic steering angle in elevation θ_S, pitch θ_P, yaw θ_Y and roll θ_R -angles are read from a meta-file.

2. The antenna look angle prior to shuttle rotation is $\theta_\mathrm{L} = \theta_\mathrm{T} + \theta_\mathrm{S}$, where $\theta_\mathrm{T} = 14^\circ$ is the nominal mechanical tilt angle (see Fig. 4.1.4).

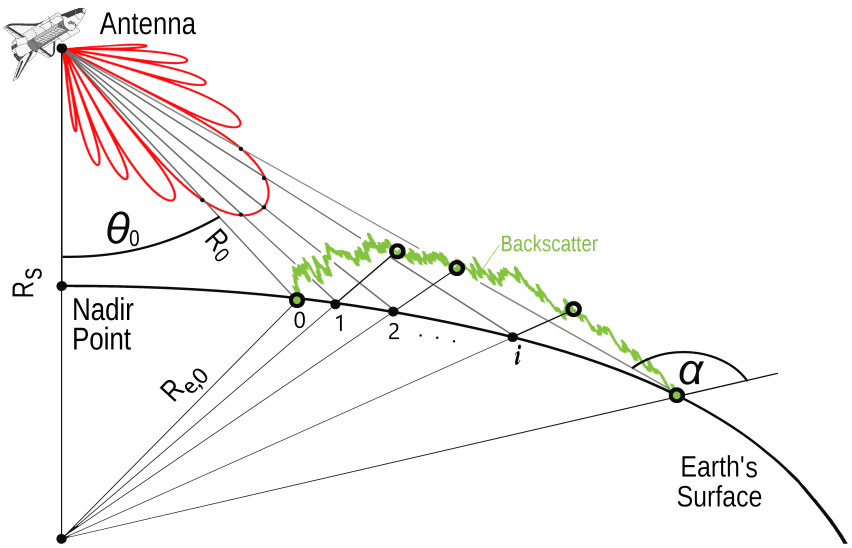

Figure 4.1.3: The figure illustrates how the side looking acquisition geometry of SAR and the curvature of the earth alter the shape of the antenna pattern. In order to compare the reference patterns generated by the antenna model with the range profile, a conversion to a common coordinate system is necessary. First, the antenna reference pattern needs to be resampled, so that the off-nadir look angles θ_i correspond directly to the slant ranges R_i. Second, the reference area $A_\beta = \delta_\mathrm{a}\delta_\mathrm{R}$ for the backscatter coefficient β^0 is converted to an equivalent area perpendicular to the radar beam (conversion to γ^0). Finally, the differences in slant range across the swath are compensated. According to the SAR radar equation (see Eq. (2.6.9)), the intensity of a processed SAR image is inversely proportional to third power of the slant range.

3. The off-nadir look angle θ_b (Antenna boresight) following the pitch, yaw, roll sequence is calculated according to Equation ((4.1.9))

$$p = \begin{pmatrix} p_\mathrm{x} \\ p_\mathrm{y} \\ p_\mathrm{z} \end{pmatrix} = \begin{pmatrix} \cos(\theta_\mathrm{P}) & 0 & \sin(\theta_\mathrm{P}) \\ 0 & 1 & 0 \\ -\sin(\theta_\mathrm{P}) & 0 & \cos(\theta_\mathrm{P}) \end{pmatrix} \cdot \begin{pmatrix} \cos(\theta_\mathrm{Y}) & -\sin(\theta_\mathrm{Y}) & 0 \\ \sin(\theta_\mathrm{Y}) & \cos(\theta_\mathrm{Y}) & 0 \\ 0 & 0 & 1 \end{pmatrix} \cdot \begin{pmatrix} 1 & 0 & 0 \\ 0 & \cos(\theta_\mathrm{R}) & -\sin(\theta_\mathrm{R}) \\ 0 & \sin(\theta_\mathrm{R}) & \cos(\theta_\mathrm{R}) \end{pmatrix} \cdot \begin{pmatrix} 0 \\ \sin(\theta_\mathrm{L}) \\ -\cos(\theta_\mathrm{L}) \end{pmatrix}$$

$$\theta_\mathrm{b} = \cos^{-1}(p_\mathrm{z}). \tag{4.1.9}$$

It should be noted, that the provided state vector readings, and especially the antenna boresight vector are subject to considerable uncertainty which introduces significant errors to the calculation of θ_i. This problem will be further discussed in a later section of this thesis. In this case, a workaround was used in which the antenna boresight is determined by the angle associated with maximum signal power. The corresponding sample is obtained by finding the maximum in a polynomial fitted to the noisy range profile data. Next, a cloud of individual estimates is

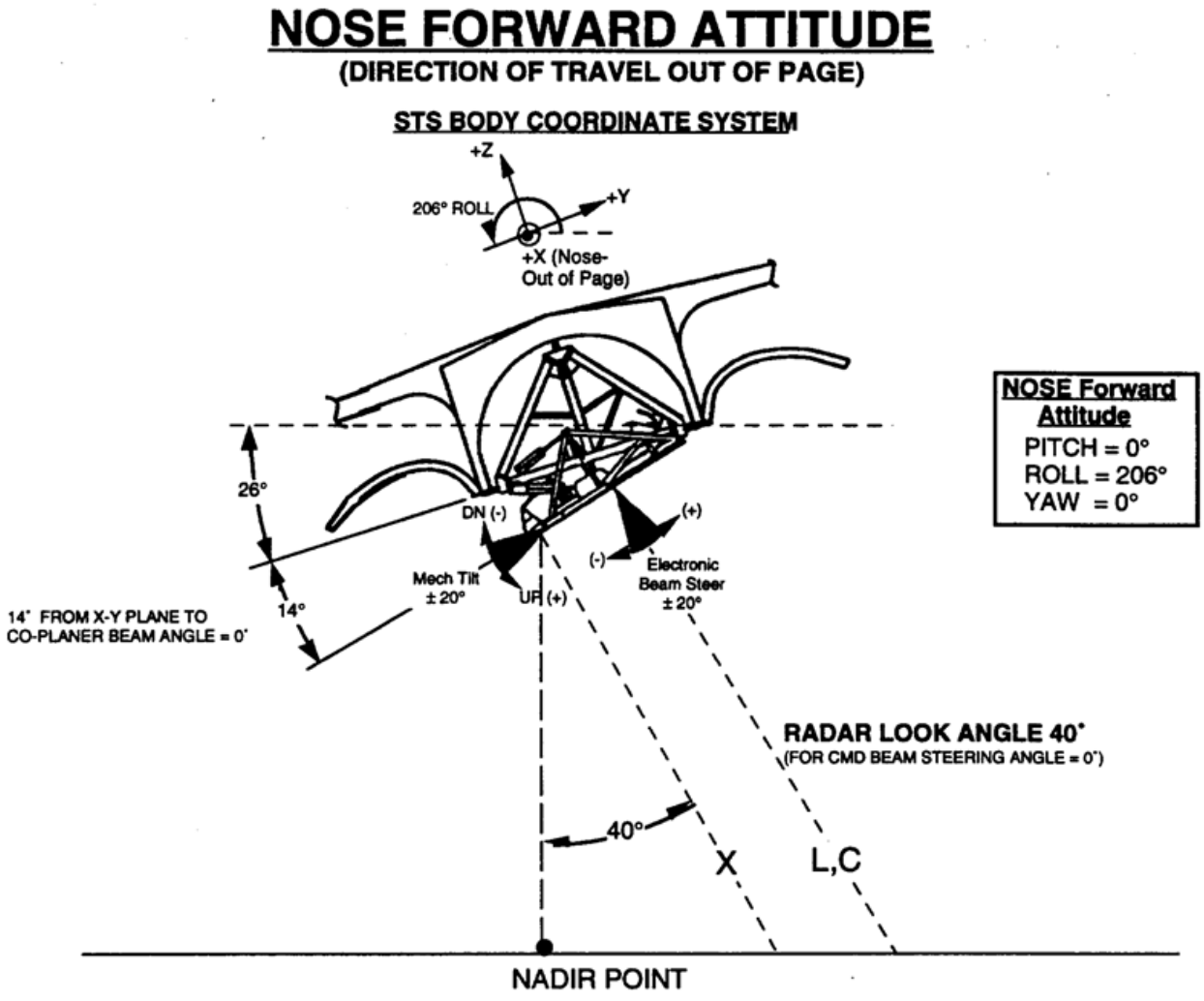

Figure 4.1.4: Nominal attitude of the Space Shuttle (Image Credit: Jet Propulsion Laboratory [20]).

combined to one average range profile and converted to decibels. in addition, a piecewise quadratic regression filter is applied for a noise free representation of the antenna pattern. Finally, the pattern is referenced to zero at boresight. This has the effect of a constant scaling factor applied uniformly across range, and does not affect the shape in elevation [35]. The simulated relative antenna pattern can now be compared to the obtained measurement. The deviation between the two patterns can be considered as the remaining relative calibration uncertainty with respect to the antenna pattern. Examples and an evaluation of the antenna model accuracy are given in Section 6.1.

5 Antenna Pattern Correction Algorithm

In this chapter, the implementation of the antenna pattern correction is discussed. A summary of the steps involved in antenna pattern generation is given and the subsequent application to real SIR-C data is laid out. Section 5.2 introduces the offset problem as a result of ephemeris uncertainty and presents possible solutions. An approach as to how the required parameters can be estimated form the image data itself is discussed. Since this approach is only applicable under certain conditions, two possible modifications are proposed in order to deal with these limitations. As a last point, the final implementation of the SIR-C antenna pattern algorithm is presented.

5.1 Antenna Pattern Generation

The antenna patterns are calculated according to Section 3.3 by combining the probe data and the pre-measured stick patterns. That is, the array factor is calculated from the probe data and the stick locations. Then, the array factor is multiplied by the stick pattern to yield the antenna pattern. A few exemplary cases are shown in Figure 3.4.2.The APGA returns a two dimensional cross section of the full directional characteristic. In the default case the pattern is obtained by cutting through the elevation plane, but other cross sections can be specified by the user. Antenna patterns are obtained either with ideal phase shift and stick current values or by using experimentally obtained test data from probe measurements. These data provide the feed current distribution across the aperture and the measured phase shifts for each phase-shifter control bit in the antenna array. If the test data pattern is chosen by the APGS-user, the relevant Matlab subroutines read stick currents and phase information from formatted text files (see Appendix B), rather than assuming an ideal distribution and exact phase shift increments. The transmit and receive patterns are combined to the final correction pattern by adding the decibel values together. The device failure files contain the On/Off status for L- or C-band, polarization and receive/transmit-mode. The resulting change in the antenna pattern will be taken into account by the APGS if the files are updated accordingly. At this stage the generated pattern is available as a vector pair (antenna elevation angles and directional gain), where the samples in the pattern vector correspond to equal spaced angular increments in the elevation. Since the spacing between slant range samples is nonlinear, the pattern vector is interpolated and resampled to match the elevation look angles per pixel θ_i. After that, sine and cosine correction is applied and the antenna pattern is adjusted to compensate range spreading loss (conversion to gamma nought according to section 4.1.3). Once all the above computations are completed, the resulting antenna pattern in decibels is normalized and subtracted from the

SLC-magnitude image in range. The $0\,\mathrm{dB}$ maximum of the normalized pattern is the sample that presumably corresponds to antenna boresight (maximum transmit/receive-power). The conversion to gamma nought offers the benefit, that the residual variation (peak to peak excursion) in the corrected range profile can be considered as the remaining relative calibration uncertainty. This assumption is valid to the extend that the backscatter coefficient γ^0 of a particular scene can be considered constant across range. The amazonian rain forest is known to offer the best conditions in this respect and has been used for in-flight antenna pattern verification before. To improve the agreement with the actual in-flight antenna pattern, the range profile is obtained by the method described in Section 4.1.2. Subsequently, the peak to peak excursion of the corrected range profile can be checked against the stated goal of $\pm 1\,\mathrm{dB}$ range variation for SIR-C rain forest data [4].

5.2 Offset Problem

5.2.1 Angular Offset in Elevation

For antenna pattern correction, a critical computation concerns the interval of elevation angles that directly corresponds to the first and last sample in range. Accurate knowledge of the viewing geometry is required as even slight deviations in the look angle interval can introduce significant cross track errors. Unfortunately, the solution based on available orbital state vector- and shuttle attitude information lacks the accuracy needed for antenna gain pattern correction. As will be discussed below, the main source of uncertainty is the magnitude of the spacecraft position relative to the Earth center and the antenna pointing vector. Both of those parameters are used to calculate the look angles and determine the interval the antenna pattern is generated for. Errors in the elevation angles lead to mismatch between pattern and range profile as shown in Figure 5.2.1. Estimates of the angular offset between antenna model and gamma profile are as high as $\pm 2.1^\circ$ in some cases.

5.2.2 Error Sources

The reason for the discrepancy lies in the uncertainty of the available ephemeris data. As previously stated, there are three different sources for obtaining ephemeris data for SIR-C: The Mission Operations Subsystem, state vectors embedded in the file headers, and Post-flight Attitude and Trajectory History (PATH) tapes from the Johnson Space Center [3]. PATH tape data are most reliable in terms of completeness and accuracy but are not released for civilian use. Instead, the availability of ephemeris information is restricted to the file headers which are quoted as being the least accurate [11]. This is why alternative solutions are required, which involve estimation of the necessary parameters from raw data and the processed SIR-C images itself. First, however, the

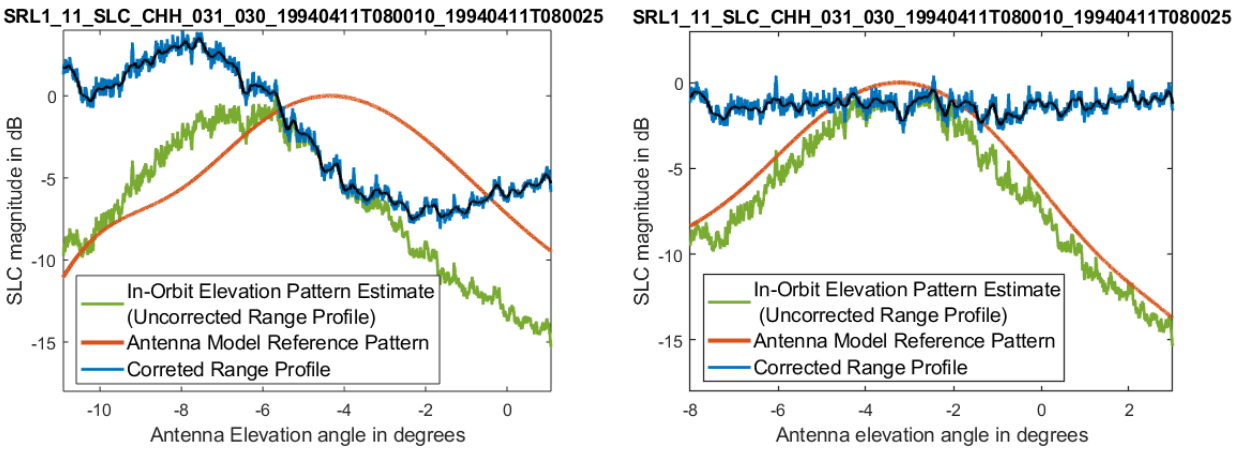

(a) Offset problem caused by inaccurate knowledge of the viewing geometry.

(b) Offset compensation (best fit in the least squares sense).

Figure 5.2.1: The plot on the left hand side shows an exemplary case of antenna pattern correction, where unaltered header information is used to determine the antenna pointing angle. The in-orbit elevation pattern estimate, depicted as the green ripple, was derived from a real SIR-C acquisition, identifiable by the granule ID in the plot title. A large angular offset between the reference pattern and the range profile is clearly visible, as well as the large cross-swath errors after the antenna pattern is subtracted (depicted as the blue ripple). Compensating this offset by fitting the reference pattern to the range profile, can significantly reduce cross-track errors, as is shown on the right hand side of the figure.

possible error sources must be understood. Considering the geometry in Figure 4.1.3 the observed angular offsets have two possible causes: Errors in the *off-nadir look angles* θ_i or errors in the antenna pointing angle θ_b (*antenna mispointing*).

Antenna mispointing, could either result from uncertainty in the shuttle attitude or from steering errors caused by the active phased array. To investigate the latter case, the offsets in several datatakes with identically commanded steering angles were compared. Systematic errors, caused for example by faulty antenna elements like phase shifters or amplifiers were not confirmed. The available test data however, was limited to 12 datatakes with an average aquisition time of 1.5 minutes. Another argument against electronic steering being the primary reason for the offset problem is, that no such errors were found in the JPL calibration documents. Even tough TR-module- and C-band panel malfunctions occured in both SRL1 & 2, the failures reportedly had little impact on calibration [3].
In contrast to steering errors, the uncertainty of the shuttle attitude is well documented (see Table 2.3.1) and has been cited by [21], as one of the main challenges in SIR-C processing. However, the uncertainty of $\pm 1.24°$ in the roll angle can not explain the entire observed angular offsets by itself.

The off-nadir look angles per range sample θ_i are calculated according to the cosine theorem (see

Fig. 4.1.3):

$$\theta_i = \arccos\left(\frac{R_{\mathrm{s}}^2 + R_i^2 - R_{\mathrm{e},i}^2}{2 \cdot R_{\mathrm{s}} \cdot R_i}\right), \tag{5.2.1}$$

$$R_i = R_0 + i \cdot dR = R_0 + i \cdot \frac{c}{2 \cdot f_{\mathrm{s}}}. \tag{5.2.2}$$

Here, R_{s} is the magnitude of the spacecraft position relative to the Earth center, R_i is the slant range per pixel, c is the speed of light, f_{s} is the range sampling frequency and $R_{\mathrm{e},i}$ are the Earth radii per pixel calculated according to the ellipsoid model (see Eq. 2.5.5). As a potential source of the calculation errors, one of the three triangle sides $R_{\mathrm{s}}, R_i, R_{\mathrm{e},i}$ can be immediately eliminated: The slant range magnitude to first pixel is

$$R_0 = \left(\frac{n_{\mathrm{p}}}{PRF} + DWP - \tau_{\mathrm{d}}\right) \cdot \frac{c}{2}, \tag{5.2.3}$$

where n_{p} is the number of pulses in the air, DWP (Data Window Position) is the delay between the rising edge of the PRF-pulse and the data taking trigger and τ_{d} is the electronic delay time. With exception of τ_{d} all these parameters are precisely known and even the remaining uncertainties in the electronic delay time are so small that they have virtually no effect on θ_i. After all, slant range distance is what a radar measures. The assumption that R_i are sufficiently accurate is further supported by the fact that the processed SIR-C SAR images have the expected focus and contrast, which is evidenced in [15] by the figures of merit derived from impulse response functions. Significant errors in the slant range would lead to obvious degradation of the image quality since it is a key parameter in multiple processing steps. This leaves the platform position magnitude R_{s} and the Earth radius per slant range sample $R_{\mathrm{e},i}$. Obviously, the approximation of the Earth by an ellipsoid contributes a certain amount of error, but given that the original SIR-C calibration achieved good results with Clarke 1866, it can be assumed that this is not the main reason for the observed offset problem. In addition, testing of rain forest scenes with manually adjusted $R_{\mathrm{e},i}$ showed no drastic improvements. For the adjustments, GPS-data from Google Earth was used to add an ellipsoidal reference height corresponding to the most frequent site elevation. It should be noted, that scene altitude can be determined precisely by Digital Elevation Models (DEM). Incorporation of DEMs into the APCA could eliminate altitude errors entirely or at least quantify the uncertainty. This however, exceeds the scope of this bachelor thesis and may be a topic for future work.

The process of elimination suggests that the primary cause of error in the look angle calculation are inaccuracies in the platform position magnitude R_{s}. This is supported by reports of large errors in Geo-coding, in which the location is derived from the position and velocity vectors. The worst case position error is estimated to be on the order of several kilometers [11, 38]. Furthermore, the state vector from the file headers is known to suffer from substantial uncertainty and has been reported by [39] to potentially cause errors in the look angle calculation. Hence, the original SIR-C processor used the more reliable Post-flight Attitude and Trajectory History (PATH) tapes containing refined shuttle orbit information.

While the mismatch observed in Figure 5.2.1 is a combination of all factors discussed above, it can be concluded that the space craft position and the shuttle attitude are the two largest contributors to the overall error. Thus, the following sections will focus on optimizing these particular parameters.

5.3 Reducing the Angular Offset in Elevation

In most cases the range profile roughly resembles the shape of the antenna pattern, even if the scene under consideration does not meet the requirements discussed in 4.1.2. When the range profile is calculated by averaging the azimuth lines, much of the naturally occurring backscatter-variation is filtered in the process. Hence, the observed angular interval can be estimated by finding the sector in the generated antenna pattern that best correlates with the signal variation in the range profile. The location of the beam center, and by extension the minimal and maximal observation look angles, can usually be narrowed down to a few samples, even if there are substantial discrepancies between antenna pattern and range profile. To this end, multiple iterations of the antenna pattern are generated by successively changing the platform position magnitude R_s. The look angle θ_b is kept constant across all iterations, since R_s does not factor into its calculation (see Eq. 4.1.9). This has the effect of sliding a window across the antenna pattern. In each iteration, the limits $\theta_\mathrm{A,min}$ and $\theta_\mathrm{A,max}$ shift by a small increment until all samples of the antenna pattern eventually end up at the correct range bins (see Fig. 5.3.1). The procedure is as follows:

- The slant range to the first pixel R_s is incremented or decremented. The current version of APGA uses 250 pattern iterations where R_s is varied over a span of $\pm 5\,\mathrm{km}$. .
- The look angles-, local incidence angles- and slant ranges per pixel are calculated for each R_s according to Equations 4.1.6, 4.1.8 and 4.1.8.
- The angular limits in antenna coordinates $\theta_\mathrm{A,min}$ and $\theta_\mathrm{A,max}$ are calculated according to Equations 5.3.1 and 5.3.2:

$$\theta_\mathrm{A,min} = \theta_I - \theta_\mathrm{b} + \theta_\mathrm{S} \tag{5.3.1}$$

$$\theta_\mathrm{A,max} = \theta_{\max\{i\}} - \theta_\mathrm{b} + \theta_\mathrm{S}, \tag{5.3.2}$$

  where θ_S is the commanded electronic steering angle. The corresponding section of the antenna pattern is resampled, sine and cosine corrected and adjusted for range spreading loss (see Section 5.1).

- The iteration associated with the lowest sum of squared residuals (SSR) after subtraction from the normalized range profile is selected as the best fit.

The angular mismatch between antenna pattern and range profile can be drastically reduced by finding the best fitting pattern in the least squares sense (see Fig. 5.2.1).

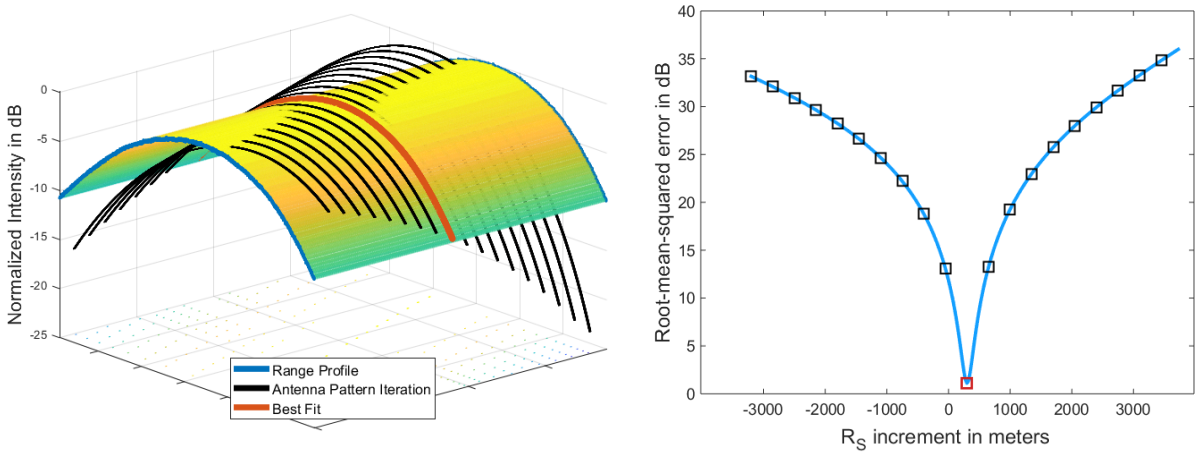

(a) Antenna model reference pattern iterations.

(b) Fit error between the antenna model reference pattern iterations and the range profile.

Figure 5.3.1: The figure shows the principle by which the correct off-nadir look angles are estimated. Subfigure (a) depicts multiple iterations of the antenna pattern as a result of successive incremental changes in either the shuttle position magnitude R_s or the shuttle roll angle. The iteration that best matches the range profile, is identified by the lowest root-mean-squared error, or rather, the sum of squared residuals after the reference patterns are subtracted from the normalized range profile. Subfigure (b) depicts the root-mean-squared fit error for 250 iteratations of the Shuttle position magnitude R_s. The iterations corresponding to the patterns in (a) are represented by the black and red markers.

5.4 Reducing the Angular Offset in Elevation: Execptions & Limitations

Naturally, there are limits as to how accurate the angular offset can be estimated from the range profile. The uncertainties involved in the pattern generation itself are discussed in Section 6.3. Under the prerequisite, that the APGA reproduced the actual antenna elevation beam with sufficient accuracy, we can assume that one of the previously discussed iterations contains the sector of the beam, that was actually used to sample the radar response. Hence, the main issue is, if the (most) correct pattern is also identified as such. As mentioned earlier, the success of the approach mainly depends on how well the in flight antenna pattern is retained in the range profile. While most of the variation in the average radar backscatter coefficient is filtered by averaging, some geological features can cause additional variation in the range profile on the order of several decibels. These conditions are usually observed in coastal scenes or other dominating bodies of water, like lakes or river deltas. The weak backscatter from water surfaces skews the average range profile to a point, where results are inaccurate at best and exacerbate the problem at worst. Figure 5.4.1 (a) depicts such a case, where the best fit in the least squares sense causes dramatic overcorrection of otherwise dark areas in the image. Left unchanged, some residual errors remain, but an overall better result

is achieved (Fig. 5.4.1 (b)). The same principle applies to acquisitions over the ocean. Fitting

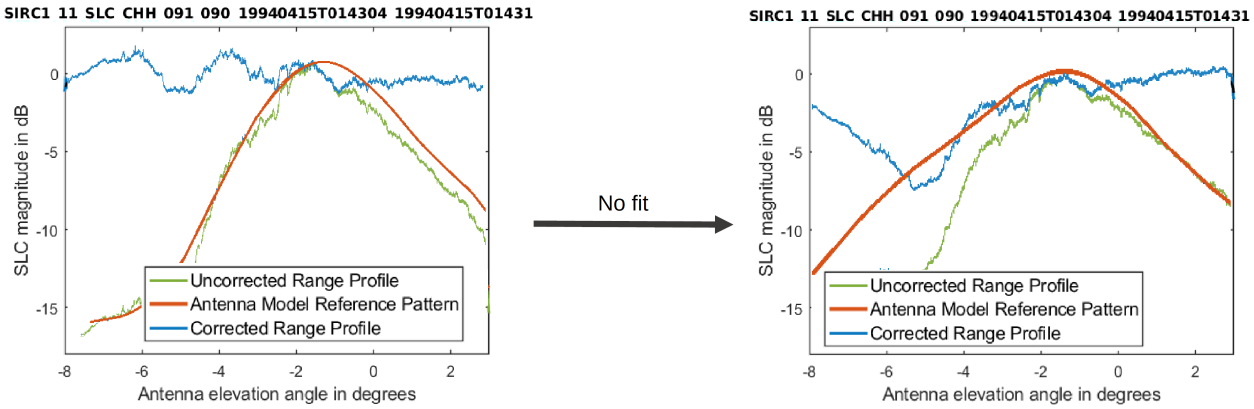

(a) Coastal Scene: The left plot represents the fitted antenna pattern correction, while the one on the right shows the unmanipulated result.

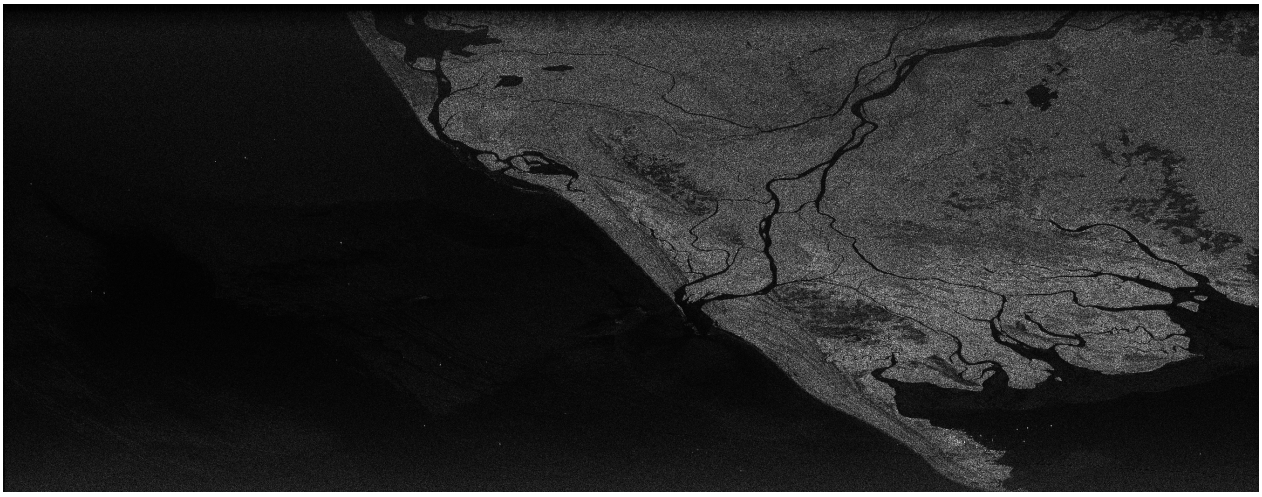

(b) SIR-C SAR-image considered in Subfigure (a).

Figure 5.4.1: Exemplary case of a coastal scene. The plots in Subfigure (a) demonstrate that the approach detailed in Section 5.3 is not suitable for images like the example depicted in Subfigure (b).

the antenna pattern to the range profile is ineffectual, since radar backscatter from water surfaces decreases drastically at high incidence angles.

Fortunately, problem cases, such as the examples discussed in this section, can easily be identified via thresholding of the sum of squared differences (SSD) between antenna model reference pattern and range profile. To ensure comparability in the SSD values across different datatakes/scenes, the pattern maximum is always referenced to $0\,\mathrm{dB}$ and the final result is normalized to sample size. The current version of the APGA uses a threshold of $4.9\,\mathrm{dB}$ to determine if the range profile bears appropriate resemblance to the antenna pattern.

5.5 Angular Offset in Elevation: Handling of Exceptions

Two strategies were pursued to deal with cases were the SSD exceeds a set threshold:

5.5.1 Null Line Approach

Given how important the look angle is for SAR processing and calibration, a special Null Line Processor was employed in the original SIR-C preprocessing stage to estimate the antenna boresight position. It was originally tasked to derive roll angle estimates by processing especially transmitted and received signal data (Null Lines) embedded with the regular SAR signal (see Fig. 5.5.1 (a)) [40]. Since the normal antenna beam is fairly broad, putting a null at the boresight helped to figure out at what range sample the boresight is situated and by extension, where it is pointing. When beam nulling was enabled, the receive phase of half of the antenna array in elevation was inverted by $180°$. The received beam therefore has a notch or "null" at the boresight [40]. This was done at a rate of one Null Lines per second of SAR data. The processing routine was eventually bypassed when it was determined that the shuttle attitude information was accurate enough to compute the roll angle values directly. This applies only to the PATH-data and not to the header information available for this thesis. Nevertheless, the Null Lines are still present in the raw data and were used in this thesis to reduce the offset-problem encountered during antenna pattern correction. The principle of this approach is to chose the angular limits of the elevation pattern in such a way, that the maximum is in the same location relative to sample size as the notch in the null line data. This is done in one of two ways:

1. First, a sector of the antenna beam pattern is generated, that extends well beyond the actually used beamwidth. Based on the unaltered state vector information the pattern is then resampled, sine and cosine corrected, and adjusted for range spreading loss. Finally, a section of same sample size as the null line is extracted in the manner as shown in Figure 5.5.1 (c).

2. The pattern can be taken from the stack of previously generated iterations (see Sec. 5.3). This time, instead of fit quality, the iteration is selected based on the minimum distance between pattern maximum- and Null Line minimum location (in samples).

Since both patterns were most likely resampled with different off-nadir look angles, there may be slight deviations in their overall shape. Here, the difference in look angles arises from potentially different values of R_{s} used in Equation (4.1.6). This approach therefore addresses the possibility, that the observed offset in the scene under consideration is caused predominantly by antenna mispointing. If the roll angle is the primary error source, pattern 1 is expected to have better accuracy. In contrast, pattern 2 is optimized to correct errors in the shuttle position parameter R_{s}. The decision, which one to use is made on the basis of least sum of squared differences to the range

profile. An Example of a Null Line after range compression is given in Figure 5.5.1 (b). The signal is very noisy which is mainly because it is not fully processed yet. Since Null Lines are isolated pulses, azimuth compression can not be used to focus the signal. Instead, multiple filter steps are applied, in order to improve the null estimation in the noise pattern:

1. The signal pulse adjacent to the null line is subtracted (in decibels). This results in a better defined notch since the next pulse will peak in the same place as the null line dips.

2. Step one is repeated for all available null lines in the present raw image data. Usually, there are around 15 null lines per raw-file, which are combined to a single average.

3. The resulting null-pattern, shown in Figure 5.5.1 (c), is passed through a median filter to reduce spikes in the noise, and subsequently smoothed by a moving boxcar quadratic regression (boxcar-size = 1000 samples).

The null beam pattern can be generated by passing the optional parameter `indnull` to the APGS in Matlab.

5.5.2 Mean Angular Offset

Next to the null beam pulse approach, a second method to deal with exceptions was tested. Usage of the null beam pulse requires to load the raw data files and perform range compression, which is both time consuming and computationally expensive. This is avoided with this approach, as the angular offset, in problematic cases, is estimated based on successful offset adjustments, that directly precede and/or follow the scene in question. Instead of correcting each scene individually, all pulses (azimuth lines) in a given data-take are processed as one long strip. Range profiles are calculated for every 10000 pulses each of which are fitted with antenna patterns in the manner described in Section 5.3. The angular offsets with respect to a reference pattern with unaltered parameters are recorded in order to identify and correct potential outliers. The procedure is as follows:

1. A median filter is applied to the recorded offset data. Offset data, to reiterate, refers to the angular shifts in elevation as a result of least squares fitting of the antenna model output vector to the range profile.

2. The weighted average of all offsets is calculated. The weights are the inverse of the fit error (Sum of squared differences). This ensures, that scenes, where the range profile shows good agreement with the antenna pattern, are weighted more heavily while problem cases are prevented from distorting the results.

3. Every case that deviates more than 1.5 standard deviations from the weighted average is considered an outlier. In all other cases the relevant image section is corrected with the

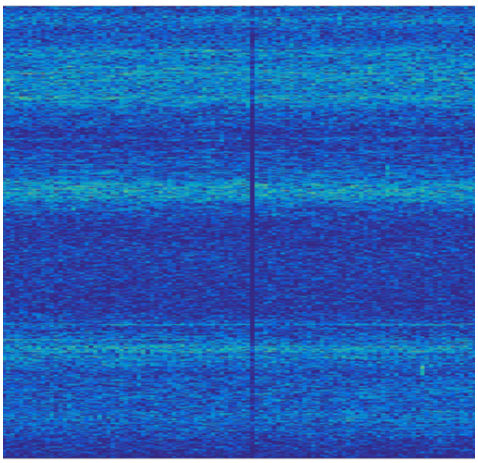

(a) Null Line embedded in the raw data.

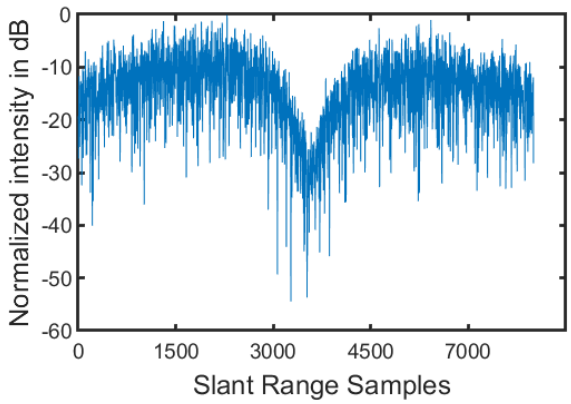

(b) Single Null Line pulse after range compression.

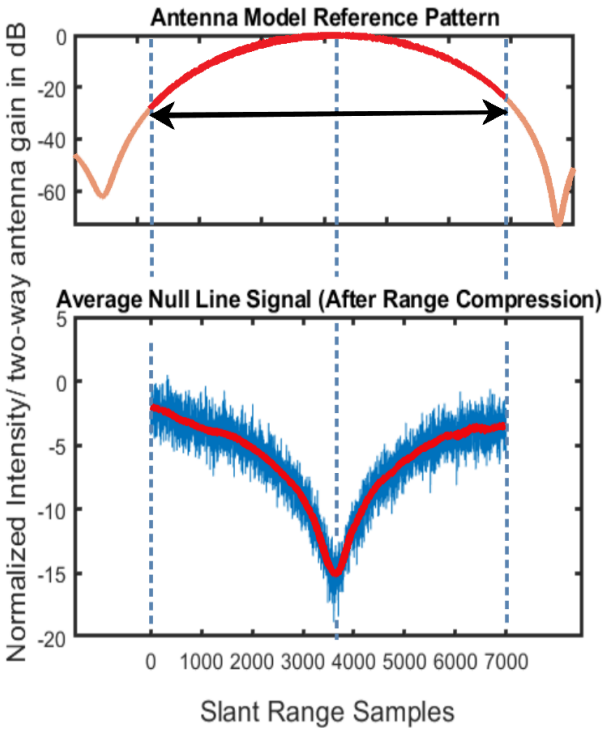

(c) Null Lines after filtering process.

Figure 5.5.1: Null Line Approach: The angular limits of the antenna model reference pattern in elevation are chosen in such a way, that the maximum is in the same location relative to sample size as the notch in the null line data. This principle is depicted in Subfigure (c).

corresponding antenna pattern.

In all identified outlier cases, the correction is done again. This time, the version of the pattern is used, that is closest to the (weighted) mean offset. Figure 5.5.2 depicts the offsets of C-band test data in HH-polarization, along with the weighted mean and the ± 1.5 standard deviation thresholds. The scene that corresponds to the dip below the lower boundary is depicted in Figure 5.5.3 (b). Figure 5.5.3 (a) demonstrates how the discussed modifications can improve the accuracy of the antenna pattern correction in images with large bodies of water. This becomes evident when considering the section of the range profile that corresponds to the vegetated areas in the image.

Additionally, the masking of water bodies can improve the fit quality by reducing the variation in the signal brightness β^0. The resulting range profile is a better approximation of the

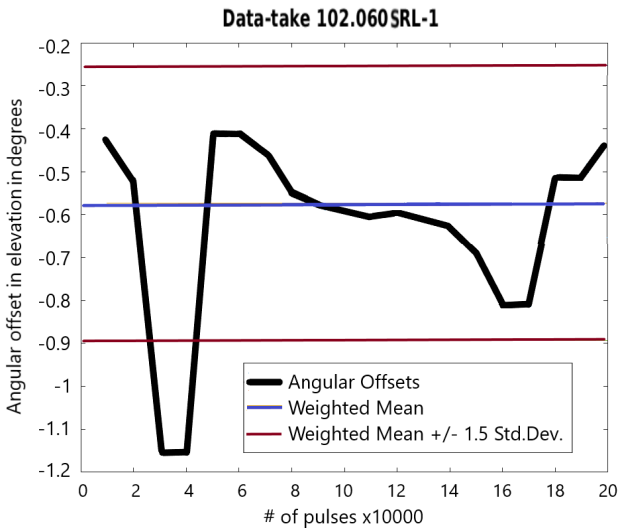

Figure 5.5.2: Offsets, weigthed mean, and thresholds for data-take 102.060-SRL-1.

in-flight antenna pattern and will therefore provide a more accurately weighted offset for further analysis (Fig. 5.5.4). Naturally, this modification has its limits too. As fewer lines are available to be collapsed into average range profile values, the ability to filter natural variation by averaging is reduced. It is not recommended to mask water if it takes up too much of a scene, e.g. a coastal scene aligned in flight direction. If a masking algorithm is employed, these trade-off needs to be considered.

5.5.3 Comparison: Null Line Approach vs. Mean Angular Offset

In the previous section two strategies were proposed as to how the antenna pattern correction can best be applied to images that are not suitable for the approach detailed in Section 5.3. This includes images with high intensity modulation due to the slope of the terrain or high spatial heterogeneity. Images that contain extended areas with exceptionally low backscattering (rivers, savannas) and/or high backscattering (double bounce from the trees over flooded terrain) are also in this category. These targets are not sufficiently homogeneous to allow for meaningful comparison with a reference pattern, which makes it difficult to evaluate performance. In fact, the lack of agreement between gamma profile and antenna pattern is what makes this separate treatment necessary in the first place. Eventually, the *"Null Line Approach"* (NLA) was chosen for implementation in the Antenna pattern Correction Algorithm. The following criteria were considered in the decision:

- In contrast to the *"Mean Angular Offset Approach"*(MAOA), the NLA is not dependent on the availability of full data-takes. Single SIR-C images can be corrected.
- The Accuracy of the correction is consistent and does not depend on the size of the data-take.
- Even though the correction of a full datatake is less expensive computationally MAOA, NLA

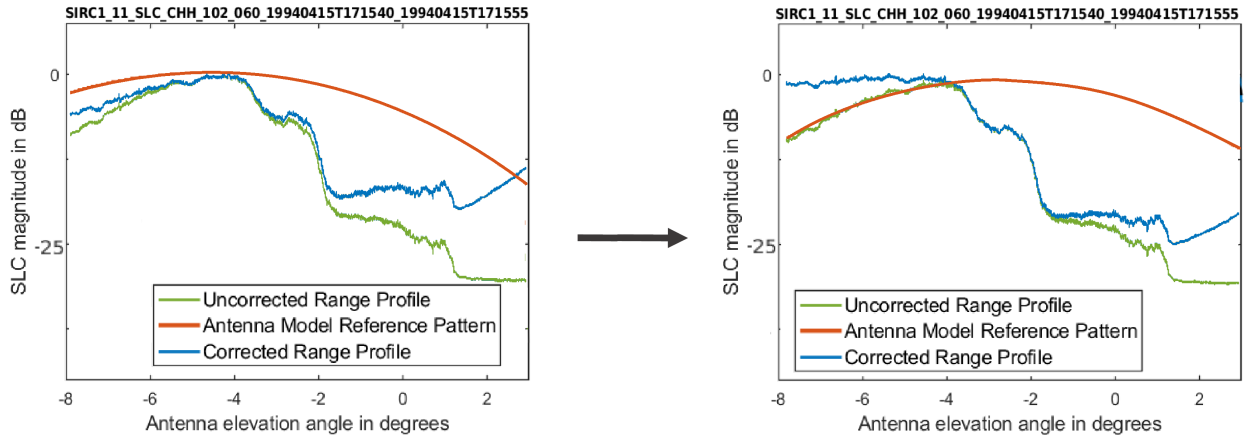

(a) The plot on the left hand side represents the least squares fit detailed in Section 5.3. The plot on the right hand side depicts the result when the Mean Angular Offset Approach is applied.

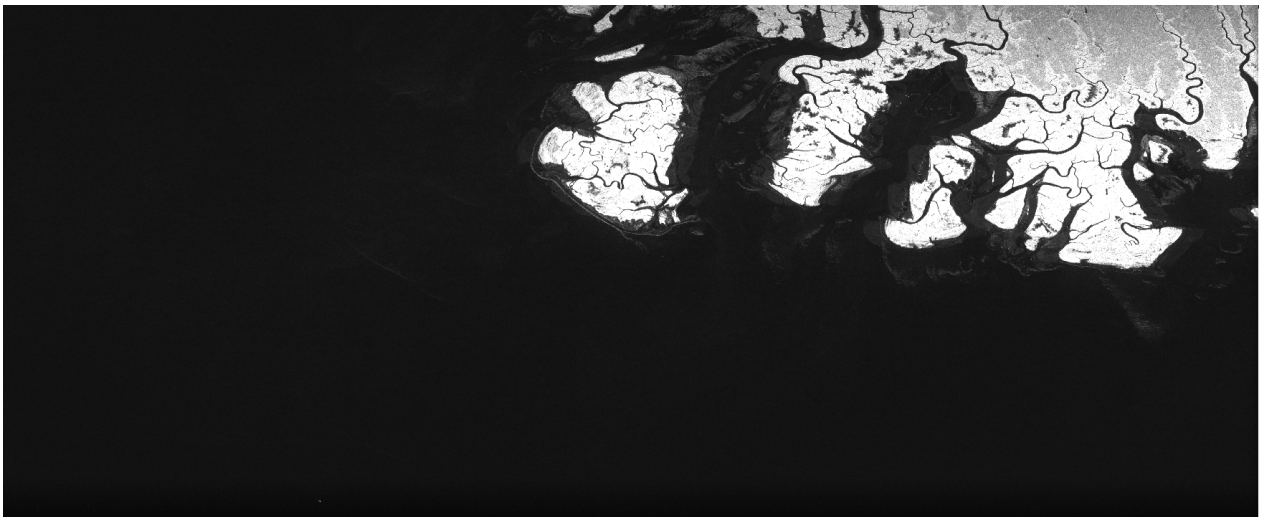

(b) SIR-C SAR-image considered in Subfigure (a).

Figure 5.5.3: The figure depicts the Mean Angular Offset Approach for the scene that corresponds to the outlier identified in Figure 5.5.2. Subfigure (a) demonstrates how this approach can improve the accuracy of the antenna pattern correction in images with large bodies of water. The improvement relative to the best fit in the least squares sense becomes evident when considering the section of the range profile that corresponds to the vegetated areas in the image.

has the advantage that single images can be processed in parallel.

- MAOA may be unreliable for data -takes recorded over the ocean or islands like Galapagos or the Philippines. Conceivably, there may not be a single range line in the whole datatake that does not contain part of the ocean.

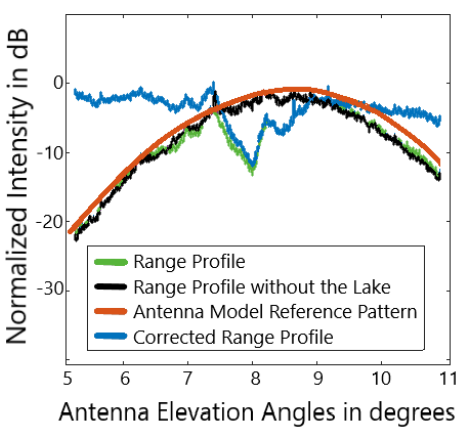

(a) Range profile with- and without masking of Lake Constance.

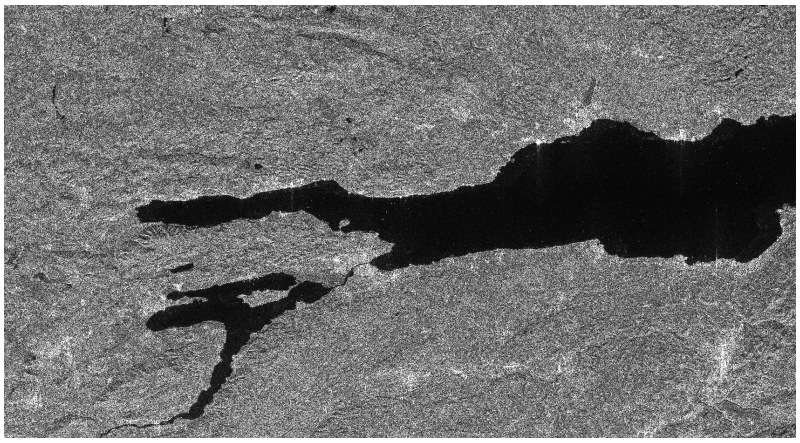

(b) Scene considered in Subfigure (a).

Figure 5.5.4: Masking of water bodies improves the estimation of the in-orbit antenna pattern, provided that they do not extend across the entire image in the azimuth direction.

5.6 Implementation

As we will become apparent in Chapter 6, the method detailed in Section 5.3 gives smaller residual error than the NLA. This is generally the case for all rain forest scenes analyzed. The main reason is that the noisy uncompressed Null Line data only allows for an estimate with limited accuracy. The minimum "nulls" are often several hundred samples wide, which is why the best fit in the least squares sense often gives a better estimate of where the antenna is actually pointing. However, there are circumstances in which the most accurate pattern iteration is not identified as such (see Fig. 5.4.1, Fig. 5.5.2). In these cases, NLA usually outperforms the fitted Pattern. For this reason, a two pronged approach is implemented that uses both methods in parallel. The decision, which pattern to use is based on thresholding of the SSD (see Sec. 5.3). The flowchart in Figure 5.6.1 summarizes the steps involved in the antena pattern correction of SIR-C data. After successful application of the APCA, the Matlab-function returns the corrected SLC and the radiometric correction vector. This enables the end user to reverse the effects of antenna pattern correction if required. Additionally, the user can pass a number of comma separated input parameters to the Matlab function. The user inputs overwrite the information otherwise gathered from the raw data header. With this feature the user can optimize the antenna pattern correction for individual scenes manually. The input options are listed in Table 5.6.1.

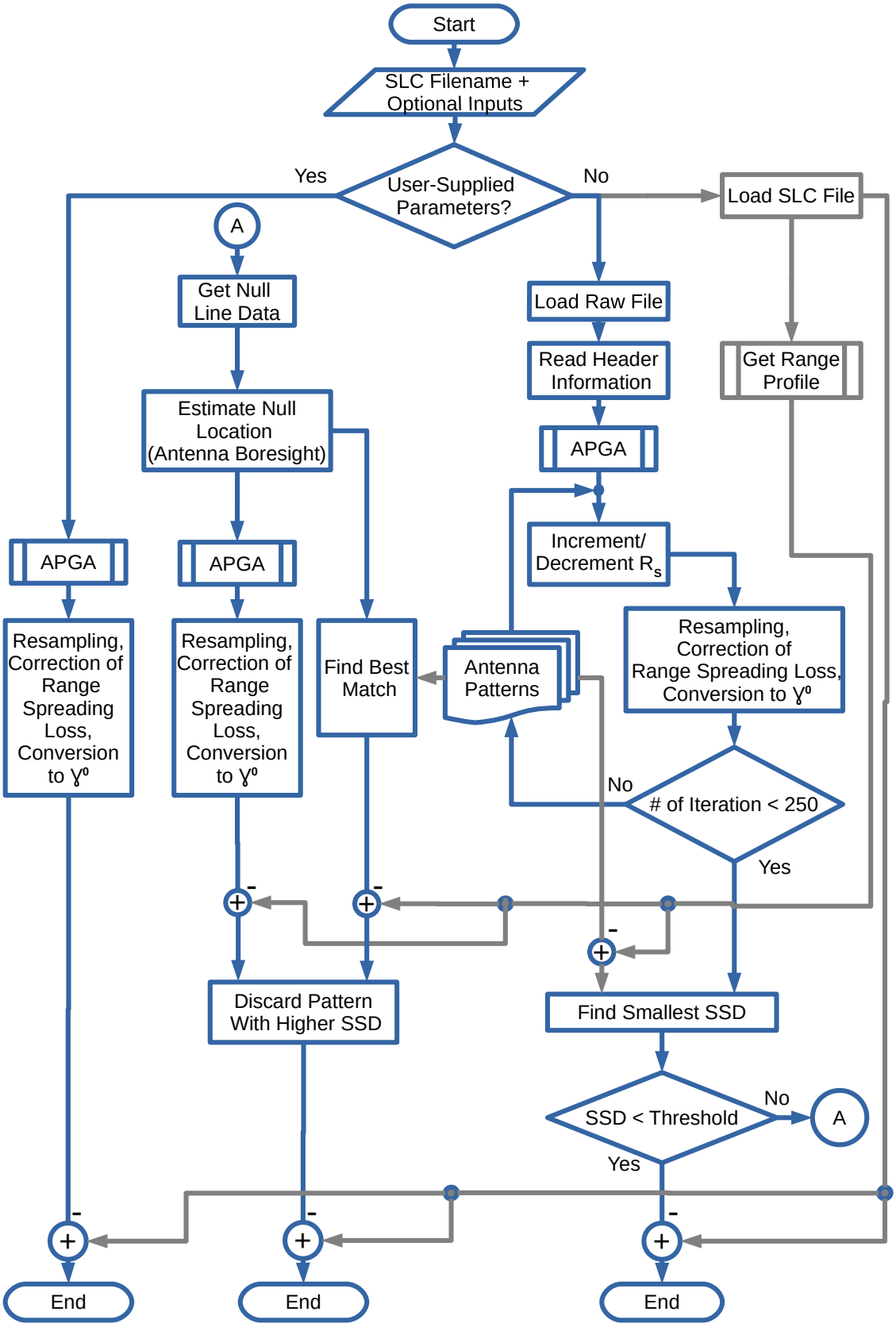

Figure 5.6.1: Process flow diagram of the antenna pattern correction algorithm. The blue arrows represent the direction of process flow, while the gray arrows indicate interfaces between different sub-processes.

Input parameter	Description:
indpol:	H-pol. pattern = 1, V-pol. pattern =0
indtr:	Transmit Pattern = 1, Receive pattern =0.
indnull:	Null beam: yes=1,no (default) = 0
indea:	Azimuth (0) or Elevation (1) pattern (Default = 1)
fixdeg:	Elevation(indea=0), Azimuth (indea=1) cut angle in degrees
eldeg:	Elevation pointing angle in degrees
azdeg:	Azimuth pointing angle in degrees
nsp:	Beamspoiling number (0 - 8)
ind:	Ideal pattern (1) or Testdata Pattern (2)
lAng	Boresight look angle in degrees
xlmin:	Minimum observation look angle in degrees
xlmax:	Maximum observation look angle in degrees
nang:	Number of samples in pattern
errThresh	Threshold for fitting error
ctvThresh	Threshold for cross track variation
skip2null	Skip straight to the alternative fitting method, where the antenna boresight is estimated with a Null line pulse.
passSLC	If the SLC is already in a matlab workspace, it can be passed directly after the optional input 'passSLC' to significantly speed up the runtime.

Table 5.6.1: Optional input parameters for the antenna pattern correction routine.

6 Performance Evaluation

In this chapter, the results of the antenna pattern correction are presented. Data from over 180 test sites and a total of 13 dataatakes were analyzed. The subset of images suitable for antenna pattern verification are tabulated in Section 6.2, while the full list of test cases is given in Appendix A. The availability of suitable test scenes varies depending on frequency and polarization since certain combinations were acquired more frequently than others. The most common acquisitions available for testing were C-band H-pol. data with a total of 56 individual (rain) forest scenes. Overall, the results are in accordance with the goal of $\pm 1\,\mathrm{dB}$ residual radiometric cross-swath uncertainty. Those cases, which are exceptionally different will be discussed in Section 6.3.

6.1 Antenna Model Verification Procedure (Elevation)

In order to verify the Antenna Model, the generated elevation patterns are compared with measured gamma profiles. The gamma profile, which is a vector of the mean antenna pattern over elevation angle (see Sec.4.1.3) [37], is derived from measurements across the rain forest. For verification over 40 different scenes from three datatakes acquired over the Amazon basin in Brazil (6.040-SRL-1, 103.060-SRL-1, 71.070-SRL-1) and an additional eight images of the Sub-Saharan rain forest (datatake 91.090-SRL-1) were selected. Figure 6.1.1 (a) depicts exemplary results, where the red and blue antenna patterns represent "Best Fit" and NLA respectively. The noisy green signal in Figures 6.1.1 (a) through (c) is the gamma profile before and after antenna pattern correction. By reducing the noise with a boxcar average filter (blue curve) a more accurate representation is obtained. Note, that the intensity of the gamma profile has been normalized for comparison purposes. The results show, that the deviation between antenna model and measurements is well within the stated goal of $\pm 1\,\mathrm{dB}$. The residual variation and consequently the accuracy of the antenna model range from $\pm 0.105\,\mathrm{dB}$ $[0.329\,\mathrm{dB}]$ (peak-to-peak) in the Amazon cases (no beamspoiling) to $\pm 0.763\,\mathrm{dB}$ $[0.932\,\mathrm{dB}]$ for Gabon (maximum beamspoiling). The numbers in the square brackets are the values obtained from NLA patterns. Results vary depending on frequency, polarization and degree of phase manipulation (electronic steering & beam spoiling). Co-polarized acquisitions usually show better agreement with the measured gamma profiles than their cross-polarized counterparts. In the general case, the actual error may be slightly higher since additional uncertainty is added if the relevant parameters are derived from non rain forest data.The estimates of the overall cross-swath calibration uncertainty are given in the following section.

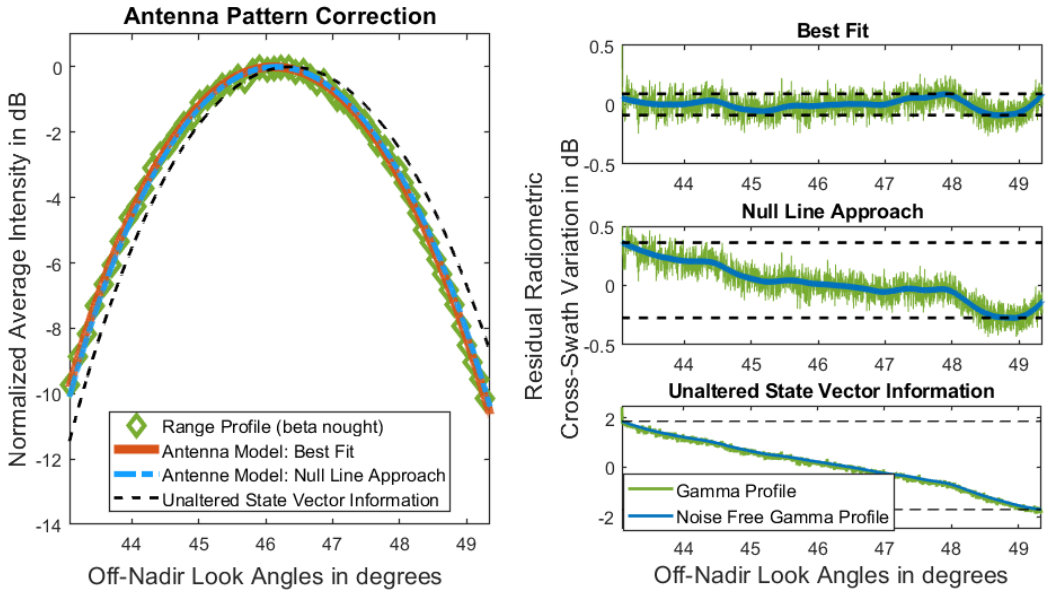

(a) Amazon rain forest scene C-band H-co-polarization for zero degree beam steering and no spoiling.

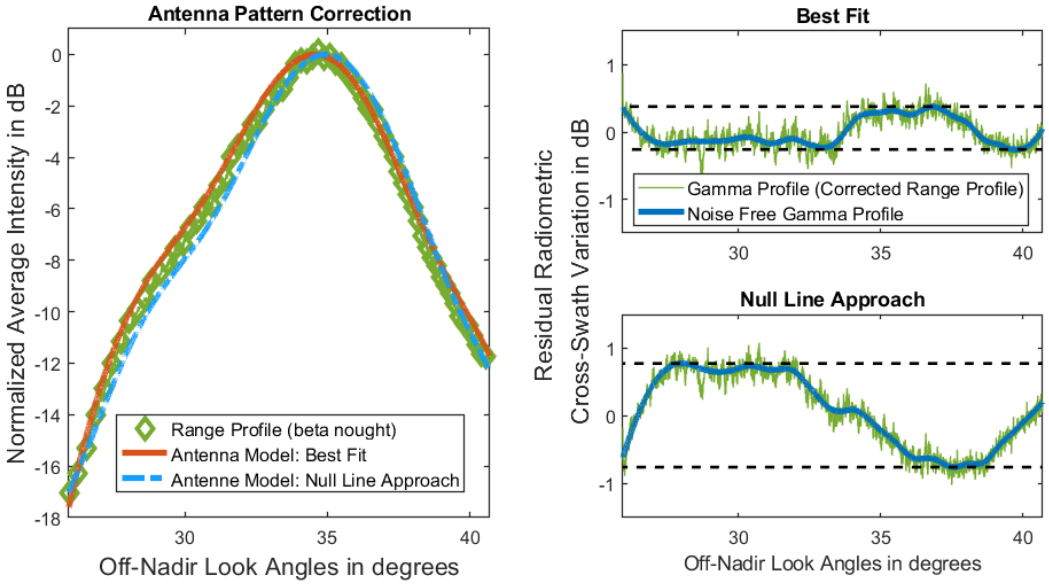

(b) Sub-Saharan rain forest scene C-band H-co-polarization for $5°$ of beam steering and $150°$ beam spoiling.

Figure 6.1.1: Exemplary results for antenna pattern correction. The plots on the left hand side each depict the gamma profile extracted from rain forest (green curve) and reference patterns for comparison. The plots on the right hand side represent the deviation between gamma profile and the individual reference patterns (green curve) and a filtered version of the deviation (blue line).

6.2 Evaluation

The estimates of the residual cross-swath uncertainties for SIR-C data were obtained by analyzing the APCA-results for over 50 selected sites depending on polarization and frequency. Tables 6.2.1 through 6.2.8 summarize the measurements for all rain forest scenes and a compilation of all available test results is included in Appendix A. Results obtained by three different methods are presented for reference: Best fit (BF) (see Sec. 5.3), NLA (see Sec. 5.5) and user-override, where all relevant parameters are taken directly from the header annotations (HA). Note that the final APCA will always return the result with the smallest cross-swath variation if no other user-specifications apply. The figures of merit[1] presented in Tables 6.2.1 through 6.2.8 are:

- Cross track variation (CTV), or peak-to-peak excursion, before the pattern correction is applied.
- Residual ranges of cross-track variation (RCTV), or peak-to-peak excursion, which is representative of the relative radiometric cross-swath uncertainty.
- The sum of squared differences (SSD), normalized by number of range samples, which is used as a metric for fit quality.

For reasons of readability, the figures of merit for a particular scene are color-coded in green for best-, yellow for second best- and red for worst result.

Granule ID (Acquisition Time)	CTV (uncorr.) in dB	RCTV (BF) in dB	RCTV (NLA) in dB	RCTV (HA) in dB	SSD (BF) in dB	SSD (NLA) in dB	SSD (HA) in dB
Datatake: 006.040-SRL-1-CHH: Bebedouro, Brazil. Elec. steering in el.: 5°. Beamspoiling: 0°.							
1994/04/09/19:11:11-19:11:23	4.803	±0.358	±0.77	±4.819	0.041	0.214	7.837
1994/04/09/19:11:22-19:11:34	4.405	±0.197	±0.768	±4.747	0.012	0.237	7.91
1994/04/09/19:11:34-19:11:46	4.278	±0.221	±0.818	±4.897	0.017	0.207	8.016
1994/04/09/19:11:45-19:11:57	3.613	±0.132	±0.517	±4.568	0.009	0.087	6.974
1994/04/09/19:11:57-19:12:09	3.861	±0.162	±0.61	±4.579	0.013	0.123	7.204
1994/04/09/19:12:08-19:12:20	4.223	±0.27	±0.825	±5.099	0.018	0.261	8.963
1994/04/09/19:12:20-19:12:32	4.479	±0.23	±0.845	±5.356	0.024	0.328	10.271
1994/04/09/19:12:31-19:12:43	4.092	±0.275	±0.646	±5.353	0.026	0.184	10.264
1994/04/09/19:12:43-19:12:55	3.855	±0.23	±0.42	±5.293	0.02	0.077	9.892
1994/04/09/19:12:54-19:13:06	4.235	±0.295	±0.621	±5.7	0.036	0.164	11.415
1994/04/09/19:13:06-19:13:18	4.519	±0.487	±0.803	±5.532	0.089	0.248	11.011
1994/04/09/19:13:17-19:13:29	3.93	±0.502	±0.497	±4.999	0.067	0.066	8.058
1994/04/09/19:13:40-19:13:52	4.154	±0.356	±0.592	±5.24	0.041	0.149	9.845
1994/04/09/19:13:46-19:13:58	3.773	±0.55	±0.649	±5.034	0.099	0.223	9.587

[1]The SLCs produced by the current version of the SIR-C processor have a trailing section of garbage pixels at far range. To avoid distortions, RCTV and SSD were calculated using only the first 90 percent of range samples.

Datatake: 031.030-SRL-1-CHH: Northwest China. Elec. steering in el.: $-3°$. Beamspoiling: $120°$.							
1994/04/11/07:58:16-07:58:31	9.865	±0.648	±0.834	±2.134	0.144	0.249	1.662
Datatake: 034.031-SRL-1-CHH: Elec. steering in el.: $10°$. Beamspoiling: $0°$.							
1994/10/02/12:32:36-12:32:50	13.552	±0.651	±0.809	±3.555	0.091	0.106	3.439
1994/10/02/12:33:31-12:33:46	11.247	±0.629	±0.928	±4.388	0.074	0.194	5.249
1994/10/02/12:33:59-12:34:13	11.945	±0.716	±0.775	±3.344	0.152	0.161	2.904
1994/10/02/12:34:13-12:34:27	11.136	±0.575	±0.677	±3.59	0.102	0.123	3.486
Datatake: 071.070-SRL-1-CHH: Sena Madureira, Brazil. Elec. steering in el.: $17°$. Beamspoiling: $0°$.							
1994/04/13/19:29:41-19:29:54	5.185	±0.137	±0.729	±1.314	0.008	0.186	0.595
1994/04/13/19:29:53-19:30:06	5.07	±0.305	±0.945	±1.389	0.024	0.247	0.608
Datatake: 091.090-SRL-1-CHH: Gabon and Cameroon. Elec. steering in el.: $-5°$. Beamspoiling: $150°$.							
1994/04/15/01:43:32-01:43:47	19.564	±0.532	±0.932	±1.74	0.057	0.22	0.354
1994/04/15/01:43:47-01:44:02	18.122	±0.604	±0.967	±1.413	0.091	0.341	0.303
1994/04/15/01:44:01-01:44:16	17.324	±0.425	±0.877	±1.033	0.06	0.318	0.191
1994/04/15/01:44:15-01:44:30	17.219	±0.398	±0.803	±1.011	0.057	0.3	0.172
1994/04/15/01:44:44-01:44:59	16.486	±0.686	±0.756	±0.918	0.149	0.186	0.222
1994/04/15/01:44:58-01:45:13	16.568	±0.4	±0.682	±1.204	0.055	0.162	0.48
1994/04/15/01:45:13-01:45:28	15.08	±0.728	±0.873	±0.72	0.081	0.303	0.186
1994/04/15/01:46:39-01:46:54	14.956	±0.763	±0.932	±1.39	0.146	0.186	0.343
Datatake: 103.060-SRL-1-CHH: Sena Madureira, Brazil. Elec. steering in el.: $6.5°$. Beamspoiling: $0°$.							
1994/04/15/18:45:12-18:45:24	9.437	±0.112	±0.458	±1.487	0.007	0.06	0.647
1994/04/15/18:45:23-18:45:35	9.475	±0.105	±0.329	±1.661	0.007	0.028	0.792
1994/04/15/18:45:35-18:45:47	9.607	±0.183	±0.37	±1.647	0.007	0.034	0.839
1994/04/15/18:45:46-18:45:58	9.901	±0.255	±0.871	±1.863	0.02	0.255	1.091
1994/04/15/18:45:58-18:46:10	9.726	±0.258	±0.656	±1.857	0.014	0.177	1.106
1994/04/15/18:46:09-18:46:21	9.98	±0.17	±0.814	±1.863	0.006	0.244	1.04
1994/04/15/18:46:21-18:46:33	10.365	±0.142	±0.481	±1.801	0.008	0.077	0.956
1994/04/15/18:46:32-18:46:44	9.364	±0.313	±0.793	±1.47	0.026	0.189	0.59
1994/04/15/18:46:44-18:46:56	9.209	±0.315	±0.513	±1.809	0.033	0.103	1.186
1994/04/15/18:47:07-18:47:19	10.133	±0.367	±0.7	±1.87	0.029	0.107	1.045
1994/04/15/18:47:18-18:47:30	10.456	±0.418	±0.711	±1.697	0.035	0.135	0.929
1994/04/15/18:47:30-18:47:42	10.045	±0.536	±0.53	±2.037	0.053	0.04	0.962
1994/04/15/18:47:41-18:47:53	9.989	±0.478	±0.527	±1.878	0.057	0.093	1.075
1994/04/15/18:47:53-18:48:05	10.502	±0.569	±0.837	±1.154	0.115	0.198	0.325
1994/04/15/18:48:04-18:48:16	10.321	±0.294	±0.609	±1.501	0.027	0.098	0.682
1994/04/15/18:48:16-18:48:28	9.523	±0.86	±0.8	±2.016	0.092	0.131	0.999
1994/04/15/18:48:27-18:48:39	10.029	±0.277	±0.428	±2.107	0.01	0.068	1.353
1994/04/15/18:48:39-18:48:51	10.382	±0.177	±0.417	±2.357	0.009	0.054	1.564
1994/04/15/18:48:50-18:49:02	10.546	±0.21	±0.555	±2.487	0.008	0.131	1.826
1994/04/15/18:49:02-18:49:14	10.58	±0.192	±0.33	±2.478	0.014	0.042	1.816
1994/04/15/18:49:13-18:49:26	10.909	±0.161	±0.339	±1.754	0.007	0.035	0.874
1994/04/15/18:49:25-18:49:37	10.423	±0.159	±0.519	±2.339	0.009	0.097	1.536
1994/04/15/18:49:36-18:49:49	10.324	±0.435	±0.422	±2.213	0.059	0.046	1.265

1994/04/15/18:49:48-18:50:00	11.252	±0.263	±0.948	±1.982	0.02	0.282	1.192
1994/04/15/18:50:11-18:50:23	13.303	±0.552	±0.755	±1.065	0.094	0.094	0.184
1994/04/15/18:50:23-18:50:35	13.32	±0.402	±0.733	±0.603	0.046	0.141	0.097
1994/04/15/18:50:46-18:50:58	14.102	±0.529	±0.606	±1.24	0.051	0.052	0.268

Table 6.2.1: Test results for C-band antenna, HH-co-polarized data.

Granule ID (Acquisition Time)	CTV (uncorr.) in dB	RCTV (BF) in dB	RCTV (NLA) in dB	RCTV (HA) in dB	SSD (BF) in dB	SSD (NLA) in dB	SSD (HA) in dB
Datatake: 006.040-SRL-1-CHV: Bebedouro, Brazil. Elec. steering in el.: 5°. Beamspoiling: 0°.							
1994/04/09/19:11:34-19:11:46	3.742	±0.197	±0.724	±4.427	0.017	0.157	6.524
1994/04/09/19:11:45-19:11:57	2.732	±0.198	±0.23	±3.946	0.017	0.023	5.218
1994/04/09/19:11:57-19:12:09	3.358	±0.145	±0.616	±4.251	0.008	0.11	6.031
1994/04/09/19:12:08-19:12:20	3.815	±0.175	±0.761	±4.695	0.012	0.233	7.889
1994/04/09/19:12:20-19:12:32	3.858	±0.171	±0.531	±4.855	0.013	0.142	8.474
1994/04/09/19:12:31-19:12:43	3.674	±0.263	±0.764	±4.897	0.025	0.258	8.882
1994/04/09/19:12:43-19:12:55	3.754	±0.321	±0.798	±4.942	0.044	0.312	8.811
1994/04/09/19:13:06-19:13:18	4.33	±0.444	±0.799	±5.258	0.086	0.274	10.015
1994/04/09/19:13:17-19:13:29	3.319	±0.516	±0.671	±4.522	0.075	0.111	6.303
1994/04/09/19:13:29-19:13:41	4.848	±0.469	±0.905	±5.664	0.079	0.43	12.125
1994/04/09/19:13:40-19:13:52	3.713	±0.333	±0.511	±4.859	0.04	0.103	8.621
1994/04/09/19:13:46-19:13:58	3.36	±0.465	±0.938	±4.717	0.076	0.501	8.409
Datatake: 034.031-SRL-1-CHV: Elec. steering in el.: 10°. Beamspoiling: 0°.							
1994/10/02/12:34:13-12:34:27	10.014	±0.588	±0.63	±3.045	0.082	0.091	2.628
Datatake: 103.060-SRL-1-CHV: Sena Madureira, Brazil. Elec. steering in el.: 6.5°. Beamspoiling: 0°.							
1994/04/15/18:45:12-18:45:24	9.11	±0.332	±0.332	±0.894	0.008	0.008	0.221
1994/04/15/18:45:23-18:45:35	9.183	±0.332	±0.317	±1.032	0.012	0.01	0.312
1994/04/15/18:45:35-18:45:47	9.376	±0.341	±0.341	±1.072	0.008	0.008	0.315
1994/04/15/18:45:46-18:45:58	9.498	±0.158	±0.356	±1.256	0.009	0.029	0.421
1994/04/15/18:45:58-18:46:10	9.233	±0.439	±0.43	±1.301	0.023	0.04	0.459
1994/04/15/18:46:09-18:46:21	9.706	±0.313	±0.524	±1.257	0.01	0.065	0.441
1994/04/15/18:46:21-18:46:33	9.931	±0.318	±0.318	±1.234	0.012	0.012	0.399
1994/04/15/18:46:32-18:46:44	8.941	±0.772	±0.8	±1.174	0.102	0.164	0.371
1994/04/15/18:46:44-18:46:56	8.367	±0.748	±0.649	±1.86	0.044	0.126	1.073
1994/04/15/18:46:55-18:47:07	9.653	±0.377	±0.413	±1.136	0.027	0.031	0.273
1994/04/15/18:47:07-18:47:19	9.204	±0.627	±0.593	±1.751	0.039	0.144	1.035
1994/04/15/18:47:18-18:47:30	10.114	±0.43	±0.43	±1.373	0.063	0.063	0.48
1994/04/15/18:47:30-18:47:42	9.983	±0.587	±0.587	±1.336	0.088	0.088	0.42
1994/04/15/18:47:41-18:47:53	9.439	±0.689	±0.609	±1.417	0.064	0.04	0.485
1994/04/15/18:47:53-18:48:05	10.357	±0.525	±0.57	±0.689	0.036	0.054	0.074
1994/04/15/18:48:04-18:48:16	9.944	±0.483	±0.38	±1.055	0.034	0.026	0.235

1994/04/15/18:48:16-18:48:28	8.942	±0.908	±0.886	±1.753	0.103	0.116	0.622
1994/04/15/18:48:27-18:48:39	9.872	±0.31	±0.279	±1.562	0.014	0.011	0.7
1994/04/15/18:48:39-18:48:51	10.28	±0.172	±0.172	±1.797	0.009	0.009	0.863
1994/04/15/18:48:50-18:49:02	10.324	±0.285	±0.323	±1.974	0.007	0.022	1.147
1994/04/15/18:49:02-18:49:14	10.228	±0.287	±0.278	±2.157	0.016	0.014	1.303
1994/04/15/18:49:13-18:49:26	10.506	±0.342	±0.342	±1.304	0.032	0.032	0.42
1994/04/15/18:49:25-18:49:37	10.202	±0.221	±0.286	±1.822	0.013	0.012	0.816
1994/04/15/18:49:36-18:49:49	9.927	±0.76	±0.77	±1.859	0.18	0.193	0.77
1994/04/15/18:49:48-18:50:00	10.723	±0.647	±0.818	±1.569	0.077	0.121	0.576
1994/04/15/18:50:00-18:50:12	11.407	±0.319	±0.746	±1.404	0.032	0.076	0.369
1994/04/15/18:50:11-18:50:23	11.718	±0.579	±0.783	±1.059	0.058	0.113	0.206
1994/04/15/18:50:23-18:50:35	12.161	±0.859	±0.99	±0.865	0.135	0.155	0.162

Table 6.2.2: Test results for C-band antenna, HV-cross-polarized data.

Granule ID (Acquisition Time)	CTV (uncorr.) in dB	RCTV (BF) in dB	RCTV (NLA) in dB	RCTV (HA) in dB	SSD (BF) in dB	SSD (NLA) in dB	SSD (HA) in dB
Datatake: 006.040-SRL-1-CVH: Bebedouro, Brazil. Elec. steering in el.: 5°. Beamspoiling: 0°.							
1994/04/09/19:11:11-19:11:23	4.655	±0.33	±0.606	±4.437	0.043	0.142	6.789
1994/04/09/19:11:22-19:11:34	3.894	±0.172	±0.208	±4.183	0.012	0.013	6.262
1994/04/09/19:11:34-19:11:46	3.928	±0.224	±0.765	±4.452	0.019	0.175	6.593
1994/04/09/19:11:45-19:11:57	2.931	±0.195	±0.224	±3.964	0.017	0.02	5.257
1994/04/09/19:11:57-19:12:09	3.541	±0.158	±0.214	±4.27	0.009	0.013	6.064
1994/04/09/19:12:08-19:12:20	3.997	±0.187	±0.305	±4.69	0.012	0.027	7.922
1994/04/09/19:12:20-19:12:32	4.072	±0.193	±0.468	±4.876	0.017	0.114	8.533
1994/04/09/19:12:31-19:12:43	3.863	±0.268	±0.353	±4.906	0.031	0.048	8.936
1994/04/09/19:12:43-19:12:55	3.919	±0.328	±0.353	±4.95	0.051	0.052	8.818
1994/04/09/19:12:54-19:13:06	4.212	±0.387	±0.549	±5.264	0.074	0.118	9.837
1994/04/09/19:13:06-19:13:18	4.533	±0.483	±0.741	±5.255	0.097	0.217	9.988
1994/04/09/19:13:17-19:13:29	3.51	±0.49	±0.652	±4.509	0.074	0.109	6.286
1994/04/09/19:13:29-19:13:41	5.068	±0.469	±0.761	±5.673	0.085	0.289	12.145
1994/04/09/19:13:40-19:13:52	3.9	±0.352	±0.571	±4.852	0.041	0.139	8.625
1994/04/09/19:13:46-19:13:58	3.529	±0.492	±0.449	±4.708	0.085	0.069	8.408

Table 6.2.3: Test results for C-band antenna, VH-co-polarization data.

Granule ID	CTV	RCTV	RCTV	RCTV	SSD	SSD	SSD

(Acquisition Time)	(uncorr.) in dB	(BF) in dB	(NLA) in dB	(HA) in dB	(BF) in dB	(NLA) in dB	(HA) in dB
Datatake: 006.040-SRL-1-CVV: Bebedouro, Brazil. Elec. steering in el.: 5°. Beamspoiling: 0°.							
1994/04/09/19:11:45-19:11:57	2.895	±0.174	±0.955	±3.735	0.015	0.299	4.664
1994/04/09/19:11:57-19:12:09	3.374	±0.156	±0.963	±4.057	0.009	0.261	5.32
1994/04/09/19:12:43-19:12:55	3.785	±0.329	±0.807	±4.701	0.043	0.283	7.853
1994/04/09/19:12:54-19:13:06	4.03	±0.356	±0.914	±5.059	0.061	0.347	9.225
1994/04/09/19:13:46-19:13:58	3.385	±0.402	±0.94	±4.568	0.056	0.445	7.606

Table 6.2.4: Test results for C-band antenna, VV-co-polarized data.

Granule ID (Acquisition Time)	CTV (uncorr.) in dB	RCTV (BF) in dB	RCTV (NLA) in dB	RCTV (HA) in dB	SSD (BF) in dB	SSD (NLA) in dB	SSD (HA) in dB
Datatake: 006.040-SRL-1-LHH: Bebedouro, Brazil. Elec. steering in el.: 5°. Beamspoiling: 0°.							
1994/04/09/19:11:11-19:11:23	5.488	±0.312	±0.229	±3.318	0.03	0.02	3.641
1994/04/09/19:11:22-19:11:34	5.673	±0.203	±0.263	±3.549	0.016	0.028	4.495
1994/04/09/19:11:34-19:11:46	6.404	±0.428	±0.533	±3.817	0.054	0.068	4.941
1994/04/09/19:11:45-19:11:57	4.599	±0.203	±0.214	±2.98	0.019	0.019	3.038
1994/04/09/19:11:57-19:12:09	5.576	±0.326	±0.26	±3.527	0.043	0.024	4.188
1994/04/09/19:12:08-19:12:20	5.743	±0.372	±0.36	±3.877	0.036	0.034	5.23
1994/04/09/19:12:20-19:12:32	5.897	±0.366	±0.342	±4.014	0.036	0.033	5.613
1994/04/09/19:12:31-19:12:43	4.962	±0.469	±0.553	±3.685	0.079	0.073	5.293
1994/04/09/19:12:43-19:12:55	5.563	±0.5	±0.478	±3.945	0.088	0.053	5.832
1994/04/09/19:12:54-19:13:06	5.732	±0.412	±0.323	±4.447	0.043	0.028	6.489
1994/04/09/19:13:06-19:13:18	5.742	±0.785	±0.821	±3.688	0.215	0.234	5.322
1994/04/09/19:13:17-19:13:29	4.934	±0.802	±0.889	±3.612	0.136	0.175	3.368
1994/04/09/19:13:46-19:13:58	5.109	±0.537	±0.576	±4.059	0.093	0.134	6.24
Datatake: 071.070-SRL-1-LHH: Sena Madureira, Brazil. Elec. steering in el.: 17°. Beamspoiling: 0°.							
1994/04/13/19:29:41-19:29:54	4.911	±0.28	±0.389	±0.31	0.017	0.048	0.029
1994/04/13/19:29:53-19:30:06	4.542	±0.934	±0.948	±1.018	0.263	0.273	0.315
Datatake: 103.060-SRL-1-LHH: Sena Madureira, Brazil. Elec. steering in el.: 6.5°. Beamspoiling: 0°.							
1994/04/15/18:45:12-18:45:24	9.725	±0.178	±0.268	±0.64	0.011	0.028	0.098
1994/04/15/18:45:23-18:45:35	9.753	±0.141	±0.395	±0.569	0.008	0.046	0.07
1994/04/15/18:45:35-18:45:47	10.04	±0.284	±0.502	±0.613	0.029	0.106	0.088
1994/04/15/18:45:46-18:45:58	10.238	±0.455	±0.607	±0.634	0.051	0.087	0.095
1994/04/15/18:45:58-18:46:10	9.874	±0.435	±0.453	±0.541	0.045	0.071	0.054
1994/04/15/18:46:09-18:46:21	10.437	±0.369	±0.569	±0.557	0.033	0.111	0.06
1994/04/15/18:46:21-18:46:33	10.904	±0.456	±0.54	±0.782	0.064	0.089	0.114
1994/04/15/18:46:32-18:46:44	9.777	±0.723	±0.836	±0.763	0.147	0.209	0.197
1994/04/15/18:47:07-18:47:19	9.405	±0.742	±0.742	±0.836	0.139	0.139	0.189

1994/04/15/18:47:30-18:47:42	11.375	±0.813	±0.813	±0.994	0.166	0.166	0.311
1994/04/15/18:47:41-18:47:53	11.645	±0.573	±0.599	±1.167	0.074	0.087	0.443
1994/04/15/18:47:53-18:48:05	11.533	±0.805	±0.649	±1.587	0.153	0.104	0.919
1994/04/15/18:48:04-18:48:16	12.506	±0.924	±0.98	±1.661	0.227	0.24	0.839
1994/04/15/18:48:27-18:48:39	10.931	±0.723	±0.253	±0.647	0.127	0.016	0.088
1994/04/15/18:48:39-18:48:51	11.023	±0.281	±0.265	±0.394	0.023	0.025	0.054
1994/04/15/18:48:50-18:49:02	11.754	±0.307	±0.321	±0.533	0.039	0.036	0.09
1994/04/15/18:49:02-18:49:14	11.452	±0.26	±0.362	±0.523	0.016	0.044	0.082
1994/04/15/18:49:13-18:49:26	11.857	±0.351	±0.359	±0.916	0.023	0.027	0.151
1994/04/15/18:49:25-18:49:37	10.871	±0.218	±0.252	±0.317	0.016	0.017	0.028
1994/04/15/18:50:11-18:50:23	14.57	±0.829	±0.806	±2.252	0.157	0.166	1.592
1994/04/15/18:50:46-18:50:58	16.2	±0.961	±0.961	±3.437	0.184	0.184	2.806

Table 6.2.5: Test results for L-band antenna, HH-co-polarized data.

Granule ID (Acquisition Time)	CTV (uncorr.) in dB	RCTV (BF) in dB	RCTV (NLA) in dB	RCTV (HA) in dB	SSD (BF) in dB	SSD (NLA) in dB	SSD (HA) in dB
Datatake: 006.040-SRL-1-LHV: Bebedouro, Brazil. Elec. steering in el.: 5°. Beamspoiling: 0°.							
1994/04/09/19:11:11-19:11:23	5.626	±0.35	±0.488	±3.247	0.039	0.078	3.544
1994/04/09/19:11:22-19:11:34	5.393	±0.53	±0.631	±3.21	0.077	0.096	3.375
1994/04/09/19:11:34-19:11:46	6.598	±0.635	±0.606	±3.786	0.11	0.106	4.398
1994/04/09/19:11:45-19:11:57	4.408	±0.392	±0.742	±2.745	0.061	0.213	2.545
1994/04/09/19:11:57-19:12:09	5.743	±0.292	±0.314	±3.581	0.032	0.041	4.029
1994/04/09/19:12:08-19:12:20	6.074	±0.351	±0.374	±3.908	0.037	0.035	5.387
1994/04/09/19:12:20-19:12:32	6.007	±0.435	±0.421	±3.894	0.053	0.051	5.231
1994/04/09/19:12:31-19:12:43	5.301	±0.608	±0.593	±3.774	0.126	0.134	5.472
1994/04/09/19:12:43-19:12:55	6.111	±0.621	±0.598	±4.108	0.149	0.141	6.746
1994/04/09/19:12:54-19:13:06	6.095	±0.606	±0.691	±4.262	0.13	0.161	6.287
1994/04/09/19:13:06-19:13:18	6.445	±0.804	±0.804	±4.106	0.239	0.239	6.395
1994/04/09/19:13:17-19:13:29	4.889	±0.757	±0.971	±3.521	0.147	0.259	3.299
1994/04/09/19:13:40-19:13:52	7.251	±0.656	±0.974	±4.396	0.142	0.23	8.173
1994/04/09/19:13:46-19:13:58	6.239	±0.473	±0.59	±4.414	0.098	0.11	7.111
Datatake: 103.060-SRL-1-LHV: Sena Madureira, Brazil. Elec. steering in el.: 6.5°. Beamspoiling: 0°.							
1994/04/15/18:45:12-18:45:24	8.748	±0.204	±0.841	±0.344	0.016	0.276	0.044
1994/04/15/18:45:23-18:45:35	8.722	±0.134	±0.952	±0.329	0.008	0.301	0.029
1994/04/15/18:45:58-18:46:10	8.311	±0.609	±0.85	±0.598	0.11	0.341	0.105
1994/04/15/18:46:09-18:46:21	9.481	±0.358	±0.928	±0.412	0.032	0.344	0.057
1994/04/15/18:46:21-18:46:33	9.708	±0.188	±0.97	±0.338	0.009	0.275	0.025
1994/04/15/18:47:41-18:47:53	10.882	±0.665	±0.702	±1.02	0.126	0.125	0.309
1994/04/15/18:48:27-18:48:39	9.889	±0.966	±0.543	±0.346	0.2	0.079	0.028

1994/04/15/18:48:39-18:48:51	9.844	±0.416	±0.844	±0.694	0.05	0.255	0.168
1994/04/15/18:48:50-18:49:02	10.465	±0.275	±0.666	±0.588	0.025	0.18	0.137
1994/04/15/18:49:13-18:49:26	10.618	±0.305	±0.638	±0.454	0.023	0.112	0.056
1994/04/15/18:49:25-18:49:37	10.008	±0.186	±0.656	±0.44	0.012	0.143	0.059

Table 6.2.6: Test results for L-band antenna, HV-cross-polarized data.

Granule ID (Acquisition Time)	CTV (uncorr.) in dB	RCTV (BF) in dB	RCTV (NLA) in dB	RCTV (HA) in dB	SSD (BF) in dB	SSD (NLA) in dB	SSD (HA) in dB
Datatake: 006.040-SRL-1-LVH: Bebedouro, Brazil. Elec. steering in el.: 5°. Beamspoiling: 0°.							
1994/04/09/19:11:11-19:11:23	5.708	±0.376	±0.342	±3.562	0.04	0.03	4.3
1994/04/09/19:11:22-19:11:34	5.463	±0.535	±0.575	±3.532	0.078	0.083	4.104
1994/04/09/19:11:34-19:11:46	6.705	±0.642	±0.73	±4.135	0.115	0.096	5.273
1994/04/09/19:11:45-19:11:57	4.483	±0.388	±0.397	±3.054	0.06	0.061	3.182
1994/04/09/19:11:57-19:12:09	5.818	±0.272	±0.323	±3.887	0.03	0.027	4.831
1994/04/09/19:12:08-19:12:20	6.153	±0.352	±0.733	±4.216	0.037	0.133	6.371
1994/04/09/19:12:20-19:12:32	6.128	±0.452	±0.52	±4.216	0.057	0.065	6.133
1994/04/09/19:12:31-19:12:43	5.379	±0.601	±0.629	±4.057	0.128	0.118	6.376
1994/04/09/19:12:43-19:12:55	6.199	±0.624	±0.729	±4.437	0.154	0.213	7.79
1994/04/09/19:12:54-19:13:06	6.202	±0.625	±0.678	±4.602	0.133	0.145	7.291
1994/04/09/19:13:06-19:13:18	6.542	±0.831	±0.771	±4.403	0.252	0.177	7.368
1994/04/09/19:13:17-19:13:29	4.978	±0.765	±0.799	±3.852	0.147	0.17	3.991
1994/04/09/19:13:46-19:13:58	6.333	±0.473	±0.99	±4.725	0.097	0.28	8.115

Table 6.2.7: Test results for L-band antenna, VH-cross-polarized data.

Granule ID (Acquisition Time)	CTV (uncorr.) in dB	RCTV (BF) in dB	RCTV (NLA) in dB	RCTV (HA) in dB	SSD (BF) in dB	SSD (NLA) in dB	SSD (HA) in dB
Datatake: 006.040-SRL-1-LVV: Bebedouro, Brazil. Elec. steering in el.: 5°. Beamspoiling: 0°.							
1994/04/09/19:11:11-19:11:23	6.509	±0.374	±0.365	±3.935	0.049	0.037	5.235
1994/04/09/19:11:22-19:11:34	6.143	±0.236	±0.249	±3.804	0.023	0.023	4.942
1994/04/09/19:11:34-19:11:46	7.121	±0.524	±0.626	±4.331	0.088	0.073	5.894
1994/04/09/19:11:45-19:11:57	5.123	±0.302	±0.341	±3.33	0.036	0.044	3.775
1994/04/09/19:11:57-19:12:09	6.433	±0.204	±0.225	±4.166	0.014	0.017	5.387
1994/04/09/19:12:08-19:12:20	6.569	±0.381	±0.437	±4.333	0.044	0.048	6.556
1994/04/09/19:12:20-19:12:32	6.491	±0.418	±0.397	±4.371	0.052	0.04	6.64

1994/04/09/19:12:31-19:12:43	5.737	±0.451	±0.491	±4.308	0.088	0.084	7.081
1994/04/09/19:12:43-19:12:55	6.531	±0.683	±0.624	±4.54	0.202	0.138	7.742
1994/04/09/19:12:54-19:13:06	6.71	±0.638	±0.555	±4.814	0.137	0.105	8.524
1994/04/09/19:13:06-19:13:18	6.704	±0.703	±0.658	±4.504	0.185	0.144	7.487
1994/04/09/19:13:17-19:13:29	5.732	±0.769	±0.807	±4.156	0.121	0.162	4.775
1994/04/09/19:13:29-19:13:41	7.805	±0.529	±0.963	±5.303	0.1	0.442	11.068
1994/04/09/19:13:40-19:13:52	7.477	±0.522	±0.946	±4.962	0.094	0.276	9.148
1994/04/09/19:13:46-19:13:58	6.317	±0.507	±0.688	±4.638	0.085	0.162	7.819

Table 6.2.8: Test results for L-band antenna, VV-co-polarized data.

SIR-C images (granules) are identified by Greenwich Mean Time (GMT) at the start and the end of the acquisition. In Tables 6.2.1 through 6.2.8, column 2 contains the peak to peak excursion in the uncorrected gamma profile. The remaining columns contain residual cross track variation (RCTV) and sum of squared differences (SSD) for best fit in the least squares sense (BF), Null Line Approach (NLA) and user-override, where all relevant parameters are taken directly from the header annotations (HA).The values in column five (RCTV, HA) show, that calibration without additional methods for parameter-error-compensation is not possible. As for "Best Fit", the antenna pattern correction algorithm shows excellent results, that is, the estimated errors at all frequencies and polarization exceeded JPL requirements. This is also true for the Null Line Approach. Even though the results for NLA consistently fall short of the BF-benchmark, its performance on flat, uniform rain forest data was shown to be adequate. Since the approach does not rely on the gamma profile for look angle estimation, it can be concluded, that NLA will deliver valid results for any other regular scene as well. The average residual errors for L-band and C-band are summarized in Table 6.2.9. From the examplary case in Figure 6.2.1, it is apparent that the algorithm successfully

Frequency and Polarization	Average Residual Cross-Track Variation for Best Fit in the Least Squares Sense [NLA] in dB
CHH	±0.35 [0.63]
CHV	±0.43 [0.56]
CVH	±0.31 [0.48]
CVV	±0.28 [0.92]
LHH	±0.49 [0.77]
LHV	±0.47 [0.69]
LVH	±0.53 [0.63]
LVV	±0.48 [0.56]

Table 6.2.9: Estimated relative radiometric cross-swath uncertainty for SIR-C data (average).

eliminates the antenna elevation characteristics in the SAR image.

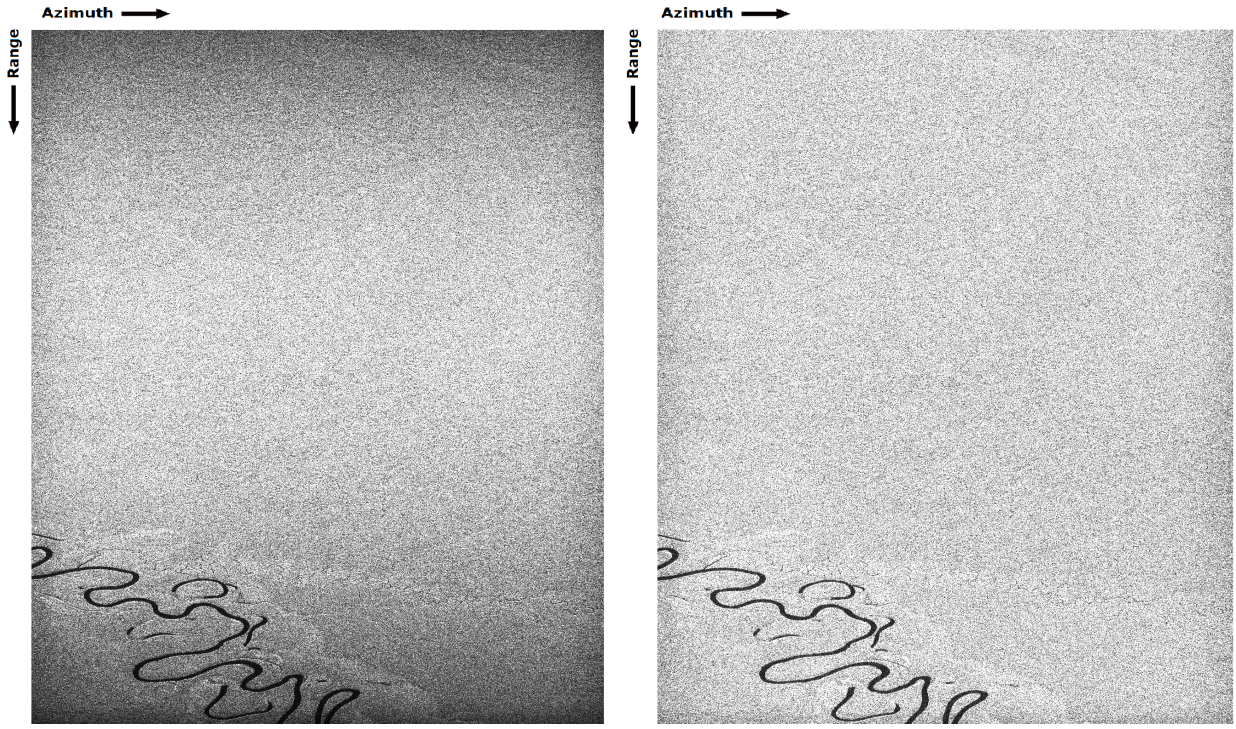

(a) (b)

Figure 6.2.1: Antenna elevation pattern spanning over range: (a) Before antenna pattern correction. (b) After antenna pattern correction.

6.3 Error Evaluation

The uncertainties involved in the APCA can be divided into two general categories: Uncertainty in the Antenna Model and uncertainty in the derivation of relevant parameters (look angles, altitude etc.). The largest contribution to antenna model uncertainty comes from the deviations between commanded vs. measured phases shifts which are approximated as static offsets in the pattern generation software. This is supported by the observation, that performance of the antenna model degrades with the level of phase manipulation (steering, beam spoiling) employed during acquisition. The agreement between modeled and measured antenna patterns, for example, were found to be worse at extreme off-broadside angles in elevation (>17°). Evidence of this phenomenon can be seen in the results of the wide-swath datatake 091.090-SRL-1 in Table 6.2.1. An explanation for this is given in [4].
Despite these previous factors, the antenna model was verified in Section 6.1 to have surprising accuracy. Instead, limited knowledge of the viewing geometry is the major source of calibration error. The effects of uncertainty in the available platform position data were noted in Section 5.2 and are corroborated by the observations of [15], [38] and [39].

Further inaccuracies in the radiometric cross-swath correction may be introduced as a result of

sine and cosine correction in the process of deriving the gamma profile. The conversion to gamma nought requires knowledge of the local incidence angle, and consequently a surface elevation model of the earth. It should be noted that, the standard method based on a reference ellipsoid only provides a rough approximation of the local surface topography.

6.3.1 Exceptions and Limitations

Fortunately, most SIR-C image products exceed the cross swath the requirements of $\pm 1\,\mathrm{dB}$ relative cross-swath calibration. There are however, exceptions for which the relative cross swatch calibration uncertainties may be greater than those quoted above. The exceptions were reported by the JPL Calibration team during the data processing [27, 4]. They are:

1. Large cross-swath errors were observed in data-takes, for which the antenna elevation angles exceed $\pm 17^\circ$ off broadside (wide-swath and/or electronic steering).

2. Altitude error or certain topographic effects may result in significant radiometric cross-swath aberration. This problem occurs for example if a coastal plain and a mountain range at high elevation is covered in the same scene. In processing, the standard approach for SIR-C data is to asume a constant altitude. This can cause additional errors in the calculation of the look angles θ_i. In [39], Holecz et al. suggest that the radiometric errors introduced by terrain variations may exceed $5\,\mathrm{dB}$ in the most extreme cases.

3. Data-takes with strong interference signatures (see Fig. 6.3.2 (a)) may suffer from large calibration errors.

6.3.2 Anomalies

There are, some minor anomalies in a small percentage of the SIR-C data collection. While most SIR-C products exceed all their image quality requirements [3], these anomoalies may lead to greater calibration uncertainty as well. Note, that the following account is not comprehensive:

Incorrect Receiver Gain Settings

In some datatakes the low noise receiver amplifiers were saturated, while other echoes were too weak. Low receiver gain setting resulted in poor SNR (Fig. 6.3.1) to a point where in some extreme cases the returned echoes were overwhelmed by the caltone signals embedded in the receiver gain [3].

Datatake 169.1-SRL-1 through 175.32-SRL-1

For data-takes 169.1-SRL-1 through 175.32-SRL-1, redundant hardware was used on the day of the acquisition. According to JPL-Documentation [27] this causes problems with the processor.

Device Failure

One C-band panel failed on the first flight and two failed on the second flight. Reportedly, the failure of C-band panels had only a minor impact on antenna performance and calibration[3].

Nadir Return

Nadir return occurs if a significant amount of energy, usually from the antenna side lobes, is reflected from the nadir point at the ground. If it falls into the receive widow of the pulse repetition cycle it, causes a bright streak in the image. The intensity may vary and the streak may be slightly skewed due to the change in the space shuttle's roll angle and altitude [40]. Nadir returns and transmitter interference were noticeable in a number of datatakes with very wide swaths (see Fig. 6.3.2 (a) and (b)).

Nadir return shows up as a thin bright image line in the along-track direction. Nadir return occurs when a sidelobe of the range antenna pattern is directed toward the nadir of the space shuttle, which results in an undesirable strong radar return recorded into the data window.

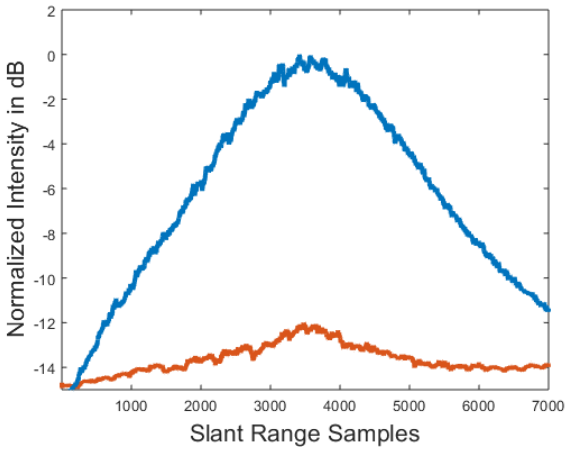

Figure 6.3.1: Incorrect receiver gain settings: The red curve represents the range profile of a SAR image that was acquired with very poor SNR due to incorrect receiver settings. For comparison, the blue curve depicts the range profile from another scene in the same datatake (same antenna beam settings), where the receiver provided sufficient amplification.

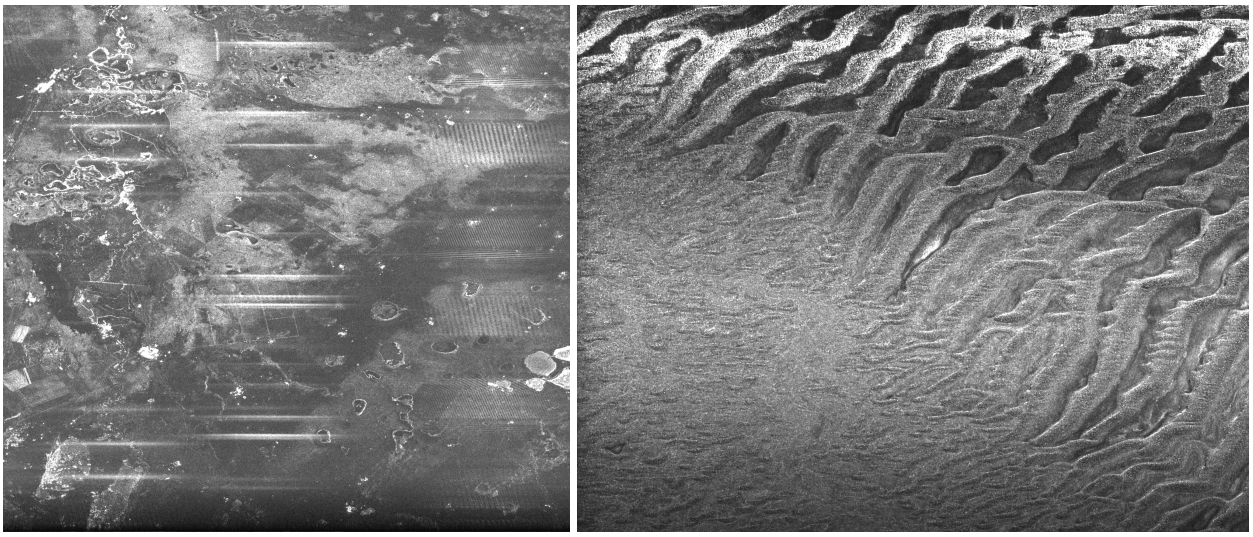

(a) Interference (b) Nadir return

Figure 6.3.2: Examples of interference and nadir return in SIR-C data.

7 Conclusion

Design and implementation of the SIR-C antenna pattern correction proved a challenging task. Two active phased array antennas enabled a high number of different acquisition modes, calling for a multitude of different antenna beams and hence antenna patterns. For this purpose, a model of the SIR-C antenna is used to generate reference patterns for the cross track amplitude variation in SIR-C SAR-images. Over relatively flat, uniform areas, it was shown that the residual cross-track amplitude variations were better than the goal of $\pm 1\,\mathrm{dB}$ (peak-to-peak).
A key issue of the pursued antenna model approach, is to cope with parameter uncertainty and high attitude drift rates. start it was clear, that the available attitude and position uncertainty was too high, to determine the antenna beamwidth and pointing direction with sufficient accuracy. The two most impactful parameters in terms of their contribution to the overall error and their potential for improvement, were identified as the shuttle roll angle and the position vector magnitude. This problem was tackled with a hybrid approach, in order to consider different cases depending on whether the overall error is predominantly caused by the roll angel or the shuttle position parameter. The best iteration is eventually determined by the smallest root mean square error. Tests with both L-band and C-band data demonstrated the final Antenna Pattern Correction Algorithm to be fully operational for all normal swath- and reduced swath modes of SIR-C. The results obtained from the Amazon rain forest achieved excellent accuracy, with residual ranges of radiometric cross-swath variation as low as $\pm 0.105\,\mathrm{dB}$. The rain forest results are consistent with the original calibration report [4] and show that the antenna model approach was successfully applied.
The developed algorithm therefore represents a step forward towards retrieving the SIR-C data collection and providing high resolution radiometrically calibrated SIR-C images to the public. The effort invested in reducing uncertainties in radiometric SAR measurements is important because it allows a more accurate and dependable data exchange across missions. To this end, SIR-C data is particularly interesting with respect to Earth monitoring in L-band, since it provides better time continuity between the L-band sensors SEASAT (1978) and ALOS (2006-2011) [10]. To retrieve the historic SIR-C dataset, therefore means to finally close this significant gap in Earth monitoring.

Glossary

AF	Array Factor
AGP	Antenna Gain Pattern
ALOS	Advanced Land Observing Satellite
APCA	Antenna Pattern Correction Algorithm
APGA	Antenna Pattern Generation Algorithm
APGS	Antenna Pattern Generation Software
ASF	Alaska Satellite Facility
BF	Best Fit
CTV	Cross Track Variation
DEM	Digital Elevation Model
DFM	Device Failure Map
DFT	Discrete Fourier Transform
DWP	Data Window Position
ECR	Earth Center Rotational (Coordinate-System)
FFT	Fast Fourier Transform
FM	Frequency Modulation
HA	Header Annotations
IFFT	Inverse Fast Fourier Transform
IRW	Impulse Response Width
JPL	Jet Propulsion Laboratory
MLC	Multi Look Complex
MOS	Mission Operation Subsystem
NASA	National Aeronautics and Space Administration

NISAR	NASA-ISRO (Indian Space Research Organisation) Synthetic Aperture Radar
NLA	Null Line Apprpach
PARC	Polarimetric Active Radar Calibratiors
PATH	Post-Flight Attitude and Trajectory History
PRF	Pulse Repetition Frequency
PRI	Pulse Repetition Interval
RADAR	Radio Detection And Ranging
RCM	Range Cell Migration
RCMC	Range Cell Migration Correction
RCS	Radar Cross Section
RCTV	Residual Cross Track Variation
RDA	Range Doppler Algorithm
SAR	Synthetic Aperture Radar
SIR-C	Spaceborne Imaging Radar with Payload C
SLAR	Side Looking Airborne Radar
SLC	Single Look Complex
SNR	Signal to Noise Ratio
SRL	Space Radar Laboratory
SRTM	Shuttle Radar Topography Mission
SSD	Sum of Squared Differences
SSR	Sum of Squared Residuals
TR	Transmit Receive

Bibliography

[1] H. J. Kramer, "SIR-C/X-SAR Payload on STS-59 and STS-68 Missions," Accessed on: April 4, 2019. [Online]. Url: https://directory.eoportal.org/web/eoportal/satellite-missions/s/sir-c, 2002.

[2] R. L. Jordan, B. L. Huneycutt, and M. Werner, "The SIR-C/X-SAR Synthetic Aperture Radar system," *IEEE Transactions on Geoscience and Remote Sensing*, vol. 33, no. 4, pp. 829–839, July 1995.

[3] C. Y. Chang and et al., "SIR-C Ground Data Processing System Overview," Jet Propulsion Laboratory, Pasadena, Ca 91109, Tech. Rep., March 1997, JPL Document ID: D-14457.

[4] A. Freeman, M. Alves, B. Chapman, J. Cruz, Y. Kim, S. Shaffer, J. Sun, E. Turner, and K. Sarabandi, "SIR-C data quality and calibration results," *IEEE Transactions on Geoscience and Remote Sensing*, vol. 33, no. 4, pp. 848–857, July 1995.

[5] E. R. Stofan, D. L. Evans, C. Schmullius, B. Holt, J. J. Plaut, J. van Zyl, S. D. Wall, and J. Way, "Overview of results of Spaceborne Imaging Radar-C, X-Band Synthetic Aperture Radar (SIR-C/X-SAR)," *IEEE Transactions on Geoscience and Remote Sensing*, vol. 33, no. 4, pp. 817–828, July 1995.

[6] V. Gracheva, F. J. Meyer, S. A. Arko, and P. A. Rosen, "New applications of spaceborne imaging RADAR-C (SIR-C) data," in *2017 IEEE International Geoscience and Remote Sensing Symposium (IGARSS)*, July 2017, pp. 4076–4080.

[7] U. S. Geological Survey, "USGS EROS Archive - Radar - Spaceborne Imaging Radar C-band (SIR-C)," Accessed on: April 4, 2019. [Online]. Url: https://www.usgs.gov/centers/eros/science/usgs-eros-archive-radar-spaceborne-imaging-radar-c-band-sir-c?qt-science_center_objects=0#qt-science_center_objects.

[8] S. A. Arko, K. McCarthy, R. Tye, B. Thoman, and A. La Belle-Hamer, "The Alaska Satellite Facility Ground Station," in *Proc.12th International Conference on Space Operations*, 2012.

[9] B. J. Döring, "Traceable Radiometric Calibration of Synthetic Aperture Radars," Ph.D. dissertation, Fakultät für Elektrotechnik und Informationstechnik des Karlsruher Instituts für Technologie (KIT), February 2016.

[10] K. J. Arnoult, R. Gens, V. Gracheva, F. J. Meyer, and P. A. Rosen, "Processing of Spaceborne Imaging Radar-C (SIR-C) Data at Full Resolution," in *Abstract no. G41B-0689 presented at 2018 AGU Fall Meeting, Washington, D.C., 10-14 Dec.*, 2018.

[11] C. Y. Chang, "Shuttle Imaging Radar-C Ground Data Processing System Data Product Specifications," Jet Propulsion Laboratory, Pasadena, Ca 91109, Tech. Rep., November 1992, JPL Document ID: D-7193 Version 2.0.

[12] A. Moreira, P. Prats-Iraola, M. Younis, G. Krieger, I. Hajnsek, and K. P. Papathanassiou, "A tutorial on synthetic aperture radar," *IEEE Geoscience and Remote Sensing Magazine*, vol. 1, no. 1, pp. 6–43, March 2013.

[13] I. G. Cumming and F. H. Wong, *Digital Processing of Synthetic Aperture Radar Data: Algorithms and Implementation*. Artech House remote sensing library v. 1. Artech House, Norwood, 2005.

[14] J. C. Curlander and R. N. McDonough, *Synthetic Apertre Radar: Systems and Signal Processing*. John Wiley & Sons.Inc, New York, 1991.

[15] S. Zeitvogel, "Evaluation and Optimization of a Newly Developed SAR Processor for SIR-C Data Using Point Target Analysis," B. S. thesis, Institut für Hochfrequenztechnik und Elektronik, Karlsruhe Insitute of Technology, 2017.

[16] D. T. Sandwell, "SAR Image Formation: ERS SAR Processor Coded In Matlab," Accessed on: April 4, 2019. [Online]. Url: https://engineering.purdue.edu/~bethel/sar_image_formation.pdf, 2002.

[17] J. Wang and X. Liu, "Automatic Correction of Range Migration in SAR Imaging," *IEEE Geoscience and Remote Sensing Letters*, vol. 7, pp. 256 – 260, May 2010.

[18] W. D. Wirth, *Radar techniques using array antennas*. The Institution of Electrical Engineers, London, 2002.

[19] Y. Shen, "Antenna Phase Shifter Bits Calculation," JPL California Institue of Technology, Pasadena, Ca 91109, Tech. Rep., July 1992, JPL Interoffice Memorandum 3346-92-133.

[20] Jet Propulsion Laboratory, "Shuttle Imaging Radar-C Commands, Modes, Timing and Telemetry," JPL California Institue of Technology, Pasadena, Ca 91109, Tech. Rep., December 1995, JPL Document ID: D-9262 Revision C.

[21] C. Y. Chang and J. C. Curlander, "SIR-C Ground Data System and Processing Algorithm Design ," in *XVIIth ISPRS Congress Technical Commission II: Systems for Data Processing and Analysis*, vol. XXIX, no. B2, 1992, pp. 464–468.

[22] D. Perz and C. Chang, " SIR-C Ground Data Processing System Functional Requirements

Document," JPL California Institue of Technology, Pasadena, Ca 91109, Tech. Rep., November 1993, JPL Document ID: D-4892 Version 3.0.

[23] D. Small, "Flattening Gamma: Radiometric Terrain Correction for SAR Imagery," *IEEE Transactions on Geoscience and Remote Sensing*, vol. 49, no. 8, pp. 3081–3093, Aug 2011.

[24] R. K. Raney, T. Freeman, R. W. Hawkins, and R. Bamler, "A Plea for Radar Brightness," in *Proceedings of IGARSS '94 - 1994 IEEE International Geoscience and Remote Sensing Symposium*, vol. 2, Aug 1994, pp. 1090–1092 vol.2.

[25] C. Y. Chang, " SIR-C GDPS Algorithm Design Document," JPL California Institue of Technology, Pasadena, Ca 91109, Tech. Rep., February 1994, JPL Document ID: D-7194.

[26] K. El-Darymli, P. McGuire, E. Gill, D. Power, and C. Moloney, "Understanding the significance of radiometric calibration for Synthetic Aperture Radar Imagery," in *IEEE 27th Canadian Conference on Electrical and Computer Engineering (CCECE)*, 05 2014.

[27] E. O'Leary and A. Richardson, "SIR-C: RDC User Guide," Jet Propulsion Laboratory, Pasadena, Ca 91109, Tech. Rep., August 1996, JPL Document ID D-14454.

[28] A. Freeman, "SAR calibration: An overview," *Geoscience and Remote Sensing, IEEE Transactions on*, vol. 30, pp. 1107 – 1121, 12 1992.

[29] K. Sarabandi, L. E. Pierce, M. C. Dobson, F. T. Ulaby, J. M. Stiles, T. C. Chiu, R. De Roo, R. Hartikka, A. Zambetti, and A. Freeman, "Polarimetric Calibration of SIR-C Using Point and Distributed Targets," *Geoscience and Remote Sensing, IEEE Transactions on*, vol. 33, pp. 858 – 866, 08 1995.

[30] S. Shaffer, "SIR C Antenna Model Implementation," JPL California Institue of Technology, Pasadena, Ca 91109, Tech. Rep., July 1992, JPL Interoffice Memorandum 3346-92-000.

[31] Y. Kim, "SIR-C Phase shifter algorithm," JPL California Institue of Technology, Pasadena, Ca 91109, Tech. Rep., August 1991, JPL Interoffice Memorandum 3349-91-063.

[32] Y. Kim, "SIR-C SAF Full Probe Test Report," JPL California Institue of Technology, Pasadena, Ca 91109, Tech. Rep., July 1993, JPL Interoffice Memorandum 3349-93-038.

[33] R. Kinsey, "Phased Array Beam Spoiling Technique," in *Conference: Antennas and Propagation Society International Symposium, IEEE*, 08 1997, pp. 698 – 701 vol.2.

[34] Y. Kim, "SIR-C Stick Patterns," JPL California Institue of Technology, Pasadena, Ca 91109, Tech. Rep., November 1991, JPL Interoffice Memorandum 3349-91-119.

[35] J. E. Laycock and H. Laur, "ERS-1 SAR Antenna Pattern Estimation," european space agency, Tech. Rep., September 1994, ES-TN-DPE-OM-JLOl, Iss.1 Rev.1 .

[36] M. Shimada and A. Freeman, "A technique for Measurement of Spaceborne SAR Antenna Patterns Using Distributed Targets," *IEEE Transactions on Geoscience and Remote Sensing*, vol. 33, no. 1, pp. 100–114, Jan 1995.

[37] M. Bachmann, M. Schwerdt, and B. Bräutigam, "Accurate Antenna Pattern Modeling for Phased Array Antennas in SAR Applications - Demonstration on TerraSAR-X," *International Journal of Antennas and Propagation*, vol. 2009, pp. 1–9, April 2009.

[38] A. Freeman, J. Cruz, B. Chapman, M. Alves, J. Sun, M. Azeem, and S. Shaffer, "First results from SIR-C calibration," in *Proceedings of IGARSS '94 - 1994 IEEE International Geoscience and Remote Sensing Symposium*, vol. 2, Aug 1994, pp. 1079–1081 vol.2.

[39] F. Holecz, A. Freeman, and J. van Zyl, "Topographic Effects on the Antenna Gain Pattern Correction," in *Proceedings of IGARSS '95 - 1995 IEEE International Geoscience and Remote Sensing Symposium*, 01 1995, pp. 587 – 589 vol.1.

[40] P. Barrett, C. Chang, J. Levison, L. Nguyen, Q. Nguyen, D. Perz, B. Swift, E. Turner, G. Weaver, and J. Weirickand T. Wrigh, " SIR-C: GDPS User Guide," JPL California Institue of Technology, Pasadena, Ca 91109, Tech. Rep., March 1997, JPL Document ID: D-13626.

A Full Antenna Pattern Correction Test results

The following tables list the improvement in the cross-track radiometric variation due to antenna pattern correction for all available SIR-C images. Note that the following test sites are not necessarily suited for antenna pattern derivation. The residual ranges of cross-track variation therefore do not represent the actual relative radiometric cross-swath error.

Granule	CHH			CHV			LHH			LHV		
	CTV	RCTV	SSD	CTV	RCTV	SSD	CTV	RCTV	SSD	CTV	RCTV	SSD
1994/04/09/19:11:11-19:11:23	4.506	±0.298	0.041	4.179	±0.263	0.035	5.173	±0.24	0.03	5.217	±0.27	0.039
1994/04/09/19:11:22-19:11:34	4.095	±0.137	0.013	3.355	±0.134	0.014	5.401	±0.168	0.016	5.044	±0.45	0.077
1994/04/09/19:11:34-19:11:46	4.023	±0.174	0.017	3.493	±0.177	0.017	6.025	±0.362	0.054	6.166	±0.513	0.115
1994/04/09/19:11:45-19:11:57	3.396	±0.081	0.01	2.609	±0.139	0.017	4.285	±0.155	0.019	4.115	±0.358	0.061
1994/04/09/19:11:57-19:12:09	3.709	±0.129	0.013	3.196	±0.096	0.008	5.31	±0.286	0.043	5.498	±0.226	0.032
1994/04/09/19:12:08-19:12:20	3.884	±0.187	0.02	3.538	±0.11	0.012	5.358	±0.231	0.036	5.614	±0.243	0.037
1994/04/09/19:12:20-19:12:32	4.266	±0.21	0.024	3.65	±0.141	0.014	5.663	±0.295	0.036	5.807	±0.347	0.053
1994/04/09/19:12:31-19:12:43	3.985	±0.237	0.026	3.607	±0.233	0.026	4.842	±0.383	0.079	5.072	±0.429	0.128
1994/04/09/19:12:43-19:12:55	3.618	±0.201	0.023	3.52	±0.261	0.038	5.229	±0.441	0.088	5.846	±0.546	0.149
1994/04/09/19:12:54-19:13:06	3.969	±0.237	0.036	3.769	±0.341	0.064	5.397	±0.327	0.043	5.698	±0.5	0.13
1994/04/09/19:13:06-19:13:18	4.266	±0.45	0.094	4.12	±0.381	0.081	5.457	±0.705	0.18	6.179	±0.661	0.167
1994/04/09/19:13:17-19:13:29	3.595	±0.409	0.06	2.983	±0.405	0.075	4.408	±0.567	0.136	4.418	±0.521	0.147
1994/04/09/19:13:29-19:13:41	4.633	±0.233	0.041	4.703	±0.356	0.079	6.955	±0.378	0.082	7.27	±0.511	0.197
1994/04/09/19:13:40-19:13:52	3.823	±0.265	0.041	3.402	±0.291	0.04	6.812	±0.451	0.092	6.74	±0.566	0.142
1994/04/09/19:13:46-19:13:58	3.574	±0.447	0.099	3.172	±0.407	0.076	4.915	±0.345	0.114	5.904	±0.359	0.098
Average:	3.956	±0.246	0.037	3.553	±0.249	0.04	5.415	±0.356	0.07	5.639	±0.433	0.105

Table A.1: Test results for datatake 006.040-SRL-1.

Granule	CHH			CHV			LHH			LHV		
CTV	RCTV	SSD	CTV	RCTV	SSD	CTV	RCTV	SSD	CTV	RCTV	SSD	
1994/04/11/07:57:33-07:57:48	8.953	±0.989	0.23	6.535	±2.01	1.015	10.924	±1.007	0.432	10.806	±1.286	0.69
1994/04/11/07:57:47-07:58:02	11.118	±1.267	0.772	9.599	±1.852	1.276	12.909	±0.786	0.589	13.826	±1.972	1.124
1994/04/11/07:58:01-07:58:16	10.355	±0.931	0.292	8.311	±1.587	0.442	13.979	±1.02	0.439	14.673	±1.304	0.754
1994/04/11/07:58:16-07:58:31	9.474	±0.494	0.144	7.552	±1.359	0.465	11.687	±1.177	0.356	11.949	±1.272	0.366
1994/04/11/07:58:30-07:58:45	12.593	±0.979	0.509	9.251	±1.405	0.784	12.878	±1.358	0.562	13.555	±1.408	0.628

1994/04/11/07:58:44-07:58:59	11.191	±0.739	0.264	9.459	±1.092	0.417	13.174	±0.965	0.398	14.999	±1.953	1.676
1994/04/11/07:58:59-07:59:14	7.397	±1.63	0.753	-	-	-	9.974	±0.886	0.268	8.216	±1.611	0.595
1994/04/11/07:59:13-07:59:28	7.878	±2.909	1.909	-	-	-	9.872	±3.382	5.012	10.073	±1.844	0.81
1994/04/11/07:59:56-08:00:11	9.973	±4.678	4.021	-	-	-	12.987	±6.479	6.861	10.256	±3.795	3.113
1994/04/11/08:00:10-08:00:25	12.86	±0.713	0.285	9.387	±1.382	0.477	14.291	±1.152	0.446	15.081	±1.415	0.829
1994/04/11/08:00:25-08:00:40	13.205	±1.461	0.491	9.528	±2.465	1.381	15.536	±1.517	0.901	14.083	±1.862	1.438
1994/04/11/08:00:39-08:00:54	11.169	±1.014	0.42	10.442	±1.958	0.907	15.359	±2.579	2.059	14.363	±3.535	4.016
1994/04/11/08:00:53-08:01:08	9.902	±1.599	0.414	-	-	-	15.055	±2.027	1.622	11.856	±3.456	1.803
1994/04/11/08:01:08-08:01:23	10.112	±1.121	0.401	-	-	-	15.137	±1.217	0.411	8.577	±2.17	1.479
1994/04/11/08:01:22-08:01:37	11.485	±0.556	0.146	-	-	-	17.606	±1.688	1.008	11.149	±2.267	1.637
1994/04/11/08:01:36-08:01:51	11.935	±1.255	0.53	6.702	±3.19	3.858	16.809	±1.452	0.702	13.81	±2.409	1.91
1994/04/11/08:01:51-08:02:06	14.401	±0.679	0.244	9.576	±1.547	0.593	17.936	±1.767	1.518	17.551	±2.25	2.228
1994/04/11/08:02:05-08:02:20	11.687	±0.805	0.409	7.953	±2.467	1.612	14.458	±1.034	0.551	13.28	±0.905	0.463
1994/04/11/08:02:19-08:02:34	12.334	±1.249	0.703	8.791	±1.666	0.853	13.264	±1.187	0.896	14.228	±1.102	0.531
1994/04/11/08:02:34-08:02:49	12.507	±1.657	1.193	10.628	±1.425	0.851	13.865	±1.23	0.955	15.896	±1.72	1.248
1994/04/11/08:02:48-08:03:03	12.792	±2.065	1.632	10.424	±2.083	1.605	13.554	±1.14	0.674	15.137	±1.396	0.741
1994/04/11/08:03:02-08:03:17	14.134	±1.403	0.774	10.205	±1.736	0.678	15.386	±1.84	0.965	15.858	±1.755	0.797
1994/04/11/08:03:17-08:03:32	13.324	±1.731	1.21	10.853	±1.801	1.132	12.297	±1.543	0.946	13.714	±1.43	0.95
1994/04/11/08:03:31-08:03:46	10.17	±1.312	0.503	9.338	±1.358	0.539	10.299	±1.185	0.593	11.077	±1.21	0.578
1994/04/11/08:03:35-08:03:50	10.308	±1.279	0.376	10.319	±1.015	0.423	11.243	±1.146	0.481	11.305	±1.006	0.378
1994/04/11/07:59:27-07:59:42	-	-	-	-	-	-	-	-	-	6.937	±2.064	1.39
1994/04/11/07:59:42-07:59:57	-	-	-	-	-	-	-	-	-	8.148	±2.646	3.354
Average:	11.25	±1.381	0.745	9.203	±1.758	1.016	13.619	±1.63	1.186	12.607	±1.89	1.316

Table A.2: Test results for datatake 031.030-SRL-1.

Granule	CHH			CHV			LHH			LHV		
	CTV	RCTV	SSD	CTV	RCTV	SSD	CTV	RCTV	SSD	CTV	RCTV	SSD

1994/04/11/08:00:39-08:00:54	-	-	-	10.442	±1.958	0.907	-	-	-	-	-	-
1994/10/02/12:32:36-12:32:50	13.124	±0.515	0.091	11.096	±1.177	0.513	14.167	±1.089	0.443	8.429	±2.08	1.087
1994/10/02/12:32:49-12:33:04	12.618	±2.787	2.573	7.183	±1.995	1.221	13.229	±2.585	2.345	6.67	±2.02	1.375
1994/10/02/12:33:03-12:33:18	8.952	±0.664	0.168	6.436	±1.138	0.467	10.955	±1.199	0.347	6.001	±1.347	0.751
1994/10/02/12:33:17-12:33:32	10.974	±1.043	0.35	10.01	±0.643	0.121	11.323	±1.723	0.77	8.145	±1.376	0.588
1994/10/02/12:33:31-12:33:46	10.857	±0.511	0.074	9.397	±0.41	0.068	11.016	±0.557	0.138	8.216	±0.674	0.19
1994/10/02/12:33:45-12:34:00	10.47	±0.438	0.07	9.775	±0.508	0.086	12.663	±0.81	0.28	10.302	±0.907	0.33
1994/10/02/12:33:59-12:34:13	11.32	±0.634	0.152	10.141	±0.848	0.259	12.802	±1.067	0.353	9.905	±1.515	0.717
1994/10/02/12:34:13-12:34:27	10.602	±0.52	0.102	9.593	±0.498	0.074	10.722	±0.519	0.142	8.711	±0.838	0.26
1994/10/02/12:34:27-12:34:41	9.278	±0.577	0.132	8.738	±0.674	0.134	9.962	±0.907	0.32	7.708	±1.274	0.518
1994/10/02/12:34:41-12:34:55	7.381	±0.815	0.332	7.046	±0.868	0.229	8.336	±0.974	0.473	7.138	±0.871	0.322
1994/10/02/12:34:54-12:35:09	7.35	±0.926	0.346	6.409	±0.716	0.209	7.579	±1.038	0.376	6.884	±0.897	0.3
1994/10/02/12:35:08-12:35:23	8.122	±0.658	0.175	8.017	±0.599	0.114	9.381	±0.703	0.24	8.035	±0.912	0.276
1994/10/02/12:35:22-12:35:37	11.041	±3.532	4.173	-	-	-	11.439	±3.436	4.763	-	-	-
Average:	10.161	±1.048	0.672	8.791	±0.926	0.339	11.044	±1.277	0.845	8.012	±1.226	0.559

Table A.3: Test results for datatake 034.031-SRL-2.

Granule	CHH			CHV			LHH			LHV		
	CTV	RCTV	SSD	CTV	RCTV	SSD	CTV	RCTV	SSD	CTV	RCTV	SSD
1994/10/03/04:39:33-04:39:46	3.632	±0.613	0.124	2.026	±0.48	0.068	5.744	±1.226	0.673	-	-	-
1994/10/03/04:39:46-04:40:00	4.457	±0.577	0.114	2.465	±0.616	0.112	5.736	±1.848	1.295	-	-	-
1994/10/03/04:39:59-04:40:13	2.905	±0.803	0.198	-	-	-	-	-	-	-	-	-
1994/10/03/04:40:12-04:40:26	5.193	±0.787	0.228	2.285	±0.399	0.071	7.642	±1.829	1.222	-	-	-
1994/10/03/04:40:25-04:40:39	2.147	±0.579	0.141	-	-	-	-	-	-	-	-	-
1994/10/03/04:40:39-04:40:53	2.24	±0.773	0.252	-	-	-	-	-	-	-	-	-
1994/10/03/04:40:52-04:41:06	3.253	±0.691	0.185	2.733	±0.757	0.16	4.553	±1.481	0.931	-	-	-
1994/10/03/04:41:00-04:41:13	3.035	±0.784	0.164	2.339	±0.8	0.206	3.859	±1.257	0.808	-	-	-

Average:	3.358	±0.701	0.176	2.37	±0.61	0.123	5.507	±1.528	0.986	

Table A.4: Test results for datatake 045.020-SRL-2.

Granule	CHH			CHV			LHH			LHV		
	CTV	RCTV	SSD	CTV	RCTV	SSD	CTV	RCTV	SSD	CTV	RCTV	SSD
1994/04/12/09:06:57-09:07:11	5.489	±0.612	0.138	1.892	±0.509	0.088	-	-	-	2.887	±0.835	0.252
1994/04/12/09:07:10-09:07:25	4.104	±0.655	0.114	1.577	±0.595	0.076	5.538	±1.869	0.89	-	-	-
1994/04/12/09:07:24-09:07:39	4.133	±0.552	0.118	1.564	±0.625	0.171	-	-	-	2.315	±0.832	0.287
1994/04/12/09:07:38-09:07:53	4.737	±0.494	0.076	1.85	±0.606	0.127	5.627	±0.631	0.134	2.963	±0.658	0.084
1994/04/12/09:07:52-09:08:07	2.799	±0.569	0.116	-	-	-	4.245	±0.604	0.172	-	-	-
1994/04/12/09:08:06-09:08:21	4.809	±0.524	0.096	-	-	-	-	-	-	3.475	±1.037	0.331
1994/04/12/09:08:20-09:08:34	2.783	±0.859	0.204	1.161	±0.489	0.102	6.429	±1.864	1.242	-	-	-
1994/04/12/09:08:34-09:08:48	6.343	±0.977	0.314	1.681	±0.427	0.043	-	-	-	7.425	±0.787	0.171
1994/04/12/09:08:48-09:09:02	2.607	±0.402	0.053	-	-	-	4.269	±0.584	0.101	3.015	±0.493	0.096
1994/04/12/09:09:15-09:09:30	3.029	±0.176	0.014	-	-	-	3.644	±0.386	0.061	2.999	±0.441	0.061
1994/04/12/09:09:43-09:09:57	-	-	-	1.121	±0.553	0.099	5.044	±1.456	0.907	4.34	±1.105	0.458
1994/04/12/09:09:02-09:09:16	-	-	-	-	-	-	3.608	±0.652	0.096	3.022	±0.718	0.123
1994/04/12/09:09:29-09:09:44	-	-	-	-	-	-	-	-	-	3.051	±1.118	0.484
Average:	4.083	±0.582	0.124	1.549	±0.544	0.101	4.801	±1.006	0.45	3.549	±0.802	0.235

Table A.5: Test results for datatake 048.030-SRL-1.

Granule	CHH			CHV			LHH			LHV		
	CTV	RCTV	SSD	CTV	RCTV	SSD	CTV	RCTV	SSD	CTV	RCTV	SSD

1994/10/03/19:38:50-19:39:02	12.429	±1.024	0.331	11.647	±1.305	0.516	15.169	±2.067	1.421	14.34	±2.201	1.726
1994/10/03/19:39:01-19:39:14	11.979	±0.992	0.383	10.398	±1.013	0.294	13.785	±3.135	3.49	13.861	±1.99	1.519
1994/10/03/19:39:13-19:39:26	11.368	±0.519	0.122	10.406	±0.448	0.093	14.244	±1.108	0.618	13.682	±1.298	0.683
1994/10/03/19:39:25-19:39:38	11.56	±1.182	0.489	10.455	±1.568	0.843	14.953	±2.073	1.564	15.847	±2.306	2.176
1994/10/03/19:39:37-19:39:50	11.221	±0.789	0.256	10.555	±0.616	0.11	12.081	±1.307	0.606	11.608	±0.851	0.316
1994/10/03/19:39:49-19:40:02	11.075	±0.569	0.112	10.314	±0.385	0.061	11.408	±1.238	0.589	9.491	±0.898	0.355
1994/10/03/19:40:01-19:40:14	11.021	±0.221	0.036	10.123	±0.232	0.029	13.151	±1.327	0.722	13.335	±1.041	0.444
1994/10/03/19:40:13-19:40:26	11.426	±0.27	0.035	10.136	±0.362	0.056	11.888	±1.231	0.681	11.314	±0.811	0.185
1994/10/03/19:40:18-19:40:30	11.144	±0.237	0.026	10.468	±0.371	0.032	12.349	±0.822	0.244	11.872	±1.23	0.262
Average:	11.469	±0.645	0.199	10.5	±0.7	0.226	13.225	±1.59	1.104	12.817	±1.403	0.852

Table A.6: Test results for datatake 055.030-SRL-2.

Granule	CHH			CHV			LHH			LHV		
	CTV	RCTV	SSD	CTV	RCTV	SSD	CTV	RCTV	SSD	CTV	RCTV	SSD
1994/04/13/19:29:41-19:29:54	5.078	±0.123	0.008	-	-	-	4.808	±0.253	0.017	5.487	±0.263	0.024
1994/04/13/19:29:53-19:30:06	4.924	±0.269	0.024	-	-	-	4.309	±0.832	0.263	4.626	±0.989	0.393
Average:	5.001	±0.196	0.016				4.558	±0.543	0.14	5.057	±0.626	0.209

Table A.7: Test results for datatake 071.070-SRL-1.

Granule	CHH			CHV		
	CTV	RCTV	SSD	CTV	RCTV	SSD
1994/10/05/05:07:55-05:08:10	4.449	±0.304	0.045	3.992	±0.47	0.105
1994/10/05/05:08:09-05:08:24	5.14	±0.208	0.028	4.773	±0.337	0.052

1994/10/05/05:08:23-05:08:38	5.694	±0.135	0.02	5.28	±0.367	0.042
1994/10/05/05:08:38-05:08:53	5.86	±0.126	0.015	5.132	±0.266	0.048
1994/10/05/05:08:52-05:09:07	4.838	±0.407	0.064	3.97	±0.823	0.253
1994/10/05/05:09:06-05:09:21	5.693	±0.375	0.073	5.698	±0.514	0.094
1994/10/05/05:09:21-05:09:36	5.43	±0.368	0.063	5.2	±0.267	0.048
1994/10/05/05:09:35-05:09:50	4.929	±0.104	0.01	5.041	±0.218	0.025
1994/10/05/05:09:49-05:10:04	4.857	±0.223	0.022	4.531	±0.355	0.056
1994/10/05/05:10:04-05:10:19	5.075	±0.223	0.028	4.699	±0.221	0.023
1994/10/05/05:10:18-05:10:33	6.399	±0.886	0.244	5.569	±0.713	0.215
1994/10/05/05:10:32-05:10:47	3.543	±0.531	0.092	2.363	±0.901	0.238
1994/10/05/05:10:45-05:11:01	5.134	±0.145	0.012	3.622	±0.58	0.094
Average:	5.157	±0.31	0.055	4.605	±0.464	0.099

Table A.8: Test results for datatake 077.090-SRL-2.

Granule	CHH			CHV			LHH			LHV		
	CTV	RCTV	SSD	CTV	RCTV	SSD	CTV	RCTV	SSD	CTV	RCTV	SSD
1994/04/15/01:43:04-01:43:19	19.231	±3.658	3.71	11.468	±3.732	5.579	26.428	±3.174	4.975	26.923	±7.512	21.28
1994/04/15/01:43:18-01:43:33	22.888	±3.209	2.835	15.596	±3.761	2.943	29.895	±3.743	4.915	32.825	±8.45	38.667
1994/04/15/01:43:32-01:43:47	18.858	±0.423	0.057	14.914	±0.767	0.159	22.146	±0.965	0.399	22.732	±1.598	1.108
1994/04/15/01:43:47-01:44:02	17.429	±0.526	0.091	14.843	±1.096	0.247	19.291	±1.286	0.742	18.49	±1.04	0.552
1994/04/15/01:44:01-01:44:16	16.661	±0.373	0.06	14.662	±0.599	0.158	18.883	±1.206	0.654	17.784	±0.975	0.496
1994/04/15/01:44:15-01:44:30	16.539	±0.328	0.057	14.364	±0.664	0.173	18.82	±1.192	0.534	17.749	±0.894	0.417
1994/04/15/01:44:30-01:44:45	15.876	±0.36	0.058	14.072	±0.683	0.11	18.488	±1.116	0.547	18.081	±1.065	0.557
1994/04/15/01:44:44-01:44:59	15.935	±0.661	0.149	13.539	±0.91	0.474	18.432	±1.56	0.616	17.506	±1.222	0.613
1994/04/15/01:44:58-01:45:13	16.023	±0.378	0.055	14.051	±0.94	0.394	18.799	±1.682	0.821	18.523	±1.553	1.079
1994/04/15/01:45:13-01:45:28	14.454	±0.67	0.081	12.628	±1.163	0.247	17.65	±1.654	0.613	17.39	±1.133	0.556
1994/04/15/01:45:27-01:45:42	13.68	±0.598	0.071	11.646	±1.083	0.092	16.396	±1.022	0.39	15.445	±1.083	0.312
1994/04/15/01:45:41-01:45:56	15.701	±0.394	0.047	12.225	±1.39	0.216	19.014	±1.183	0.346	17.954	±1.334	0.478

1994/04/15/01:45:56-01:46:11	15.231	±0.729	0.07	10.275	±2.131	0.751	19.329	±1.785	0.601	18.33	±1.477	0.664
1994/04/15/01:46:10-01:46:25	14.395	±1.153	0.187	9.31	±2.367	1.066	19.539	±1.587	1.148	18.416	±1.526	0.927
1994/04/15/01:46:24-01:46:39	14.31	±1.175	0.144	9.356	±2.628	1.437	19.344	±1.829	1.256	18.586	±1.993	1.118
1994/04/15/01:46:39-01:46:54	14.555	±0.69	0.146	9.587	±2.352	1.208	19.186	±1.503	0.775	17.486	±0.865	0.32
1994/04/15/01:46:53-01:47:08	12.881	±1.107	0.276	7.575	±3.355	2.36	18.016	±1.298	0.633	16.528	±1.051	0.306
1994/04/15/01:47:07-01:47:22	11.222	±1.775	0.356	-	-	-	16.296	±1.261	0.505	13.91	±2.691	1.221
1994/04/15/01:47:22-01:47:37	10.404	±1.376	0.119	-	-	-	15.974	±1.031	0.468	11.611	±1.898	0.663
1994/04/15/01:47:36-01:47:51	8.347	±2.235	0.554	-	-	-	12.912	±1.048	0.218	-	-	-
1994/04/15/01:47:50-01:48:05	8.066	±2.489	0.561	-	-	-	13.199	±1.341	0.351	-	-	-
1994/04/15/01:48:05-01:48:20	7.518	±2.908	1.243	-	-	-	12.776	±1.527	0.602	-	-	-
1994/04/15/01:48:19-01:48:34	6.727	±3.242	1.64	-	-	-	11.437	±1.647	0.648	-	-	-
1994/04/15/01:48:33-01:48:48	7.379	±2.652	1.174	-	-	-	11.024	±1.369	0.584	-	-	-
1994/04/15/01:48:36-01:48:51	8.757	±1.97	1.325	-	-	-	12.71	±1.23	0.623	7.708	±2.098	1.134
Average:	13.723	±1.403	0.603	12.359	±1.742	1.036	17.839	±1.53	0.959	18.199	±2.073	3.623

Table A.9: Test results for datatake 091.090-SRL-1.

Granule	CHH			CHV			LHH			LHV		
	CTV	RCTV	SSD	CTV	RCTV	SSD	CTV	RCTV	SSD	CTV	RCTV	SSD
1994/10/06/12:26:27-12:26:42	5.349	±1.066	0.346	-	-	-	7.199	±0.485	0.082	6.905	±0.378	0.06
1994/10/06/12:26:41-12:26:56	5.678	±1.008	0.253	-	-	-	7.04	±0.686	0.182	6.794	±0.413	0.06
1994/10/06/12:26:55-12:27:10	4.683	±2.156	0.816	-	-	-	7.172	±1.803	0.265	6.355	±2.108	0.343
1994/10/06/12:27:10-12:27:25	8.453	±0.527	0.113	7.27	±0.595	0.172	8.436	±0.979	0.315	6.872	±1.084	0.41
1994/10/06/12:27:24-12:27:39	10	±0.55	0.101	9.362	±0.431	0.087	9.44	±0.558	0.134	7.908	±0.726	0.182
1994/10/06/12:27:38-12:27:53	7.354	±0.505	0.156	6.622	±0.524	0.123	7.033	±0.533	0.172	6.069	±0.499	0.15
1994/10/06/12:27:53-12:28:08	7.323	±1.053	0.274	6.494	±1.256	0.35	7.233	±2.021	1.02	7.903	±2.068	1.424
1994/10/06/12:28:07-12:28:22	5.732	±0.604	0.127	4.629	±1.204	0.578	6.939	±1.862	1.207	8.447	±2.741	2.615
1994/10/06/12:28:21-12:28:36	7.66	±0.665	0.233	7.215	±1.143	0.366	10.785	±2.069	1.582	10.585	±2.6	2.346
1994/10/06/12:28:36-12:28:51	8.002	±1.025	0.365	7.373	±1.041	0.395	12.209	±2.984	4.135	14.329	±5.596	6.37

1994/10/06/12:28:50-12:29:05	7.553	±0.8	0.232	7.804	±0.965	0.356	11.556	±2.238	1.742	11.194	±1.863	1.152
1994/10/06/12:28:55-12:29:10	7.432	±1.056	0.39	6.999	±1.102	0.38	9.541	±2.451	1.954	9.363	±2.76	2.464
Average:	7.102	±0.918	0.284	7.085	±0.918	0.312	8.715	±1.556	1.066	8.56	±1.903	1.465

Table A.10: Test results for datatake 099.000-SRL-2.

Granule	CHH			CHV			LHH			LHV		
	CTV	RCTV	SSD	CTV	RCTV	SSD	CTV	RCTV	SSD	CTV	RCTV	SSD
1994/04/15/18:45:12-18:45:24	9.012	±0.091	0.007	8.743	±0.273	0.008	9.243	±0.144	0.011	8.343	±0.192	0.016
1994/04/15/18:45:23-18:45:35	9.03	±0.09	0.007	8.79	±0.277	0.012	9.272	±0.112	0.008	8.287	±0.108	0.008
1994/04/15/18:45:35-18:45:47	9.162	±0.15	0.007	8.966	±0.281	0.008	9.549	±0.256	0.029	8.539	±0.269	0.032
1994/04/15/18:45:46-18:45:58	9.47	±0.206	0.02	9.119	±0.118	0.009	9.792	±0.426	0.051	8.838	±0.469	0.09
1994/04/15/18:45:58-18:46:10	9.251	±0.2	0.014	8.848	±0.353	0.023	9.349	±0.344	0.045	7.827	±0.517	0.11
1994/04/15/18:46:09-18:46:21	9.492	±0.116	0.006	9.269	±0.258	0.011	9.818	±0.303	0.033	8.883	±0.291	0.032
1994/04/15/18:46:21-18:46:33	9.877	±0.12	0.008	9.528	±0.268	0.012	10.283	±0.342	0.045	9.211	±0.158	0.009
1994/04/15/18:46:32-18:46:44	8.907	±0.247	0.026	8.571	±0.709	0.102	9.294	±0.677	0.147	8.244	±0.534	0.093
1994/04/15/18:46:44-18:46:56	8.741	±0.277	0.033	8.019	±0.565	0.044	8.529	±0.373	0.057	9.248	±0.594	0.114
1994/04/15/18:46:55-18:47:07	9.594	±0.971	0.315	9.271	±0.261	0.027	9.775	±1.423	0.791	8.431	±1.032	0.397
1994/04/15/18:47:07-18:47:19	9.654	±0.271	0.029	8.747	±0.533	0.039	8.942	±0.604	0.139	7	±0.634	0.161
1994/04/15/18:47:18-18:47:30	9.803	±0.278	0.035	9.572	±0.349	0.063	10.228	±0.748	0.209	9.803	±0.962	0.322
1994/04/15/18:47:30-18:47:42	9.44	±0.415	0.053	9.488	±0.533	0.105	10.767	±0.56	0.182	10.438	±1	0.344
1994/04/15/18:47:41-18:47:53	9.432	±0.432	0.057	8.925	±0.638	0.064	10.963	±0.49	0.074	10.309	±0.58	0.126
1994/04/15/18:47:53-18:48:05	10.02	±0.546	0.115	9.942	±0.442	0.036	11.085	±0.7	0.202	11.576	±1.278	0.597
1994/04/15/18:48:04-18:48:16	9.846	±0.231	0.027	9.573	±0.422	0.034	11.864	±0.793	0.227	11.635	±0.971	0.347
1994/04/15/18:48:16-18:48:28	9.077	±0.77	0.092	8.582	±0.815	0.103	10.3	±0.942	0.323	8.774	±1.438	0.537
1994/04/15/18:48:27-18:48:39	9.551	±0.236	0.01	9.434	±0.258	0.014	10.357	±0.628	0.127	9.315	±0.867	0.2
1994/04/15/18:48:39-18:48:51	9.976	±0.146	0.009	9.899	±0.145	0.009	10.574	±0.264	0.018	9.397	±0.384	0.05
1994/04/15/18:48:50-18:49:02	10.075	±0.191	0.008	9.89	±0.249	0.007	11.263	±0.289	0.039	9.984	±0.255	0.025
1994/04/15/18:49:02-18:49:14	10.131	±0.166	0.014	9.839	±0.243	0.016	10.915	±0.22	0.016	9.694	±0.424	0.073

1994/04/15/18:49:13-18:49:26	10.436	±0.131	0.007	10.101	±0.306	0.032	11.312	±0.281	0.023	10.104	±0.259	0.023
1994/04/15/18:49:25-18:49:37	9.972	±0.136	0.009	9.825	±0.18	0.013	10.426	±0.196	0.015	9.584	±0.166	0.012
1994/04/15/18:49:36-18:49:49	9.858	±0.407	0.055	9.512	±0.709	0.18	9.985	±1.187	0.391	9.137	±1.502	0.669
1994/04/15/18:49:48-18:50:00	10.636	±0.225	0.019	10.259	±0.572	0.077	11.193	±1.122	0.398	10.632	±1.558	0.745
1994/04/15/18:50:00-18:50:12	10.907	±0.2	0.014	10.983	±0.277	0.032	10.731	±0.534	0.075	10.887	±0.735	0.203
1994/04/15/18:50:11-18:50:23	12.674	±0.472	0.094	11.287	±0.498	0.058	13.976	±0.589	0.157	11.627	±0.894	0.264
1994/04/15/18:50:23-18:50:35	12.891	±0.368	0.044	11.763	±0.74	0.135	13.359	±0.644	0.195	11.506	±0.759	0.142
1994/04/15/18:50:34-18:50:46	13.054	±0.354	0.039	11.53	±0.94	0.141	13.457	±1.187	0.171	10.556	±1.07	0.172
1994/04/15/18:50:46-18:50:58	13.386	±0.38	0.051	11.364	±1.139	0.282	15.17	±0.768	0.184	12.511	±0.777	0.177
1994/04/15/18:50:57-18:51:09	12.004	±0.93	0.214	10.904	±1.556	0.643	11.2	±1.664	0.706	9.96	±1.6	0.635
1994/04/15/18:51:07-18:51:19	12.848	±1.351	0.514	11.053	±1.46	0.325	12.082	±1.531	0.997	10.621	±2.21	0.409
Average:	10.257	±0.347	0.061	9.737	±0.511	0.083	10.783	±0.636	0.19	9.716	±0.765	0.223

Table A.11: Test results for datatake 103.060-SRL-1.

Granule	CHH		
	CTV	RCTV	SSD
1994/04/18/15:52:03-15:52:18	10.077	±0.936	0.296
1994/04/18/15:52:17-15:52:32	10.105	±1.216	0.458
1994/04/18/15:52:31-15:52:46	9.801	±0.895	0.243
1994/04/18/15:52:46-15:53:01	8.119	±1.079	0.242
1994/04/18/15:53:00-15:53:15	8.474	±1.721	0.892
1994/04/18/15:53:14-15:53:29	10.014	±1.383	0.693
1994/04/18/15:53:29-15:53:44	9.291	±1.339	0.394
1994/04/18/15:53:43-15:53:58	13.52	±1.048	0.392
1994/04/18/15:53:57-15:54:12	6.861	±3.142	1.454
1994/04/18/15:54:12-15:54:27	11.723	±1.17	0.526
1994/04/18/15:54:26-15:54:41	9.838	±0.991	0.253
1994/04/18/15:54:40-15:54:55	9.946	±1.393	0.708

1994/04/18/15:54:55-15:55:10	10.365	±1.206	0.39
1994/04/18/15:55:09-15:55:24	10.336	±1.343	0.639
1994/04/18/15:55:23-15:55:38	9.053	±0.982	0.299
1994/04/18/15:55:38-15:55:53	9.424	±0.908	0.214
1994/04/18/15:55:52-15:56:07	11.376	±1.375	0.542
1994/04/18/15:56:35-15:56:50	7.321	±1.642	0.797
1994/04/18/15:56:49-15:57:04	11.612	±2.293	1.115
Average:	9.855	±1.372	0.555

Table A.12: Test results for datatake 150.020-SRL-1.

B Probe Test Data

The following tables contain the phase-shifter test data for C and L-band, H and V-polarization. The first to columns each indicate the position of the phase-shifter within the array in elevation and azimuth. The next four columns contain the measurements for the $22.5°$, $45°$, $90°$ and $90°$ bit respectively.

		chps						cvps			
0	0	18,60	43,70	83,90	183,40	0	0	19,70	45,00	94,10	196,30
0	1	20,40	45,50	84,40	182,80	0	1	20,80	53,60	96,00	196,50
0	2	19,90	44,20	86,20	188,70	0	2	20,60	50,70	93,40	194,40
0	3	18,80	40,70	87,50	181,50	0	3	20,40	50,20	94,40	191,50
0	4	16,80	38,10	81,80	184,00	0	4	19,50	49,30	93,90	191,90
0	5	20,00	42,90	89,80	179,10	0	5	19,50	50,60	96,10	194,70
0	6	20,30	42,70	86,50	185,50	0	6	20,10	52,60	98,60	198,50
0	7	20,20	41,50	83,40	182,80	0	7	19,40	50,50	93,20	198,20
0	8	20,00	43,20	85,10	186,10	0	8	19,20	50,60	92,50	192,30
0	9	20,60	41,90	82,70	186,50	0	9	20,80	49,30	93,00	184,80
0	10	19,70	39,80	82,20	180,10	0	10	20,10	49,60	95,30	184,00
0	11	19,50	43,20	81,90	176,20	0	11	21,50	52,20	95,50	182,70
0	12	19,80	40,50	78,90	193,60	0	12	20,20	50,30	97,10	178,90
0	13	18,10	47,00	88,60	187,20	0	13	19,30	50,60	91,60	176,50
0	14	20,10	45,70	86,20	191,30	0	14	20,10	52,30	94,20	176,30
0	15	20,00	44,80	79,10	195,00	0	15	20,50	52,90	91,90	179,40
0	16	19,90	42,40	81,70	188,10	0	16	21,50	51,20	92,80	179,60
0	17	18,60	41,80	80,20	191,80	0	17	20,40	48,90	92,10	187,90
1	0	19,80	42,20	84,40	172,00	1	0	19,70	40,30	87,40	172,60
1	1	21,20	43,30	86,50	179,30	1	1	21,10	42,00	85,30	170,30
1	2	20,30	40,80	84,10	175,40	1	2	19,70	42,20	87,50	167,10
1	3	21,80	42,20	87,60	179,90	1	3	19,90	42,80	84,30	170,60
1	4	20,60	43,40	83,60	169,50	1	4	19,60	43,40	86,30	180,80
1	5	21,70	43,20	83,30	179,10	1	5	20,00	44,50	86,80	185,40
1	6	21,40	44,40	83,20	181,40	1	6	20,60	44,40	89,90	182,80
1	7	21,90	43,80	89,60	182,40	1	7	20,70	44,30	85,90	174,20
1	8	19,20	42,40	85,70	179,60	1	8	20,40	43,60	87,30	175,80
1	9	20,10	42,10	84,30	174,30	1	9	19,90	42,00	82,10	179,50
1	10	20,40	45,00	83,00	182,00	1	10	20,10	40,90	84,10	178,50
1	11	21,30	44,50	81,10	184,40	1	11	21,50	44,00	84,40	182,70
1	12	20,40	43,80	87,80	168,30	1	12	20,80	42,40	86,40	181,70
1	13	20,10	43,50	85,10	176,50	1	13	21,00	44,10	84,10	175,60
1	14	19,00	43,90	80,20	175,10	1	14	20,40	45,30	84,60	171,40
1	15	19,00	40,40	82,80	176,50	1	15	19,90	42,90	79,90	173,10
1	16	18,70	37,60	78,80	175,30	1	16	20,00	44,60	83,00	174,90
1	17	18,00	38,60	84,30	177,90	1	17	18,80	43,70	83,30	171,40
2	0	18,70	40,70	83,50	174,90	2	0	20,40	40,90	85,10	169,40
2	1	18,10	39,40	81,50	173,40	2	1	20,40	39,80	81,30	173,90
2	2	18,90	40,40	84,30	178,60	2	2	19,50	39,40	78,20	177,60
2	3	17,50	37,90	84,10	178,10	2	3	19,40	40,20	81,30	171,20
2	4	18,50	39,50	81,10	172,70	2	4	18,40	40,60	84,30	174,50
2	5	19,00	40,50	79,30	170,90	2	5	20,10	40,90	84,20	165,90
2	6	19,00	41,70	84,10	181,40	2	6	20,60	41,20	81,80	176,40
2	7	19,00	42,10	82,30	192,40	2	7	20,30	40,80	81,80	180,20
2	8	18,50	41,10	87,10	180,60	2	8	19,90	41,00	85,80	174,10
2	9	19,50	39,60	79,40	179,40	2	9	19,50	38,00	77,70	189,80
2	10	19,20	41,50	78,60	187,00	2	10	19,60	39,90	79,10	186,40
2	11	19,70	43,20	83,10	181,30	2	11	20,00	39,10	76,80	190,10
2	12	19,20	40,70	80,30	178,80	2	12	18,60	37,80	76,20	194,10
2	13	17,70	38,80	80,60	179,60	2	13	19,20	37,80	76,20	180,30
2	14	14,10	37,40	83,50	177,30	2	14	19,70	38,40	78,30	176,60
2	15	18,50	40,40	83,00	175,30	2	15	20,00	41,60	78,70	175,70
2	16	18,70	39,10	79,90	179,50	2	16	20,10	40,80	77,70	184,80
2	17	19,30	40,50	85,10	176,40	2	17	18,80	38,00	77,50	194,10
3	0	20,60	44,70	88,90	187,40	3	0	21,90	44,50	87,90	193,60
3	1	21,20	44,80	90,00	190,50	3	1	22,20	45,20	85,60	190,40
3	2	20,80	44,40	91,20	190,20	3	2	21,50	45,00	92,00	189,40
3	3	19,60	45,10	91,40	188,20	3	3	20,50	45,40	92,80	188,30
3	4	21,70	46,50	90,30	186,70	3	4	20,50	46,00	92,00	188,10
3	5	21,60	45,00	91,50	191,80	3	5	20,80	45,60	91,60	186,40
3	6	22,60	45,70	91,70	187,60	3	6	20,40	45,00	88,70	186,70
3	7	20,70	44,70	92,40	187,70	3	7	20,10	42,40	87,80	191,90
3	8	20,80	46,20	93,70	192,70	3	8	20,20	44,10	91,10	188,50
3	9	21,10	48,60	89,40	179,10	3	9	20,60	44,00	85,70	193,90
3	10	21,10	45,50	90,00	184,70	3	10	20,90	45,60	88,30	195,40

3	11	22,20	45,40	91,30	186,90	3	11	19,90	42,80	86,40	192,90
3	12	20,60	43,80	89,60	185,60	3	12	20,00	43,60	88,70	184,40
3	13	21,80	45,30	89,40	183,10	3	13	19,60	44,90	86,60	187,80
3	14	18,90	44,80	91,30	183,60	3	14	19,80	45,10	85,30	186,60
3	15	22,10	49,80	89,40	185,80	3	15	20,30	44,20	83,50	186,70
3	16	22,70	46,60	85,90	184,60	3	16	20,00	44,40	86,30	188,40
3	17	21,30	47,10	89,50	187,10	3	17	20,30	43,40	88,60	188,80
4	0	19,20	41,90	85,20	188,70	4	0	21,00	44,50	92,90	184,20
4	1	19,90	42,70	84,50	184,00	4	1	21,70	42,50	86,70	182,10
4	2	19,30	42,50	85,60	184,30	4	2	20,70	42,20	87,30	186,80
4	3	19,50	42,20	90,50	185,10	4	3	20,60	43,10	86,20	183,90
4	4	20,10	44,80	88,70	182,90	4	4	19,70	45,90	92,30	181,30
4	5	20,00	43,80	83,10	174,20	4	5	21,10	45,90	90,50	179,80
4	6	20,50	45,40	92,90	193,50	4	6	20,20	45,90	88,90	181,70
4	7	20,70	44,40	90,60	193,60	4	7	20,10	45,10	89,60	188,60
4	8	23,20	47,20	93,40	197,10	4	8	19,80	44,40	90,60	191,70
4	9	20,90	44,50	85,60	200,50	4	9	20,60	44,20	86,50	193,00
4	10	20,70	43,80	90,40	185,40	4	10	20,30	44,50	84,10	196,10
4	11	20,10	44,00	83,60	184,40	4	11	20,30	46,20	85,80	187,10
4	12	21,30	42,70	90,50	185,10	4	12	20,60	44,60	90,90	183,90
4	13	18,60	40,00	86,80	185,70	4	13	20,60	43,20	85,10	192,90
4	14	19,10	42,60	83,60	185,20	4	14	20,10	45,00	86,20	194,40
4	15	20,30	45,40	89,20	184,50	4	15	21,50	44,90	84,30	190,10
4	16	19,40	41,10	85,70	195,60	4	16	21,30	45,10	84,80	191,70
4	17	19,60	41,00	85,60	187,30	4	17	21,40	43,30	88,00	195,40
5	0	19,70	42,20	87,40	170,40	5	0	21,10	42,40	77,80	158,50
5	1	20,30	43,40	85,10	173,30	5	1	20,00	42,00	81,20	175,50
5	2	18,70	42,50	82,80	174,60	5	2	19,90	40,40	83,00	175,50
5	3	18,10	42,50	83,20	164,20	5	3	20,50	42,20	81,20	170,80
5	4	19,50	43,40	87,30	168,20	5	4	21,00	42,00	81,60	172,80
5	5	23,10	40,50	84,00	165,30	5	5	20,10	39,70	83,50	170,40
5	6	19,30	43,30	80,00	174,80	5	6	18,90	42,10	84,00	178,60
5	7	19,50	42,30	88,50	180,40	5	7	20,20	43,30	82,80	172,30
5	8	19,80	42,30	87,50	172,80	5	8	21,30	44,90	82,70	174,00
5	9	21,10	45,50	87,50	174,70	5	9	20,40	42,40	83,60	179,90
5	10	19,50	41,60	85,30	178,60	5	10	19,80	42,00	85,80	174,80
5	11	19,30	43,90	80,10	171,40	5	11	20,40	44,40	82,60	173,40
5	12	21,30	46,70	80,20	180,10	5	12	20,30	42,10	85,10	182,50
5	13	18,40	41,10	80,70	176,90	5	13	20,30	42,50	83,20	176,60
5	14	19,30	42,20	82,90	177,50	5	14	19,40	41,30	83,10	173,80
5	15	19,40	46,30	86,20	175,70	5	15	20,10	43,80	81,30	173,70
5	16	19,20	45,00	82,90	172,00	5	16	20,20	43,70	80,30	176,10
5	17	20,40	44,80	87,70	175,30	5	17	20,20	41,70	82,00	179,10
6	0	19,60	41,30	80,90	174,30	6	0	19,70	41,50	87,70	176,10
6	1	19,90	43,80	85,20	174,10	6	1	21,50	45,40	88,10	175,00
6	2	19,20	43,20	84,00	174,00	6	2	20,90	44,00	84,60	174,30
6	3	20,70	43,40	85,30	172,10	6	3	21,10	46,90	85,30	173,10
6	4	19,20	43,10	83,00	180,50	6	4	20,10	44,60	84,50	171,80
6	5	18,80	41,50	85,90	171,90	6	5	19,30	44,50	86,40	172,30
6	6	21,30	47,30	90,50	176,00	6	6	20,60	43,70	86,90	188,40
6	7	20,10	41,50	84,60	175,80	6	7	21,10	44,70	90,10	192,20
6	8	18,80	41,20	82,20	180,90	6	8	19,90	41,80	88,10	189,30
6	9	20,30	42,70	87,30	174,60	6	9	20,20	41,40	79,30	186,00
6	10	20,10	44,40	83,30	180,60	6	10	20,70	42,00	81,40	182,50
6	11	20,40	41,50	84,20	178,50	6	11	20,40	42,80	87,30	176,00
6	12	20,00	43,20	84,20	173,00	6	12	20,10	42,10	88,80	174,00
6	13	19,70	44,60	87,50	174,60	6	13	19,20	42,40	82,50	176,70
6	14	18,80	41,00	82,30	180,60	6	14	19,50	42,30	86,20	174,10
6	15	18,50	41,10	83,60	179,60	6	15	19,10	42,10	82,70	176,00
6	16	19,40	40,80	84,20	176,30	6	16	19,60	42,20	79,40	180,20
6	17	17,60	39,80	82,60	172,70	6	17	18,40	41,20	77,90	179,30
7	0	18,80	41,50	85,70	184,20	7	0	17,70	37,40	89,60	197,80
7	1	18,90	42,20	83,90	181,30	7	1	20,20	41,70	86,60	194,40
7	2	19,30	43,10	84,70	185,40	7	2	19,40	41,40	85,70	193,40
7	3	18,20	40,00	82,50	180,70	7	3	19,50	41,60	85,90	199,30
7	4	20,30	42,00	83,50	180,70	7	4	19,20	43,10	85,40	191,20
7	5	21,80	41,80	92,10	180,80	7	5	19,70	42,70	89,10	190,40

7	6	21,90	45,30	86,00	185,30	7	6	20,00	43,80	89,40	198,20
7	7	21,10	43,50	87,80	182,20	7	7	20,50	44,80	88,50	197,80
7	8	21,10	43,90	89,70	188,90	7	8	21,20	44,60	91,10	193,70
7	9	20,20	42,50	83,80	195,10	7	9	20,40	44,40	87,20	183,50
7	10	21,80	43,30	87,20	187,10	7	10	20,50	43,20	85,20	184,50
7	11	20,80	45,00	84,10	189,10	7	11	20,00	44,50	84,00	178,90
7	12	21,60	45,40	87,90	190,40	7	12	20,20	45,20	87,20	178,00
7	13	19,50	40,70	85,00	188,00	7	13	19,80	43,60	84,00	186,20
7	14	17,50	40,40	82,80	184,60	7	14	19,30	42,60	85,20	182,80
7	15	19,90	46,50	88,10	186,40	7	15	19,50	43,20	82,80	179,60
7	16	20,10	42,60	83,80	194,10	7	16	21,10	46,60	85,80	183,80
7	17	19,80	43,00	86,80	189,00	7	17	19,50	48,60	88,70	182,40
8	0	20,20	42,10	86,70	182,30	8	0	20,40	39,40	91,40	186,30
8	1	20,00	42,00	86,40	188,90	8	1	20,10	41,20	85,30	184,30
8	2	19,60	41,20	84,80	192,80	8	2	19,50	42,70	87,00	189,80
8	3	18,90	43,30	87,80	188,30	8	3	19,90	44,00	86,40	188,00
8	4	17,40	37,50	82,60	179,50	8	4	20,60	43,70	89,90	186,20
8	5	20,00	43,80	87,00	190,10	8	5	19,80	42,60	90,40	191,90
8	6	20,80	46,40	94,50	193,50	8	6	19,30	42,00	88,40	186,50
8	7	20,50	42,70	88,30	185,40	8	7	19,80	42,60	86,40	193,80
8	8	21,80	45,70	94,70	196,10	8	8	21,10	43,80	91,10	187,60
8	9	21,30	45,90	88,40	192,00	8	9	19,80	42,50	86,10	177,40
8	10	21,40	44,70	88,50	198,40	8	10	19,30	42,20	80,80	183,30
8	11	19,80	43,50	87,20	173,70	8	11	18,70	41,90	81,40	174,30
8	12	20,90	44,80	90,00	174,40	8	12	19,90	42,00	87,40	174,90
8	13	20,30	46,70	89,90	184,40	8	13	20,60	45,10	87,00	187,40
8	14	19,90	44,10	84,70	185,40	8	14	20,30	44,30	83,60	185,30
8	15	17,60	40,70	84,60	187,20	8	15	20,60	45,20	85,00	184,70
8	16	18,20	40,20	85,00	188,70	8	16	20,50	44,00	86,70	187,90
8	17	17,90	40,30	81,30	186,70	8	17	20,70	43,90	92,20	187,50
9	0	16,60	39,40	85,60	176,40	9	0	20,90	43,40	89,10	172,40
9	1	19,20	40,80	82,90	177,60	9	1	21,20	43,00	85,50	172,10
9	2	17,90	42,10	84,20	170,70	9	2	20,20	42,50	88,10	173,60
9	3	17,70	39,40	82,10	180,40	9	3	19,50	41,00	84,30	172,30
9	4	16,90	37,90	79,80	162,10	9	4	19,70	43,60	83,20	177,50
9	5	20,40	41,30	84,50	166,60	9	5	20,10	41,90	86,40	176,30
9	6	18,70	38,90	83,40	177,00	9	6	21,20	43,60	91,10	182,10
9	7	19,80	41,80	83,20	176,80	9	7	20,90	43,70	87,90	183,60
9	8	20,40	40,40	81,00	171,00	9	8	21,30	43,90	86,90	176,40
9	9	18,40	40,50	80,50	177,30	9	9	19,90	42,40	83,20	181,60
9	10	18,90	40,50	79,20	179,40	9	10	20,40	43,40	86,20	182,50
9	11	20,50	43,40	86,50	181,60	9	11	20,60	43,10	85,80	182,00
9	12	19,90	41,00	85,80	174,90	9	12	20,00	41,90	90,00	174,60
9	13	17,40	39,00	82,00	164,10	9	13	18,60	41,60	87,30	175,40
9	14	17,40	39,60	83,30	174,40	9	14	19,20	40,00	81,00	172,40
9	15	19,40	43,10	83,60	169,00	9	15	19,60	42,50	86,80	174,70
9	16	19,80	40,00	82,20	171,00	9	16	20,10	43,80	82,40	173,20
9	17	19,10	41,80	82,30	171,30	9	17	19,00	41,70	83,60	175,90
10	0	19,50	44,20	86,80	190,10	10	0	20,60	40,00	89,00	187,90
10	1	19,40	43,70	87,70	188,10	10	1	21,40	43,60	86,00	187,80
10	2	19,50	45,20	89,50	188,70	10	2	21,10	41,90	87,60	193,30
10	3	19,40	41,50	92,10	184,30	10	3	21,70	45,20	91,20	186,10
10	4	19,70	44,00	93,00	186,00	10	4	22,10	47,20	92,90	191,20
10	5	19,30	41,80	91,50	188,00	10	5	20,20	43,20	90,60	196,80
10	6	20,70	45,20	89,00	197,00	10	6	19,00	40,80	85,40	181,20
10	7	20,80	44,20	89,90	191,30	10	7	20,80	43,90	84,40	186,70
10	8	20,20	43,70	87,90	189,50	10	8	21,00	45,10	87,00	185,80
10	9	19,20	45,80	88,60	184,50	10	9	21,50	46,60	86,20	189,50
10	10	19,70	43,90	84,80	190,30	10	10	20,60	44,60	85,50	196,40
10	11	20,10	43,50	87,20	195,70	10	11	22,00	45,60	86,50	197,00
10	12	19,20	44,70	87,90	183,50	10	12	20,30	40,30	88,40	181,50
10	13	21,60	48,00	89,00	190,20	10	13	19,80	43,20	86,20	191,20
10	14	19,80	43,90	91,40	188,20	10	14	20,80	44,30	87,20	194,70
10	15	19,50	44,70	89,30	189,20	10	15	20,70	44,00	85,10	193,50
10	16	20,50	44,10	86,90	193,20	10	16	20,90	43,40	84,50	192,30
10	17	19,70	42,80	86,60	194,30	10	17	18,50	43,10	91,00	193,40
11	0	19,60	40,70	87,30	190,80	11	0	18,20	42,70	94,40	189,20

11	1	19,80	42,50	88,90	185,80	11	1	20,00	44,40	88,80	182,20
11	2	20,80	42,50	90,20	190,50	11	2	20,20	42,60	88,70	182,80
11	3	18,90	41,30	89,90	182,60	11	3	20,30	43,00	85,60	187,70
11	4	20,10	43,70	89,50	184,90	11	4	19,60	42,90	84,20	182,80
11	5	21,70	45,60	90,60	181,00	11	5	19,90	44,30	90,30	185,30
11	6	22,00	44,70	89,20	190,90	11	6	19,90	44,30	92,00	185,60
11	7	20,60	43,70	85,40	188,20	11	7	19,70	44,00	87,20	184,90
11	8	20,90	45,80	88,80	188,30	11	8	20,00	45,60	88,50	188,40
11	9	19,60	40,20	82,60	181,90	11	9	19,70	41,50	84,30	177,90
11	10	20,20	43,20	84,40	180,70	11	10	19,30	41,40	80,10	182,10
11	11	20,20	43,20	84,30	185,50	11	11	20,20	42,00	79,50	181,00
11	12	20,40	41,00	86,60	174,80	11	12	20,10	43,80	88,80	177,90
11	13	17,70	39,90	88,80	193,20	11	13	21,30	46,10	90,40	185,10
11	14	20,20	46,50	91,70	186,80	11	14	19,10	42,70	84,50	190,10
11	15	18,10	39,60	82,60	176,90	11	15	20,60	45,20	85,90	189,80
11	16	16,80	35,30	81,40	173,50	11	16	20,20	41,70	81,90	175,20
11	17	18,00	37,80	79,50	174,50	11	17	20,80	41,50	85,00	177,50
12	0	20,00	45,00	92,40	190,20	12	0	20,40	39,40	91,40	186,30
12	1	20,00	44,70	93,90	189,90	12	1	20,10	41,20	85,30	184,30
12	2	19,40	44,90	91,30	194,00	12	2	19,50	42,70	87,00	189,80
12	3	20,90	43,60	92,90	188,10	12	3	19,90	44,00	86,40	188,00
12	4	19,60	43,90	92,10	194,50	12	4	20,60	43,70	89,90	186,20
12	5	20,80	47,20	91,20	196,60	12	5	19,80	42,60	90,40	191,90
12	6	22,60	44,80	90,20	189,70	12	6	19,30	42,00	88,40	186,50
12	7	20,20	44,60	85,50	195,80	12	7	19,80	42,60	86,40	193,80
12	8	21,40	47,40	86,80	197,30	12	8	21,10	43,80	91,10	187,60
12	9	20,40	47,60	86,10	184,80	12	9	19,80	42,50	86,10	177,40
12	10	21,30	44,50	87,40	196,60	12	10	19,30	42,20	80,80	183,30
12	11	19,80	43,30	88,70	189,00	12	11	18,70	41,90	81,40	174,30
12	12	21,40	48,30	93,80	179,00	12	12	19,90	42,00	87,40	174,90
12	13	20,00	41,80	90,40	183,50	12	13	20,60	45,10	87,00	187,40
12	14	19,40	42,80	91,10	187,00	12	14	20,30	44,30	83,60	185,30
12	15	19,70	41,60	89,20	183,40	12	15	20,60	45,20	85,00	184,70
12	16	20,40	42,60	90,10	185,30	12	16	20,50	44,00	86,70	187,90
12	17	20,00	43,50	88,20	182,90	12	17	20,70	43,90	92,20	187,50
13	0	18,70	41,00	81,80	184,30	13	0	18,30	42,10	88,50	192,20
13	1	19,50	42,60	85,70	183,10	13	1	19,60	44,40	84,60	178,10
13	2	20,10	41,50	84,00	187,00	13	2	18,90	43,70	85,10	185,50
13	3	19,20	42,80	86,70	189,80	13	3	19,60	43,20	86,30	188,30
13	4	19,10	43,10	89,60	181,40	13	4	18,50	44,30	89,70	182,10
13	5	21,30	44,40	90,90	192,90	13	5	19,00	44,70	90,40	186,10
13	6	20,90	44,50	88,70	181,50	13	6	19,00	44,80	89,00	190,80
13	7	19,20	43,40	86,00	186,30	13	7	19,70	46,60	88,70	190,00
13	8	20,00	42,90	87,80	190,60	13	8	19,70	44,70	88,60	197,30
13	9	19,80	46,80	88,90	186,80	13	9	19,20	44,60	86,40	189,90
13	10	19,00	41,30	86,30	195,00	13	10	18,60	43,80	86,70	187,70
13	11	19,40	44,80	88,20	189,20	13	11	19,30	42,80	82,90	199,80
13	12	26,70	39,90	79,80	186,00	13	12	20,20	44,90	91,00	182,90
13	13	19,80	46,10	90,90	193,20	13	13	20,50	45,00	86,00	191,10
13	14	19,10	46,60	89,00	191,20	13	14	20,10	44,90	83,50	189,40
13	15	17,80	40,80	87,50	191,60	13	15	20,20	44,30	82,70	193,00
13	16	17,90	38,70	85,20	186,30	13	16	20,20	43,70	82,30	193,20
13	17	19,10	39,00	86,30	190,60	13	17	20,30	42,50	87,10	192,00
14	0	18,80	42,80	82,60	174,60	14	0	16,90	39,90	91,10	175,60
14	1	19,70	42,80	84,10	177,90	14	1	20,70	36,60	75,70	174,80
14	2	18,60	41,00	82,40	177,20	14	2	18,50	37,00	77,60	175,60
14	3	20,20	44,40	87,90	174,30	14	3	20,50	44,10	84,70	180,80
14	4	19,30	43,70	83,30	179,60	14	4	19,80	43,70	87,00	178,90
14	5	20,30	43,30	86,20	185,60	14	5	19,70	42,30	90,60	182,30
14	6	19,10	40,40	83,20	181,70	14	6	19,30	41,10	85,70	180,00
14	7	18,60	41,10	83,70	173,30	14	7	21,00	41,80	84,10	175,30
14	8	19,80	42,40	88,50	187,40	14	8	20,80	44,50	87,70	176,00
14	9	19,30	45,30	84,20	188,80	14	9	20,10	44,40	83,80	184,70
14	10	20,00	41,90	83,40	194,10	14	10	18,90	42,20	85,70	179,50
14	11	20,70	43,40	87,50	179,70	14	11	19,20	42,70	84,80	180,70
14	12	19,80	44,90	85,70	174,10	14	12	20,10	42,60	85,80	178,10
14	13	17,80	39,40	81,20	171,50	14	13	19,10	41,70	80,80	179,30

14	14	18,80	41,70	83,40	170,20	14	14	18,50	40,50	80,90	174,70
14	15	19,10	45,20	86,60	174,10	14	15	17,90	39,10	77,40	174,90
14	16	18,80	38,90	81,20	173,90	14	16	17,60	37,70	75,70	177,60
14	17	17,30	40,40	81,30	179,60	14	17	19,10	37,40	78,70	174,40
15	0	18,70	41,40	82,70	187,40	15	0	23,10	39,80	93,80	177,20
15	1	18,50	41,90	84,30	169,60	15	1	21,60	42,10	85,30	172,50
15	2	18,10	39,60	81,60	173,70	15	2	20,10	42,10	86,10	174,80
15	3	18,30	38,90	86,80	171,60	15	3	18,90	42,70	86,90	173,20
15	4	18,30	39,70	85,40	181,10	15	4	20,00	44,00	85,90	176,70
15	5	19,80	42,60	86,70	174,60	15	5	20,50	43,80	86,60	176,50
15	6	18,10	42,00	85,90	172,30	15	6	20,10	44,50	87,10	177,70
15	7	19,80	43,10	86,80	171,00	15	7	20,60	44,20	86,60	173,00
15	8	19,40	41,50	88,00	169,40	15	8	20,30	45,50	89,10	176,50
15	9	19,90	42,60	83,30	177,50	15	9	20,30	42,10	82,30	172,00
15	10	19,00	40,00	83,10	183,10	15	10	20,20	43,30	84,70	173,60
15	11	19,50	41,00	79,30	175,00	15	11	21,00	43,50	86,00	183,40
15	12	19,90	43,40	91,80	183,20	15	12	20,90	43,30	88,80	178,20
15	13	18,40	41,10	82,30	175,30	15	13	21,30	45,60	86,80	172,50
15	14	17,90	41,40	86,40	173,30	15	14	19,90	45,10	87,00	169,50
15	15	19,50	42,10	85,80	173,30	15	15	19,50	45,50	82,70	173,80
15	16	19,40	41,80	81,60	177,20	15	16	19,90	44,60	84,20	179,40
15	17	19,90	44,20	85,70	171,50	15	17	21,10	43,60	86,20	182,80
16	0	18,40	43,10	86,10	186,90	16	0	21,80	38,20	94,60	194,30
16	1	19,60	41,60	83,50	189,10	16	1	22,40	46,40	87,90	193,40
16	2	19,10	44,00	86,50	184,40	16	2	20,70	44,40	83,20	195,30
16	3	19,90	43,20	88,60	185,20	16	3	20,70	44,00	86,60	190,60
16	4	19,70	43,80	84,90	184,60	16	4	19,20	43,90	87,30	180,70
16	5	20,50	44,70	86,60	199,60	16	5	22,00	46,40	100,70	192,20
16	6	19,40	40,90	86,60	184,10	16	6	22,40	48,00	94,50	180,40
16	7	19,20	41,80	83,20	186,30	16	7	20,20	45,60	86,30	181,40
16	8	19,20	42,50	81,30	185,10	16	8	21,90	47,00	88,30	197,30
16	9	19,20	43,50	79,10	200,20	16	9	18,80	41,20	87,30	186,00
16	10	20,20	40,20	82,80	200,30	16	10	19,10	41,20	86,20	194,40
16	11	19,10	40,90	86,90	190,70	16	11	19,30	41,40	83,70	195,60
16	12	19,30	47,90	88,80	181,80	16	12	19,50	39,70	89,80	184,50
16	13	17,60	40,80	83,80	189,20	16	13	20,30	43,80	91,50	189,50
16	14	18,80	41,70	83,70	182,90	16	14	21,10	45,70	90,70	185,50
16	15	17,90	42,80	84,80	192,40	16	15	20,10	46,50	82,60	184,70
16	16	18,30	41,10	85,20	191,70	16	16	23,60	50,40	88,20	188,00
16	17	17,10	39,40	83,20	193,50	16	17	16,20	27,50	78,20	193,80
17	0	17,90	39,40	82,90	185,40	17	0	20,40	43,70	93,00	194,70
17	1	19,50	40,70	82,80	187,30	17	1	21,40	44,60	86,30	188,40
17	2	19,50	41,10	84,70	182,80	17	2	20,90	44,30	88,80	184,90
17	3	19,50	42,60	84,20	184,30	17	3	22,50	49,20	91,00	185,70
17	4	18,60	45,20	85,80	178,00	17	4	22,30	45,80	87,70	190,90
17	5	20,60	46,00	86,10	185,40	17	5	19,90	42,80	85,80	181,20
17	6	21,70	46,70	90,90	193,60	17	6	20,20	43,40	85,60	185,10
17	7	20,50	44,70	88,50	191,20	17	7	19,60	44,10	91,40	194,70
17	8	20,10	44,70	90,60	187,70	17	8	19,90	46,00	94,00	191,00
17	9	20,00	44,40	86,50	189,10	17	9	19,30	42,80	85,90	186,80
17	10	19,30	42,70	87,30	197,00	17	10	19,20	42,40	83,50	190,20
17	11	21,50	46,10	86,00	184,50	17	11	20,00	45,30	84,50	191,90
17	12	20,70	44,00	91,70	185,60	17	12	21,00	44,20	88,60	184,80
17	13	19,20	44,40	90,00	182,20	17	13	19,80	43,70	83,30	181,20
17	14	20,60	43,10	86,70	189,40	17	14	20,30	43,90	85,80	185,50
17	15	17,80	39,50	84,70	188,30	17	15	19,60	43,60	87,50	187,50
17	16	20,30	40,50	85,90	186,10	17	16	19,80	44,70	87,00	188,80
17	17	19,10	40,00	86,50	191,30	17	17	21,00	43,30	85,30	185,00

		lhps						lvps			
0	0	23,00	43,50	87,90	174,70	0	0	23,70	44,60	90,60	175,80
0	1	23,10	43,50	86,20	176,10	0	1	22,40	43,20	86,40	178,00
0	2	22,80	42,50	88,20	175,90	0	2	23,30	44,00	91,40	177,90
0	3	23,00	43,70	90,50	177,90	0	3	22,60	42,60	87,40	179,40
0	4	22,40	42,00	90,40	181,90	0	4	22,50	42,70	89,80	176,20
0	5	21,80	42,00	91,40	178,10	0	5	22,10	43,40	91,70	179,20
0	6	21,90	41,10	86,40	179,60	0	6	22,30	43,10	89,20	178,80
0	7	21,90	41,00	91,10	179,60	0	7	23,80	42,10	90,00	179,40
0	8	22,20	41,90	93,10	182,00	0	8	22,30	43,50	87,60	176,70
0	9	22,90	41,90	89,50	179,00	0	9	21,90	41,10	92,10	179,80
0	10	22,50	41,70	89,60	181,20	0	10	22,30	41,00	90,30	181,70
0	11	22,60	42,00	89,00	180,60	0	11	22,30	41,10	88,70	179,00
0	12	22,00	41,10	90,40	181,70	0	12	22,00	39,90	89,80	180,00
0	13	22,80	43,30	90,90	181,30	0	13	23,10	40,50	89,80	181,60
0	14	23,30	43,80	91,90	180,50	0	14	24,40	43,70	92,30	185,40
0	15	22,30	38,60	89,10	176,60	0	15	23,40	42,90	89,10	179,00
0	16	23,10	42,70	90,30	177,10	0	16	23,20	43,00	90,10	178,00
0	17	22,90	42,70	89,00	174,30	0	17	23,90	44,00	89,90	177,40
1	0	24,20	44,80	89,20	180,30	1	0	22,50	43,50	89,40	177,10
1	1	24,40	45,50	89,50	178,60	1	1	23,80	43,20	88,50	180,00
1	2	23,50	43,20	88,50	180,10	1	2	23,70	44,30	91,80	183,30
1	3	23,30	43,70	92,30	184,40	1	3	23,90	43,30	92,00	179,40
1	4	23,50	43,70	91,40	180,80	1	4	22,90	44,70	91,80	182,30
1	5	22,60	41,60	91,60	181,80	1	5	22,40	41,90	89,50	178,80
1	6	23,30	42,20	90,50	180,10	1	6	22,00	42,60	90,80	178,60
1	7	23,30	42,50	91,70	179,40	1	7	23,30	41,50	90,40	180,10
1	8	23,20	42,80	94,40	180,70	1	8	22,60	41,50	92,00	181,80
1	9	22,70	42,60	93,30	183,20	1	9	22,90	43,20	92,40	184,00
1	10	23,40	43,00	90,80	182,80	1	10	24,80	43,00	87,80	178,30
1	11	22,60	41,50	89,70	182,60	1	11	22,20	41,70	89,50	182,10
1	12	21,90	41,90	92,30	179,60	1	12	23,00	41,90	93,80	181,30
1	13	23,80	44,10	96,20	182,90	1	13	24,00	44,20	96,40	178,60
1	14	23,10	45,70	95,00	183,90	1	14	24,40	45,00	90,40	181,50
1	15	23,40	42,10	91,00	182,50	1	15	24,90	44,70	92,40	182,40
1	16	24,40	44,80	92,00	180,50	1	16	23,40	43,10	91,60	177,90
1	17	23,20	44,00	89,80	180,40	1	17	23,10	43,30	89,90	180,10
2	0	21,50	43,10	86,70	175,00	2	0	21,50	41,80	86,80	175,50
2	1	22,60	42,90	88,80	175,00	2	1	22,20	42,30	88,90	175,40
2	2	23,60	43,40	89,70	175,30	2	2	22,60	41,50	92,50	177,50
2	3	21,40	43,00	89,60	181,00	2	3	22,00	43,40	92,00	178,50
2	4	23,20	41,20	92,30	182,30	2	4	22,40	42,00	87,20	175,70
2	5	22,50	41,90	87,30	174,20	2	5	21,80	41,10	90,40	180,50
2	6	22,70	41,80	88,40	176,00	2	6	23,10	41,40	92,00	178,90
2	7	21,10	41,20	86,30	177,70	2	7	22,60	40,70	85,80	180,20
2	8	21,70	41,50	89,20	179,10	2	8	21,60	40,10	90,70	179,40
2	9	23,10	41,90	91,10	178,30	2	9	22,90	41,50	91,40	181,00
2	10	23,50	43,00	92,70	181,10	2	10	23,00	42,30	91,60	181,90
2	11	23,50	43,60	92,10	181,30	2	11	23,00	42,30	91,80	181,50
2	12	23,20	41,30	93,00	181,20	2	12	22,90	42,30	94,30	182,70
2	13	23,60	43,50	91,70	182,50	2	13	23,40	42,90	89,00	175,30
2	14	23,90	46,30	92,60	179,50	2	14	22,70	44,90	86,80	176,80
2	15	23,20	43,10	87,10	180,40	2	15	23,50	45,20	93,30	179,00
2	16	23,00	44,30	89,50	178,20	2	16	23,20	43,80	87,90	175,20
2	17	23,10	44,00	89,70	175,80	2	17	23,10	44,60	90,70	175,80
3	0	24,10	44,30	85,40	175,90	3	0	22,70	39,50	87,90	174,10
3	1	23,00	44,30	88,60	178,60	3	1	23,00	26,40	84,30	161,90
3	2	24,90	43,50	84,50	181,40	3	2	22,00	43,30	84,40	178,80
3	3	25,10	45,50	89,70	174,80	3	3	23,00	47,00	96,30	177,50
3	4	23,60	45,20	90,80	180,80	3	4	23,50	43,60	87,80	177,80
3	5	22,60	42,00	89,60	179,70	3	5	21,90	41,40	90,30	178,70
3	6	22,30	42,20	89,60	177,90	3	6	21,00	41,50	90,10	177,40
3	7	21,70	41,00	89,00	179,60	3	7	23,50	42,00	87,60	177,40
3	8	22,20	41,90	90,40	179,30	3	8	21,50	41,70	92,30	180,00
3	9	22,90	43,20	88,40	178,50	3	9	22,90	40,90	90,10	177,70
3	10	22,90	42,40	88,20	177,20	3	10	22,60	42,00	87,20	179,60

3	11	22,80	41,40	87,70	178,10	3	11	23,40	42,80	88,40	180,50
3	12	22,60	42,10	91,00	178,30	3	12	22,90	42,00	90,70	177,60
3	13	22,80	42,60	94,30	178,90	3	13	22,80	42,70	84,10	181,60
3	14	23,60	46,00	91,10	179,10	3	14	22,70	42,80	88,30	175,50
3	15	22,70	43,20	91,70	177,80	3	15	21,70	43,00	88,00	178,40
3	16	22,70	44,20	89,60	175,90	3	16	22,40	42,40	88,00	180,50
3	17	22,40	43,40	88,80	172,60	3	17	22,50	42,50	86,90	176,30
4	0	23,00	42,70	87,40	178,00	4	0	21,90	42,70	87,50	178,70
4	1	23,10	44,00	90,00	178,30	4	1	22,70	43,00	87,50	179,60
4	2	22,30	39,60	85,10	174,40	4	2	22,80	43,10	88,20	177,50
4	3	22,20	43,10	90,80	180,60	4	3	23,90	47,70	96,10	167,50
4	4	22,30	44,10	91,90	179,80	4	4	21,10	41,10	87,70	178,60
4	5	21,30	41,10	85,10	175,60	4	5	22,20	41,20	89,40	178,90
4	6	21,20	40,90	89,00	178,90	4	6	22,30	40,80	88,20	176,20
4	7	22,10	41,60	87,30	179,40	4	7	22,50	41,50	91,00	177,30
4	8	21,80	41,00	88,90	179,50	4	8	23,10	41,60	89,70	178,40
4	9	22,70	42,20	88,70	178,10	4	9	22,10	41,50	90,00	180,20
4	10	23,90	44,90	90,80	181,00	4	10	22,60	42,00	87,90	175,30
4	11	23,70	41,60	87,30	177,60	4	11	22,40	41,70	86,00	178,20
4	12	23,70	43,30	90,50	178,60	4	12	22,50	39,80	89,20	175,70
4	13	23,40	43,70	89,40	180,30	4	13	23,00	44,60	93,30	177,80
4	14	24,10	43,90	93,00	180,30	4	14	22,10	43,00	90,80	180,30
4	15	22,70	43,30	90,20	181,70	4	15	23,00	42,40	93,00	180,20
4	16	22,80	43,50	89,10	178,20	4	16	22,80	43,50	89,40	179,10
4	17	24,40	43,70	88,70	178,30	4	17	22,40	42,50	86,20	175,70
5	0	23,40	44,20	89,00	178,20	5	0	23,40	43,80	91,10	177,10
5	1	23,80	44,20	90,80	176,80	5	1	22,50	44,30	91,60	179,30
5	2	24,70	44,80	89,20	180,70	5	2	23,60	43,70	90,60	177,40
5	3	23,00	42,40	90,10	177,00	5	3	22,00	42,50	90,80	176,70
5	4	21,90	42,00	89,70	178,00	5	4	23,00	43,10	95,30	179,90
5	5	23,60	40,90	86,50	177,20	5	5	22,50	41,20	90,30	179,40
5	6	22,00	42,30	89,80	179,60	5	6	21,20	42,60	88,90	177,90
5	7	21,70	40,60	89,00	179,00	5	7	22,40	40,30	89,70	181,40
5	8	22,30	40,80	90,70	177,40	5	8	22,00	42,80	91,70	177,40
5	9	23,10	42,10	88,50	179,00	5	9	22,90	42,30	92,50	179,00
5	10	23,30	42,50	89,30	177,80	5	10	22,90	42,10	89,80	178,90
5	11	23,10	40,70	88,20	178,70	5	11	22,90	42,10	91,70	182,00
5	12	22,90	42,40	90,40	179,80	5	12	22,40	41,80	91,30	182,30
5	13	22,20	43,00	91,20	180,20	5	13	22,50	41,90	89,90	179,50
5	14	23,80	43,80	89,60	179,70	5	14	22,90	45,00	94,30	176,60
5	15	24,30	43,50	91,10	180,70	5	15	23,30	43,50	90,80	183,30
5	16	23,80	44,00	90,00	181,90	5	16	23,30	43,20	90,70	177,80
5	17	23,50	44,00	88,50	179,70	5	17	23,10	44,30	89,60	177,50
6	0	23,30	43,60	90,80	179,30	6	0	23,40	42,60	89,00	174,90
6	1	23,60	44,70	91,70	179,10	6	1	23,20	42,10	90,60	178,70
6	2	23,80	43,50	88,40	178,90	6	2	22,00	42,20	88,20	178,70
6	3	23,70	42,30	90,70	181,00	6	3	22,70	43,80	88,80	176,20
6	4	23,50	43,30	90,90	178,60	6	4	22,70	40,40	91,00	183,80
6	5	23,10	42,10	91,10	181,40	6	5	23,90	43,00	91,40	179,10
6	6	23,40	41,80	90,30	183,60	6	6	22,40	42,30	89,60	178,40
6	7	23,30	41,30	91,20	182,70	6	7	22,40	41,30	90,60	175,00
6	8	23,20	42,00	91,40	180,70	6	8	22,80	42,20	91,30	182,70
6	9	23,20	42,20	89,30	177,40	6	9	22,40	41,10	85,10	178,20
6	10	23,10	41,80	87,40	176,70	6	10	21,80	41,50	91,00	177,40
6	11	22,70	42,10	88,10	177,60	6	11	21,80	40,90	86,50	176,60
6	12	23,40	41,70	90,00	175,50	6	12	21,30	41,60	90,60	182,70
6	13	22,90	43,40	88,10	178,60	6	13	23,20	43,00	90,50	178,20
6	14	23,80	43,30	91,10	179,70	6	14	24,20	42,90	89,40	177,20
6	15	22,90	44,80	91,60	177,70	6	15	22,00	42,20	87,90	177,50
6	16	23,30	44,50	87,40	176,70	6	16	23,30	43,60	89,40	179,10
6	17	22,50	44,50	88,50	172,60	6	17	22,70	44,10	91,40	178,10
7	0	24,00	45,10	88,10	178,10	7	0	23,40	44,60	89,60	178,00
7	1	23,20	43,90	91,80	178,50	7	1	23,20	43,90	90,70	179,60
7	2	22,60	43,30	88,20	177,10	7	2	22,30	44,70	92,00	177,60
7	3	22,90	43,30	89,80	175,80	7	3	21,90	41,80	90,90	181,30
7	4	21,90	41,50	90,50	176,30	7	4	22,50	43,40	89,40	178,20
7	5	21,70	40,70	90,00	175,10	7	5	22,10	41,60	90,80	181,00

7	6	21,70	40,40	89,40	178,50	7	6	20,40	40,70	89,00	180,20
7	7	21,40	40,70	89,10	176,90	7	7	22,50	43,80	88,40	177,00
7	8	21,60	40,20	89,20	175,80	7	8	21,30	42,00	90,60	179,30
7	9	23,30	40,90	90,10	181,10	7	9	22,00	42,00	91,80	181,50
7	10	23,90	43,30	92,20	183,00	7	10	21,90	41,70	87,20	176,40
7	11	22,60	43,20	90,80	181,00	7	11	21,30	41,10	87,10	181,30
7	12	21,30	41,30	89,20	175,30	7	12	21,30	39,70	86,30	174,90
7	13	22,90	43,80	90,60	180,10	7	13	22,30	44,00	92,40	181,90
7	14	22,20	42,50	91,50	174,70	7	14	22,80	43,70	89,40	180,50
7	15	23,60	44,70	91,90	180,90	7	15	23,20	42,30	92,30	179,90
7	16	24,10	44,30	91,10	179,40	7	16	23,30	44,00	90,10	179,10
7	17	25,00	44,90	93,90	181,20	7	17	24,30	43,90	89,90	182,10
8	0	23,40	43,80	88,40	176,20	8	0	22,00	42,20	87,00	176,70
8	1	23,50	44,10	87,50	176,10	8	1	22,70	42,50	88,80	178,90
8	2	33,40	52,10	98,30	186,00	8	2	22,10	41,70	93,50	176,70
8	3	23,40	45,40	93,20	179,20	8	3	22,50	41,10	90,50	179,60
8	4	21,80	43,70	91,50	179,60	8	4	22,30	42,40	91,00	175,20
8	5	22,20	40,90	89,70	177,80	8	5	21,40	40,50	88,40	179,50
8	6	21,10	41,10	88,10	177,90	8	6	21,10	39,20	86,20	175,10
8	7	21,80	41,70	90,60	181,00	8	7	21,20	40,70	84,30	177,60
8	8	21,00	40,50	88,30	177,30	8	8	21,90	41,00	88,10	177,00
8	9	24,10	42,70	91,20	183,30	8	9	22,50	42,60	90,60	174,70
8	10	23,20	43,10	89,10	184,20	8	10	23,40	42,50	91,00	179,30
8	11	22,50	40,70	90,80	182,00	8	11	23,80	42,00	89,00	182,70
8	12	23,00	42,30	93,40	183,10	8	12	22,30	41,60	88,90	180,00
8	13	23,40	43,30	93,80	181,20	8	13	23,10	44,60	96,60	179,70
8	14	24,80	44,50	94,80	181,20	8	14	25,30	45,90	89,40	185,80
8	15	24,00	42,20	91,00	181,90	8	15	23,70	46,20	94,50	181,20
8	16	24,10	44,60	91,00	179,10	8	16	23,50	45,90	91,20	180,40
8	17	24,20	43,20	91,00	181,10	8	17	24,60	45,90	92,20	176,90

The following tables contain the feed current measurements for for C and L-band, H and V-polarization, transmit and receive mode. The first to columns each indicate the position of the radiating element within the array in elevation and azimuth. The next two columns contain the measured amplitude and phase respectively.

		chrsc				chtsc				cvrsc				cvtsc	
0	0	5,60	132,10	0	0	26,87	27,30	0	0	13,58	71,10	0	0	32,30	-26,70
0	1	8,37	-226,90	0	1	29,49	27,30	0	1	15,47	56,96	0	1	34,92	-31,74
0	2	12,18	139,87	0	2	33,18	39,17	0	2	18,85	54,56	0	2	38,88	-38,44
0	3	16,04	138,30	0	3	36,56	13,70	0	3	21,45	67,26	0	3	40,52	-24,04
0	4	11,55	133,75	0	4	33,31	29,65	0	4	20,29	80,53	0	4	39,51	-43,37
0	5	16,00	151,98	0	5	37,67	23,88	0	5	21,11	53,37	0	5	42,06	-48,73
0	6	18,03	163,81	0	6	38,73	49,51	0	6	21,29	76,26	0	6	41,35	-30,93
0	7	19,24	-194,88	0	7	38,85	57,92	0	7	19,24	79,68	0	7	39,17	-26,92
0	8	17,73	162,29	0	8	37,62	31,89	0	8	23,14	77,50	0	8	42,14	-32,70
0	9	16,55	129,04	0	9	37,94	40,94	0	9	22,68	62,85	0	9	41,01	-19,45
0	10	16,92	128,52	0	10	37,36	17,42	0	10	22,47	61,67	0	10	41,16	317,07
0	11	18,21	148,35	0	11	36,76	43,75	0	11	22,32	76,99	0	11	40,58	-25,71
0	12	18,09	143,92	0	12	38,95	24,12	0	12	19,89	72,70	0	12	40,40	-19,30
0	13	14,92	157,31	0	13	36,09	41,71	0	13	20,60	53,92	0	13	40,93	-31,88
0	14	17,07	162,85	0	14	36,91	50,25	0	14	19,36	61,72	0	14	39,37	329,72
0	15	12,57	130,32	0	15	31,20	36,72	0	15	17,28	71,24	0	15	37,20	-18,16
0	16	7,15	126,51	0	16	28,11	34,32	0	16	12,83	64,22	0	16	33,86	-29,08
0	17	6,58	127,78	0	17	24,77	19,88	0	17	8,30	68,00	0	17	28,57	-16,30
1	0	7,18	110,24	1	0	28,80	26,54	1	0	8,35	64,70	1	0	25,90	-27,70
1	1	7,51	-241,80	1	1	29,39	30,70	1	1	14,62	43,40	1	1	33,82	-51,80
1	2	13,66	118,60	1	2	35,00	35,10	1	2	17,14	50,70	1	2	36,32	-40,30
1	3	16,77	-192,30	1	3	37,22	71,70	1	3	20,03	51,00	1	3	41,14	-31,10
1	4	18,43	123,80	1	4	37,81	36,90	1	4	17,69	78,00	1	4	39,01	-22,40
1	5	16,96	-210,70	1	5	37,27	42,00	1	5	23,38	82,10	1	5	44,13	-13,10
1	6	18,19	129,50	1	6	38,02	34,10	1	6	19,77	71,90	1	6	39,95	-5,50
1	7	17,49	145,10	1	7	37,49	58,80	1	7	22,14	48,10	1	7	41,07	-53,40
1	8	19,35	105,00	1	8	38,58	27,10	1	8	22,64	73,20	1	8	41,56	-17,20
1	9	20,50	148,10	1	9	39,79	65,90	1	9	21,70	80,60	1	9	40,73	330,00
1	10	21,12	130,60	1	10	40,21	31,10	1	10	20,51	72,00	1	10	39,92	331,60
1	11	17,49	136,10	1	11	38,01	41,60	1	11	20,60	50,00	1	11	39,93	309,00
1	12	18,51	153,40	1	12	38,48	56,40	1	12	17,90	73,10	1	12	37,55	-16,10
1	13	18,10	123,20	1	13	38,69	34,50	1	13	19,21	61,30	1	13	39,87	323,10
1	14	16,59	141,10	1	14	37,73	50,20	1	14	18,30	67,10	1	14	38,68	347,30
1	15	13,40	151,40	1	15	32,87	74,10	1	15	16,37	55,00	1	15	37,47	335,40
1	16	9,92	141,40	1	16	30,27	64,20	1	16	12,50	45,80	1	16	34,20	327,40
1	17	8,38	150,50	1	17	26,20	66,30	1	17	7,26	59,10	1	17	29,61	328,70
2	0	9,35	114,90	2	0	29,50	29,40	2	0	10,50	50,44	2	0	32,70	-21,26
2	1	10,24	113,86	2	1	30,39	26,76	2	1	13,18	39,94	2	1	34,92	-33,36
2	2	15,03	127,86	2	2	34,90	42,46	2	2	17,62	57,94	2	2	38,92	-10,96
2	3	16,89	124,36	2	3	37,22	25,16	2	3	19,73	39,84	2	3	40,84	-26,16
2	4	17,66	103,06	2	4	38,61	38,46	2	4	18,44	65,54	2	4	38,21	-24,16
2	5	16,43	123,46	2	5	35,67	41,96	2	5	20,98	41,94	2	5	41,53	-50,16
2	6	16,98	165,46	2	6	37,42	65,46	2	6	21,17	64,74	2	6	40,45	-32,16
2	7	19,20	-201,84	2	7	38,19	79,66	2	7	22,39	58,74	2	7	41,67	-34,06
2	8	19,78	142,16	2	8	38,38	43,96	2	8	22,95	58,84	2	8	42,26	-27,36
2	9	21,08	138,96	2	9	39,29	55,36	2	9	22,74	63,54	2	9	42,23	-14,66

2	10	18,80	116,76	2	10	37,91	25,56	2	10	20,49	60,04	2	10	40,22	-17,36
2	11	19,57	147,96	2	11	38,21	53,16	2	11	22,28	65,54	2	11	41,23	-10,46
2	12	20,49	142,76	2	12	40,08	57,06	2	12	19,62	69,64	2	12	40,15	-3,66
2	13	18,56	110,36	2	13	38,39	32,66	2	13	19,57	40,74	2	13	40,27	321,04
2	14	15,47	127,56	2	14	36,63	50,06	2	14	18,72	61,04	2	14	39,78	-19,76
2	15	14,65	149,86	2	15	32,87	60,66	2	15	16,67	84,94	2	15	35,87	-5,46
2	16	12,80	146,26	2	16	31,07	59,36	2	16	13,43	92,14	2	16	31,40	-8,06
2	17	9,96	160,56	2	17	27,40	55,96	2	17	8,64	96,34	2	17	27,01	-13,06
3	0	7,42	114,53	3	0	27,90	24,83	3	0	11,02	76,17	3	0	30,70	-2,63
3	1	9,32	-234,61	3	1	29,19	33,89	3	1	16,30	53,67	3	1	34,62	-26,63
3	2	13,71	130,89	3	2	33,90	41,09	3	2	18,63	64,77	3	2	36,62	-19,33
3	3	14,85	-243,31	3	3	35,82	37,39	3	3	21,00	62,97	3	3	39,44	-6,03
3	4	20,38	115,99	3	4	38,51	46,49	3	4	19,77	39,77	3	4	38,81	-51,53
3	5	16,57	-221,21	3	5	36,37	44,69	3	5	22,36	55,77	3	5	43,03	-29,83
3	6	18,79	136,79	3	6	38,02	45,19	3	6	19,67	41,07	3	6	39,25	-32,33
3	7	18,96	-200,61	3	7	37,79	63,69	3	7	21,29	31,07	3	7	39,17	-42,73
3	8	19,57	-212,91	3	8	38,58	55,49	3	8	22,96	52,37	3	8	41,26	-28,43
3	9	21,89	135,39	3	9	40,89	53,59	3	9	22,34	63,27	3	9	40,33	-24,83
3	10	20,46	138,79	3	10	37,91	41,69	3	10	21,56	72,27	3	10	39,02	-28,43
3	11	19,58	152,99	3	11	37,41	50,39	3	11	22,80	64,47	3	11	41,93	-10,63
3	12	16,74	133,89	3	12	37,88	55,69	3	12	19,38	92,07	3	12	39,85	-10,93
3	13	16,51	115,99	3	13	37,39	37,49	3	13	20,93	69,27	3	13	40,47	-23,83
3	14	13,58	131,99	3	14	33,53	53,89	3	14	18,24	65,77	3	14	37,98	-31,33
3	15	13,82	126,19	3	15	33,17	52,79	3	15	16,81	62,87	3	15	35,87	-7,73
3	16	10,05	110,39	3	16	30,07	38,49	3	16	12,31	66,27	3	16	31,60	-4,93
3	17	9,12	137,49	3	17	28,10	58,79	3	17	8,45	81,87	3	17	29,91	1,27
4	0	8,73	86,58	4	0	28,40	32,58	4	0	10,34	55,57	4	0	29,70	29,17
4	1	7,82	98,04	4	1	28,49	41,04	4	1	13,46	43,97	4	1	33,72	9,17
4	2	14,68	95,24	4	2	33,80	39,84	4	2	15,82	56,47	4	2	36,02	10,77
4	3	16,87	110,04	4	3	36,92	31,74	4	3	20,00	45,27	4	3	38,84	-5,03
4	4	20,27	101,44	4	4	38,01	41,84	4	4	19,17	56,17	4	4	36,61	8,47
4	5	17,08	142,84	4	5	35,97	45,64	4	5	19,60	58,17	4	5	40,63	-3,73
4	6	20,11	134,74	4	6	37,12	62,14	4	6	20,55	48,67	4	6	39,85	-13,83
4	7	21,21	-201,46	4	7	38,69	68,24	4	7	23,04	50,07	4	7	41,77	-26,13
4	8	18,74	149,24	4	8	38,28	69,94	4	8	23,83	61,37	4	8	42,46	-26,43
4	9	21,03	140,74	4	9	38,19	43,04	4	9	22,22	38,47	4	9	41,13	-7,93
4	10	20,56	116,24	4	10	39,31	34,74	4	10	22,36	49,97	4	10	39,52	-38,03
4	11	19,20	145,24	4	11	36,91	72,04	4	11	23,90	40,87	4	11	41,23	-24,03
4	12	18,09	138,04	4	12	39,48	95,14	4	12	18,92	44,57	4	12	37,75	-9,73
4	13	15,74	90,74	4	13	35,79	20,84	4	13	16,05	34,97	4	13	35,77	-29,43
4	14	15,13	110,24	4	14	33,93	19,34	4	14	17,95	49,57	4	14	36,98	-11,13
4	15	12,09	145,34	4	15	30,27	93,44	4	15	15,65	64,17	4	15	35,17	-11,43
4	16	9,07	141,94	4	16	29,67	78,54	4	16	11,72	65,77	4	16	32,00	-15,23
4	17	7,02	157,24	4	17	26,30	91,64	4	17	5,47	48,27	4	17	26,91	-15,53
5	0	7,67	116,40	5	0	27,70	41,60	5	0	6,73	64,28	5	0	28,45	-3,92
5	1	11,18	122,80	5	1	31,62	38,60	5	1	10,37	71,78	5	1	31,69	-11,42
5	2	14,66	121,40	5	2	34,70	37,50	5	2	15,23	67,58	5	2	35,78	-13,52

5	3	18,34	124,40	5	3	37,56	31,60	5	3	17,54	63,88	5	3	37,84	-24,52
5	4	19,62	129,90	5	4	39,67	19,50	5	4	18,32	46,18	5	4	37,69	-31,92
5	5	17,46	134,40	5	5	38,77	57,20	5	5	23,94	50,78	5	5	43,50	-33,62
5	6	18,83	141,90	5	6	36,91	42,60	5	6	21,90	72,38	5	6	41,18	-17,42
5	7	19,57	158,10	5	7	38,93	72,60	5	7	23,16	49,98	5	7	41,09	-43,42
5	8	19,44	130,70	5	8	38,45	11,90	5	8	23,41	74,88	5	8	42,99	-17,72
5	9	21,16	154,70	5	9	40,34	72,10	5	9	23,25	62,48	5	9	42,72	324,88
5	10	20,02	130,10	5	10	39,32	31,40	5	10	22,50	77,38	5	10	41,82	344,78
5	11	18,18	174,20	5	11	36,62	63,50	5	11	20,01	70,38	5	11	38,85	335,88
5	12	20,50	150,50	5	12	37,29	48,50	5	12	16,96	69,88	5	12	38,07	339,88
5	13	19,94	134,20	5	13	38,57	24,00	5	13	20,11	43,38	5	13	40,66	311,88
5	14	18,56	133,30	5	14	39,02	42,30	5	14	18,24	50,18	5	14	38,46	312,68
5	15	14,59	139,20	5	15	32,81	31,80	5	15	17,93	81,38	5	15	38,39	333,48
5	16	13,38	147,60	5	16	30,07	40,40	5	16	13,18	83,68	5	16	33,73	343,58
5	17	9,60	157,70	5	17	26,30	40,10	5	17	12,55	81,48	5	17	32,65	340,38
6	0	9,11	110,99	6	0	28,60	16,39	6	0	11,94	55,48	6	0	31,70	-48,92
6	1	9,80	118,69	6	1	29,49	20,99	6	1	14,94	41,18	6	1	35,62	-58,72
6	2	15,61	118,79	6	2	35,20	15,79	6	2	18,60	49,38	6	2	38,92	-50,72
6	3	18,06	130,69	6	3	37,72	28,39	6	3	21,65	61,68	6	3	41,54	-42,72
6	4	20,22	144,89	6	4	39,51	36,19	6	4	20,93	53,68	6	4	39,51	-39,32
6	5	16,09	134,29	6	5	36,57	26,59	6	5	20,97	43,78	6	5	41,33	-31,92
6	6	17,86	142,49	6	6	38,02	45,69	6	6	20,29	75,68	6	6	40,15	-21,62
6	7	17,99	132,69	6	7	38,29	40,99	6	7	21,16	80,58	6	7	40,07	-21,62
6	8	20,01	126,19	6	8	39,88	22,59	6	8	23,51	99,98	6	8	43,06	-5,52
6	9	21,74	152,69	6	9	39,69	74,19	6	9	20,16	63,48	6	9	39,73	325,68
6	10	21,19	143,89	6	10	40,81	38,69	6	10	16,01	68,18	6	10	36,82	324,98
6	11	19,57	145,09	6	11	37,61	40,29	6	11	19,96	88,18	6	11	37,83	325,18
6	12	18,76	141,69	6	12	37,98	56,79	6	12	20,27	90,38	6	12	39,25	352,58
6	13	18,02	141,79	6	13	38,39	54,79	6	13	20,88	69,78	6	13	40,87	330,38
6	14	17,72	135,59	6	14	36,33	52,29	6	14	19,24	61,88	6	14	39,28	330,28
6	15	14,66	155,29	6	15	34,47	68,59	6	15	17,95	54,78	6	15	37,77	323,18
6	16	12,72	148,59	6	16	32,37	61,59	6	16	12,66	48,08	6	16	33,00	326,08
6	17	10,56	161,99	6	17	29,60	61,39	6	17	9,87	54,48	6	17	27,81	331,28
7	0	7,41	105,04	7	0	27,40	25,84	7	0	9,53	70,76	7	0	29,00	-23,64
7	1	8,09	100,24	7	1	27,39	17,54	7	1	15,06	49,46	7	1	34,32	-35,14
7	2	15,16	107,94	7	2	34,30	28,74	7	2	19,70	47,16	7	2	38,92	-32,14
7	3	16,48	113,94	7	3	35,82	31,44	7	3	20,31	45,36	7	3	40,34	-42,84
7	4	19,10	99,84	7	4	38,61	24,34	7	4	19,92	50,06	7	4	38,21	-43,94
7	5	17,43	-195,66	7	5	37,37	84,64	7	5	24,55	76,56	7	5	43,63	-24,74
7	6	15,24	141,74	7	6	35,12	60,14	7	6	20,67	79,56	7	6	40,35	10,66
7	7	19,41	122,74	7	7	37,29	53,74	7	7	22,54	62,86	7	7	40,67	-20,74
7	8	18,17	136,64	7	8	35,28	32,64	7	8	24,78	82,16	7	8	41,56	-19,64
7	9	22,34	184,64	7	9	39,19	93,54	7	9	24,19	72,06	7	9	42,13	345,26
7	10	19,28	125,44	7	10	38,51	27,14	7	10	20,19	56,56	7	10	39,42	335,86
7	11	18,78	171,04	7	11	37,31	68,94	7	11	21,76	49,46	7	11	40,93	317,46
7	12	20,04	145,84	7	12	39,98	71,84	7	12	18,66	70,16	7	12	36,85	341,76
7	13	17,68	118,34	7	13	36,69	13,54	7	13	21,40	47,56	7	13	41,17	317,06

7	14	17,74	133,34	7	14	36,23	40,54	7	14	20,06	52,96	7	14	38,88	316,46
7	15	15,35	113,14	7	15	34,37	51,94	7	15	14,86	86,16	7	15	37,37	330,36
7	16	10,89	97,14	7	16	30,77	41,74	7	16	10,28	100,66	7	16	33,10	321,86
7	17	9,14	112,34	7	17	27,80	46,04	7	17	5,82	128,56	7	17	28,41	339,16
8	0	6,02	124,80	8	0	24,80	52,70	8	0	8,35	49,39	8	0	24,80	-25,71
8	1	7,26	129,70	8	1	27,79	55,50	8	1	13,43	30,99	8	1	32,52	-44,91
8	2	11,23	133,50	8	2	30,10	58,40	8	2	17,27	49,99	8	2	36,82	-30,41
8	3	14,73	113,30	8	3	35,92	32,00	8	3	19,31	41,09	8	3	38,94	-27,41
8	4	12,74	111,50	8	4	33,91	13,50	8	4	20,12	45,39	8	4	38,91	-46,31
8	5	17,40	141,60	8	5	37,07	51,10	8	5	23,24	53,89	8	5	43,13	-12,21
8	6	17,90	166,30	8	6	37,22	51,80	8	6	22,93	80,39	8	6	40,45	-3,71
8	7	18,85	163,30	8	7	38,49	73,30	8	7	22,82	67,09	8	7	39,77	-29,91
8	8	19,23	150,60	8	8	36,68	71,40	8	8	24,45	94,29	8	8	40,56	-2,11
8	9	19,18	144,00	8	9	38,39	66,60	8	9	23,45	58,79	8	9	42,03	330,09
8	10	18,56	123,10	8	10	38,21	25,10	8	10	22,41	66,89	8	10	40,52	325,89
8	11	17,83	140,50	8	11	37,11	27,90	8	11	22,20	52,09	8	11	41,13	323,19
8	12	18,99	145,00	8	12	37,98	55,30	8	12	20,31	69,19	8	12	40,55	333,89
8	13	15,85	109,50	8	13	37,09	34,40	8	13	21,15	51,89	8	13	40,17	312,79
8	14	15,46	126,90	8	14	36,33	15,20	8	14	19,77	57,29	8	14	39,38	333,79
8	15	13,33	131,60	8	15	31,97	36,30	8	15	17,93	75,09	8	15	37,97	347,79
8	16	9,55	124,60	8	16	29,07	28,80	8	16	12,67	71,79	8	16	34,00	342,49
8	17	6,69	136,90	8	17	25,50	34,60	8	17	9,34	65,19	8	17	28,11	347,99
9	0	7,68	139,20	9	0	27,60	26,20	9	0	10,67	51,70	9	0	29,20	-73,80
9	1	7,92	106,10	9	1	28,69	22,80	9	1	13,88	57,80	9	1	31,42	-76,70
9	2	13,35	138,10	9	2	33,90	22,00	9	2	16,70	64,60	9	2	35,12	-51,70
9	3	15,67	122,20	9	3	36,32	42,00	9	3	19,40	41,20	9	3	40,24	-52,50
9	4	16,16	93,40	9	4	37,21	6,40	9	4	18,53	63,90	9	4	38,31	-47,60
9	5	17,27	150,40	9	5	38,07	72,80	9	5	23,69	73,30	9	5	41,53	-44,80
9	6	16,56	167,90	9	6	35,92	36,10	9	6	19,62	80,90	9	6	38,55	-7,80
9	7	17,90	156,10	9	7	37,09	77,80	9	7	22,46	52,20	9	7	39,97	-30,00
9	8	18,79	133,40	9	8	37,38	-6,90	9	8	23,56	56,10	9	8	40,76	-45,70
9	9	19,95	136,90	9	9	38,79	66,50	9	9	22,74	61,90	9	9	40,63	325,40
9	10	19,57	124,10	9	10	38,91	12,10	9	10	21,69	70,60	9	10	40,12	343,90
9	11	18,93	154,20	9	11	37,01	56,00	9	11	22,28	59,40	9	11	41,03	338,20
9	12	18,94	154,70	9	12	37,68	62,80	9	12	18,40	82,10	9	12	38,15	348,90
9	13	16,09	115,50	9	13	36,69	35,80	9	13	20,34	95,10	9	13	39,57	352,90
9	14	16,59	135,10	9	14	36,03	43,40	9	14	15,00	88,90	9	14	35,08	362,50
9	15	13,37	163,00	9	15	32,17	67,00	9	15	15,47	81,90	9	15	34,87	336,50
9	16	11,90	156,40	9	16	29,27	59,30	9	16	12,61	84,30	9	16	31,00	332,50
9	17	10,73	169,50	9	17	26,60	45,00	9	17	8,66	82,40	9	17	28,81	340,60
10	0	4,46	124,69	10	0	25,20	43,39	10	0	9,65	82,55	10	0	30,60	7,95
10	1	5,96	134,29	10	1	27,19	46,49	10	1	13,49	65,85	10	1	33,92	-12,75
10	2	11,28	130,39	10	2	31,60	49,09	10	2	16,45	68,15	10	2	36,52	-10,25
10	3	10,87	120,59	10	3	32,12	20,99	10	3	18,91	53,35	10	3	38,84	-33,15
10	4	18,99	114,19	10	4	37,91	30,79	10	4	19,22	55,55	10	4	38,71	-32,35
10	5	16,80	157,69	10	5	37,77	74,99	10	5	21,55	66,45	10	5	41,93	-7,15
10	6	17,37	163,99	10	6	36,22	55,09	10	6	19,97	63,65	10	6	40,25	-5,05

10	7	18,62	127,29	10	7	38,59	51,69	10	7	21,24	57,45	10	7	39,87	-27,25
10	8	18,55	127,99	10	8	38,48	46,99	10	8	22,63	54,25	10	8	42,36	-27,55
10	9	20,42	154,19	10	9	38,59	76,89	10	9	21,28	52,75	10	9	40,03	318,85
10	10	17,77	130,59	10	10	36,51	49,19	10	10	19,06	51,25	10	10	37,22	333,55
10	11	18,36	150,59	10	11	36,91	63,09	10	11	19,43	49,15	10	11	38,93	320,85
10	12	18,24	139,19	10	12	38,78	50,89	10	12	17,69	63,05	10	12	38,25	333,55
10	13	17,83	100,09	10	13	38,99	19,79	10	13	17,75	43,25	10	13	37,47	322,25
10	14	15,94	140,09	10	14	36,23	1,59	10	14	17,13	71,15	10	14	37,88	351,25
10	15	13,74	132,39	10	15	30,87	63,79	10	15	16,02	65,65	10	15	36,67	352,75
10	16	9,51	115,49	10	16	30,27	44,89	10	16	12,05	58,35	10	16	33,10	343,55
10	17	7,42	131,99	10	17	27,90	51,89	10	17	7,77	66,35	10	17	27,41	349,85
11	0	6,47	153,19	11	0	26,40	48,49	11	0	8,58	84,40	11	0	30,50	8,50
11	1	8,12	148,79	11	1	26,79	46,79	11	1	15,14	65,80	11	1	34,42	-22,70
11	2	11,62	146,49	11	2	32,20	42,59	11	2	18,83	67,30	11	2	36,82	-16,00
11	3	15,74	92,39	11	3	34,02	17,59	11	3	20,87	73,00	11	3	40,54	-17,30
11	4	19,88	133,09	11	4	38,01	33,59	11	4	18,49	52,40	11	4	38,51	-19,70
11	5	16,32	156,69	11	5	35,77	70,89	11	5	23,04	65,40	11	5	42,03	-14,40
11	6	19,66	144,89	11	6	36,72	64,39	11	6	21,93	81,10	11	6	40,05	-4,50
11	7	16,73	170,79	11	7	33,29	73,59	11	7	22,35	52,40	11	7	40,97	-8,70
11	8	21,20	134,19	11	8	39,18	48,29	11	8	22,59	49,80	11	8	41,16	-23,00
11	9	16,31	134,09	11	9	33,59	55,19	11	9	23,49	64,80	11	9	41,53	318,90
11	10	20,43	115,89	11	10	38,21	30,39	11	10	20,44	40,70	11	10	39,22	311,10
11	11	18,86	138,79	11	11	37,01	42,39	11	11	19,92	39,60	11	11	40,03	335,40
11	12	18,15	123,89	11	12	36,88	46,29	11	12	18,97	61,80	11	12	38,85	353,00
11	13	12,98	127,79	11	13	32,89	32,59	11	13	20,07	38,80	11	13	37,17	304,10
11	14	17,30	143,89	11	14	35,83	45,39	11	14	19,63	59,70	11	14	38,88	329,40
11	15	13,99	138,59	11	15	31,77	58,69	11	15	16,85	56,80	11	15	36,97	339,20
11	16	9,57	123,59	11	16	28,67	38,69	11	16	13,40	50,10	11	16	32,40	343,80
11	17	8,61	144,39	11	17	26,70	49,29	11	17	9,39	70,40	11	17	25,81	350,60
12	0	8,50	122,27	12	0	30,10	28,17	12	0	11,60	81,20	12	0	31,30	-6,80
12	1	9,77	134,57	12	1	30,69	35,97	12	1	15,71	54,20	12	1	35,92	-34,70
12	2	14,83	127,37	12	2	36,20	31,67	12	2	18,89	73,80	12	2	39,02	-17,40
12	3	15,68	130,57	12	3	35,92	49,17	12	3	22,65	37,20	12	3	42,14	-47,10
12	4	19,32	109,77	12	4	39,11	10,37	12	4	20,32	48,60	12	4	40,01	-38,80
12	5	17,29	156,27	12	5	37,57	51,97	12	5	19,99	58,90	12	5	41,63	-28,90
12	6	17,81	137,17	12	6	37,82	29,77	12	6	20,87	84,60	12	6	40,75	-11,00
12	7	19,32	134,67	12	7	39,09	54,07	12	7	20,14	46,40	12	7	40,37	-38,10
12	8	19,05	123,67	12	8	38,68	48,07	12	8	23,03	67,60	12	8	42,46	-24,20
12	9	18,49	122,37	12	9	37,29	31,87	12	9	21,11	52,70	12	9	40,23	324,60
12	10	19,91	138,87	12	10	40,01	47,17	12	10	20,35	90,60	12	10	40,12	335,30
12	11	16,52	152,07	12	11	35,11	58,57	12	11	19,71	59,50	12	11	39,33	325,80
12	12	19,65	165,27	12	12	39,48	72,97	12	12	18,21	64,20	12	12	38,35	341,00
12	13	14,77	112,77	12	13	34,19	24,37	12	13	20,15	54,40	12	13	40,77	328,10
12	14	15,17	123,17	12	14	35,23	37,57	12	14	18,18	52,70	12	14	38,18	322,60
12	15	13,71	165,57	12	15	34,17	76,87	12	15	15,66	97,20	12	15	36,37	9,20
12	16	12,06	153,77	12	16	32,67	62,77	12	16	12,25	101,50	12	16	33,10	11,40
12	17	11,03	170,27	12	17	31,50	76,37	12	17	4,87	83,30	12	17	24,41	6,60

13	0	6,23	148,74	13	0	27,20	41,94	13	0	8,88	83,27	13	0	31,30	-35,63
13	1	8,86	147,64	13	1	28,19	42,84	13	1	15,36	68,07	13	1	36,12	-52,53
13	2	12,19	150,14	13	2	33,00	47,24	13	2	19,37	66,07	13	2	39,42	-49,03
13	3	16,94	134,24	13	3	36,72	26,94	13	3	21,11	58,67	13	3	40,04	-54,33
13	4	18,34	146,84	13	4	38,61	59,44	13	4	19,25	40,47	13	4	38,21	-41,73
13	5	16,68	139,44	13	5	37,47	35,84	13	5	21,31	92,77	13	5	41,33	-4,93
13	6	19,71	124,14	13	6	37,42	55,64	13	6	21,34	84,57	13	6	40,15	-17,63
13	7	21,02	141,44	13	7	37,99	52,04	13	7	20,60	43,17	13	7	38,67	-50,33
13	8	19,99	117,34	13	8	37,48	17,04	13	8	23,92	72,27	13	8	42,46	-10,03
13	9	21,87	117,64	13	9	39,59	33,35	13	9	22,96	65,87	13	9	40,93	325,87
13	10	21,75	107,94	13	10	40,51	14,95	13	10	22,26	83,17	13	10	40,72	337,17
13	11	16,36	153,74	13	11	33,81	48,24	13	11	18,91	38,87	13	11	39,53	298,77
13	12	13,47	201,94	13	12	34,68	117,74	13	12	17,02	72,57	13	12	37,35	336,27
13	13	17,35	154,24	13	13	36,09	51,65	13	13	20,27	51,57	13	13	39,47	339,07
13	14	17,09	131,14	13	14	35,23	51,15	13	14	16,67	60,77	13	14	35,78	329,57
13	15	12,42	164,94	13	15	32,97	63,85	13	15	16,53	88,17	13	15	36,27	342,27
13	16	10,45	160,04	13	16	29,77	58,25	13	16	12,57	87,47	13	16	32,20	337,97
13	17	8,98	173,14	13	17	28,30	52,25	13	17	6,70	89,97	13	17	27,51	346,97
14	0	6,67	114,69	14	0	27,20	4,89	14	0	4,90	95,41	14	0	28,40	6,91
14	1	6,38	126,39	14	1	26,99	9,99	14	1	9,30	57,91	14	1	33,12	-31,39
14	2	12,60	122,19	14	2	33,10	5,89	14	2	13,42	61,91	14	2	35,92	-25,39
14	3	12,40	152,49	14	3	34,22	52,79	14	3	20,91	34,61	14	3	40,84	-40,59
14	4	19,27	112,49	14	4	38,91	6,79	14	4	18,52	63,01	14	4	38,31	-28,29
14	5	16,34	140,89	14	5	37,97	26,89	14	5	22,67	56,21	14	5	43,73	-36,79
14	6	17,75	153,19	14	6	36,62	23,39	14	6	21,45	69,81	14	6	40,55	-23,89
14	7	17,49	157,99	14	7	37,29	45,59	14	7	22,42	65,51	14	7	41,87	-51,99
14	8	20,59	134,79	14	8	39,28	29,29	14	8	22,35	76,31	14	8	41,16	-30,79
14	9	17,93	156,09	14	9	38,59	21,29	14	9	22,71	65,31	14	9	41,93	316,81
14	10	17,45	122,19	14	10	36,91	15,89	14	10	21,13	92,21	14	10	40,52	343,21
14	11	18,20	185,39	14	11	37,61	83,99	14	11	20,67	70,11	14	11	40,93	335,01
14	12	20,41	179,79	14	12	40,48	71,89	14	12	16,77	95,91	14	12	37,85	4,21
14	13	18,87	126,39	14	13	38,09	36,19	14	13	17,07	65,11	14	13	37,17	319,91
14	14	14,93	130,09	14	14	35,73	53,89	14	14	14,41	29,41	14	14	33,78	298,41
14	15	14,25	168,49	14	15	34,47	54,69	14	15	16,74	71,31	14	15	37,07	342,71
14	16	10,79	144,09	14	16	30,37	25,19	14	16	12,47	72,01	14	16	33,60	347,71
14	17	10,08	169,19	14	17	30,40	44,79	14	17	7,58	76,51	14	17	29,01	349,01
15	0	5,97	147,54	15	0	28,00	39,84	15	0	1,45	88,91	15	0	26,50	-8,19
15	1	8,80	154,54	15	1	29,69	41,44	15	1	8,48	74,81	15	1	32,42	-24,99
15	2	13,03	139,94	15	2	34,30	21,44	15	2	12,97	78,31	15	2	35,22	-17,69
15	3	17,81	135,94	15	3	37,72	27,14	15	3	21,41	60,81	15	3	41,94	-35,49
15	4	19,26	131,94	15	4	38,41	20,04	15	4	19,72	61,51	15	4	39,01	-52,89
15	5	15,33	142,34	15	5	37,17	35,64	15	5	22,42	64,71	15	5	43,33	-41,99
15	6	17,37	133,84	15	6	37,42	47,34	15	6	20,38	86,11	15	6	39,95	-23,59
15	7	20,03	150,54	15	7	39,59	58,64	15	7	22,37	73,61	15	7	41,37	-46,49
15	8	18,87	130,74	15	8	37,38	-4,96	15	8	22,20	82,91	15	8	40,86	-48,09
15	9	21,70	158,84	15	9	39,89	41,74	15	9	22,57	72,01	15	9	41,63	312,91
15	10	20,56	150,34	15	10	41,01	34,94	15	10	19,86	85,41	15	10	40,02	339,51

15	11	16,96	143,24	15	11	36,91	19,64	15	11	21,93	80,21	15	11	42,03	331,11
15	12	18,02	162,64	15	12	38,98	60,64	15	12	18,04	82,91	15	12	39,05	334,11
15	13	18,58	141,64	15	13	38,39	39,14	15	13	21,30	72,61	15	13	40,87	330,31
15	14	18,24	159,94	15	14	39,13	47,54	15	14	17,62	41,21	15	14	37,58	294,71
15	15	14,67	143,64	15	15	34,17	42,54	15	15	17,53	68,81	15	15	38,37	331,31
15	16	11,38	137,64	15	16	31,77	35,04	15	16	11,05	65,11	15	16	33,10	330,61
15	17	9,10	149,74	15	17	28,90	42,44	15	17	7,59	65,51	15	17	30,21	336,31
16	0	8,80	89,23	16	0	28,90	35,83	16	0	4,38	103,54	16	0	28,60	32,64
16	1	7,48	105,23	16	1	29,49	48,73	16	1	12,17	59,84	16	1	33,02	-16,16
16	2	14,62	99,33	16	2	34,50	42,53	16	2	16,13	61,14	16	2	36,42	-13,56
16	3	17,23	129,33	16	3	36,72	37,03	16	3	21,04	42,64	16	3	40,24	-52,66
16	4	19,21	108,73	16	4	38,21	27,73	16	4	17,93	36,74	16	4	38,41	-42,86
16	5	18,79	163,33	16	5	38,37	74,33	16	5	19,98	76,74	16	5	42,63	-17,36
16	6	16,39	146,23	16	6	37,02	60,83	16	6	16,92	90,64	16	6	39,05	26,14
16	7	17,87	166,33	16	7	37,19	71,23	16	7	20,57	51,84	16	7	40,77	-42,46
16	8	17,76	102,03	16	8	36,08	37,03	16	8	21,81	85,84	16	8	42,16	-9,16
16	9	19,89	135,73	16	9	39,69	36,03	16	9	22,44	59,64	16	9	42,63	335,04
16	10	20,34	104,73	16	10	39,01	20,43	16	10	20,35	64,24	16	10	40,22	338,34
16	11	18,67	160,73	16	11	38,61	63,13	16	11	21,30	69,54	16	11	41,53	337,74
16	12	20,01	169,23	16	12	40,58	83,73	16	12	18,97	65,24	16	12	39,95	345,34
16	13	12,85	116,63	16	13	32,29	33,53	16	13	20,44	39,04	16	13	40,37	319,04
16	14	17,35	130,03	16	14	37,73	43,63	16	14	16,41	6,24	16	14	36,08	301,44
16	15	15,28	136,43	16	15	35,37	51,43	16	15	16,11	59,04	16	15	36,17	334,64
16	16	10,82	126,53	16	16	31,77	39,33	16	16	9,77	66,44	16	16	30,80	343,24
16	17	11,15	142,33	16	17	31,60	48,33	16	17	4,59	81,64	16	17	27,31	-1,36
17	0	7,10	134,16	17	0	25,30	52,96	17	0	10,31	39,53	17	0	30,80	-16,47
17	1	8,91	145,16	17	1	27,29	57,56	17	1	15,38	29,33	17	1	36,02	-44,17
17	2	13,82	128,26	17	2	31,00	39,96	17	2	18,14	55,13	17	2	38,32	-18,17
17	3	17,64	119,66	17	3	36,22	24,96	17	3	22,17	41,63	17	3	41,34	-39,27
17	4	20,73	97,56	17	4	38,81	39,36	17	4	20,18	55,03	17	4	38,71	-25,77
17	5	17,85	151,06	17	5	36,27	82,56	17	5	24,27	53,83	17	5	42,73	-38,47
17	6	19,11	146,56	17	6	37,42	47,66	17	6	20,68	81,43	17	6	40,45	-15,97
17	7	18,81	133,96	17	7	37,09	54,96	17	7	23,21	21,63	17	7	41,97	-56,27
17	8	20,65	119,86	17	8	39,18	36,26	17	8	23,06	38,43	17	8	42,06	-36,07
17	9	21,07	162,76	17	9	37,79	46,36	17	9	21,92	79,93	17	9	39,53	369,73
17	10	20,75	126,96	17	10	39,61	35,36	17	10	20,22	46,13	17	10	39,92	332,03
17	11	19,11	142,86	17	11	38,31	52,66	17	11	22,68	85,03	17	11	41,03	345,63
17	12	20,14	145,66	17	12	40,08	45,36	17	12	18,85	93,63	17	12	39,05	356,23
17	13	18,72	115,96	17	13	36,19	46,76	17	13	21,74	75,53	17	13	39,97	342,63
17	14	15,83	104,86	17	14	35,13	25,16	17	14	17,72	42,33	17	14	36,48	335,43
17	15	13,77	159,46	17	15	33,27	77,56	17	15	18,67	82,43	17	15	37,37	371,23
17	16	10,75	156,76	17	16	31,37	73,46	17	16	13,73	82,83	17	16	33,40	365,53
17	17	10,26	172,16	17	17	31,30	77,76	17	17	9,53	98,23	17	17	27,01	375,03

lhrsc				lhtsc				lvrsc				lvtsc			
0	0	-2,85	117,10	0	0	29,90	129,50	0	0	-1,98	-126,67	0	0	27,90	-134,47
0	1	0,48	127,80	0	1	33,00	136,60	0	1	-1,09	-105,87	0	1	29,20	-118,87
0	2	4,82	126,20	0	2	37,40	145,20	0	2	2,87	-85,37	0	2	32,30	-108,37
0	3	6,40	123,90	0	3	38,30	129,80	0	3	5,44	-138,07	0	3	36,40	-124,57
0	4	6,46	132,90	0	4	37,90	132,60	0	4	6,08	-126,77	0	4	37,00	-132,37
0	5	8,87	130,30	0	5	41,40	151,30	0	5	7,59	-109,27	0	5	39,20	-117,07
0	6	9,67	131,50	0	6	42,10	150,90	0	6	8,71	-100,87	0	6	39,70	-108,27
0	7	8,36	135,30	0	7	41,40	136,60	0	7	8,43	-85,37	0	7	38,90	-94,17
0	8	8,10	115,20	0	8	41,20	149,10	0	8	9,60	-99,27	0	8	39,80	-115,07
0	9	9,68	113,80	0	9	41,50	121,80	0	9	8,81	-106,15	0	9	40,00	-112,35
0	10	9,75	131,60	0	10	41,80	140,00	0	10	7,63	-88,95	0	10	39,60	-107,85
0	11	10,83	140,90	0	11	42,40	153,00	0	11	7,39	-108,05	0	11	39,40	-111,85
0	12	9,23	137,40	0	12	41,50	142,80	0	12	6,41	-126,55	0	12	38,50	-135,25
0	13	7,24	121,80	0	13	38,10	140,60	0	13	6,24	-104,55	0	13	37,40	-111,75
0	14	6,71	131,50	0	14	38,60	142,30	0	14	4,24	-105,65	0	14	36,10	-106,35
0	15	5,34	137,80	0	15	36,50	143,70	0	15	3,03	-108,85	0	15	34,80	-110,45
0	16	1,47	133,50	0	16	32,90	130,80	0	16	-1,59	-100,15	0	16	30,50	-114,35
0	17	-1,60	122,80	0	17	29,70	126,40	0	17	-1,78	-117,35	0	17	30,10	-124,75
1	0	-2,71	99,22	1	0	29,10	148,22	1	0	-2,39	-148,20	1	0	29,30	-118,60
1	1	0,37	109,12	1	1	32,30	-206,58	1	1	-2,06	-121,40	1	1	29,80	-99,40
1	2	4,90	102,12	1	2	36,60	152,12	1	2	2,57	-97,40	1	2	33,30	-75,20
1	3	6,17	117,32	1	3	38,00	-192,48	1	3	4,70	-118,00	1	3	36,30	-86,60
1	4	7,19	119,32	1	4	37,80	-191,68	1	4	7,06	-109,00	1	4	37,20	-88,60
1	5	8,98	114,72	1	5	40,90	151,72	1	5	6,31	-122,00	1	5	38,40	-125,30
1	6	9,15	112,82	1	6	41,00	-187,28	1	6	7,95	-120,80	1	6	39,60	-112,70
1	7	9,61	120,92	1	7	40,70	-194,48	1	7	7,77	-108,70	1	7	38,90	-107,30
1	8	9,20	92,12	1	8	40,60	142,92	1	8	8,61	-121,60	1	8	39,30	-110,90
1	9	9,56	101,70	1	9	41,40	134,70	1	9	9,53	-123,13	1	9	38,90	-96,53
1	10	10,33	124,50	1	10	42,40	138,40	1	10	9,15	-131,03	1	10	37,80	-85,33
1	11	9,53	120,70	1	11	41,70	150,10	1	11	8,13	-126,03	1	11	39,00	-90,43
1	12	8,79	130,90	1	12	41,60	143,70	1	12	7,16	-129,13	1	12	37,50	-106,23
1	13	6,95	132,50	1	13	38,40	168,50	1	13	6,38	-124,13	1	13	36,10	-80,83
1	14	6,64	137,80	1	14	38,70	166,20	1	14	4,52	-135,03	1	14	33,70	-92,13
1	15	5,09	119,40	1	15	36,70	146,80	1	15	2,38	-119,33	1	15	31,20	-69,93
1	16	0,57	122,10	1	16	32,70	141,50	1	16	-2,01	-134,23	1	16	27,80	-101,73
1	17	-2,85	111,20	1	17	28,80	138,40	1	17	-2,48	-163,93	1	17	27,10	-121,63
2	0	-2,45	126,70	2	0	31,80	133,30	2	0	-2,18	-121,65	2	0	29,80	-141,55
2	1	0,88	133,20	2	1	33,30	138,30	2	1	-2,01	-89,65	2	1	30,20	-120,45
2	2	4,52	138,70	2	2	36,80	174,50	2	2	2,65	-75,45	2	2	34,50	-89,45
2	3	6,14	129,30	2	3	34,80	147,60	2	3	4,99	-120,25	2	3	36,70	-116,55
2	4	5,89	121,60	2	4	33,50	128,10	2	4	5,89	-117,05	2	4	37,00	-97,65
2	5	9,65	124,50	2	5	36,40	123,70	2	5	7,39	-123,15	2	5	39,60	-128,15
2	6	10,83	150,60	2	6	42,80	147,80	2	6	7,03	-108,55	2	6	39,50	-110,75
2	7	10,76	125,00	2	7	40,90	139,00	2	7	8,25	-89,85	2	7	39,30	-110,25
2	8	9,69	127,80	2	8	42,80	121,20	2	8	8,50	-105,95	2	8	39,50	-123,15
2	9	9,16	102,28	2	9	41,20	133,78	2	9	12,13	-98,83	2	9	40,40	-103,83

2	10	9,15	130,18	2	10	41,80	163,18	2	10	8,52	-115,93	2	10	39,60	-112,93
2	11	10,21	116,28	2	11	42,10	167,68	2	11	8,40	-114,93	2	11	40,00	-100,43
2	12	8,35	121,08	2	12	41,20	157,88	2	12	7,51	-139,43	2	12	38,80	-116,83
2	13	5,88	105,28	2	13	37,80	150,18	2	13	7,40	-120,83	2	13	37,40	-98,23
2	14	5,77	113,18	2	14	37,50	162,48	2	14	4,87	-141,53	2	14	35,30	-111,23
2	15	4,37	112,28	2	15	36,20	153,68	2	15	2,87	-103,63	2	15	33,20	-54,33
2	16	0,00	116,78	2	16	32,30	154,18	2	16	-2,48	-125,63	2	16	28,20	-83,53
2	17	-2,53	102,88	2	17	30,00	146,38	2	17	-2,68	-148,43	2	17	27,90	-103,93
3	0	-2,00	134,15	3	0	29,70	144,25	3	0	-1,61	-117,86	3	0	30,00	-123,46
3	1	0,85	147,45	3	1	32,80	146,75	3	1	-2,50	-109,56	3	1	29,40	-119,96
3	2	5,54	142,95	3	2	36,80	145,35	3	2	2,65	-83,65	3	2	34,40	-89,15
3	3	5,97	137,85	3	3	37,70	156,25	3	3	5,73	-122,56	3	3	36,10	-101,06
3	4	6,74	144,85	3	4	38,10	150,15	3	4	7,30	-118,96	3	4	37,40	-93,65
3	5	9,39	121,75	3	5	41,70	125,45	3	5	6,05	-128,36	3	5	38,70	-122,86
3	6	9,36	125,45	3	6	41,50	148,05	3	6	7,36	-114,16	3	6	39,10	-110,76
3	7	10,06	116,05	3	7	41,80	135,05	3	7	7,55	-114,16	3	7	38,80	-97,85
3	8	9,53	113,45	3	8	41,00	140,35	3	8	9,07	-113,66	3	8	40,60	-106,96
3	9	9,07	110,33	3	9	40,40	144,53	3	9	9,46	-109,49	3	9	39,90	-111,69
3	10	9,83	131,63	3	10	40,70	-200,37	3	10	8,12	-88,09	3	10	38,90	-100,99
3	11	10,09	129,03	3	11	41,60	-195,87	3	11	7,90	-107,19	3	11	39,50	-107,49
3	12	8,65	124,73	3	12	40,90	147,73	3	12	7,05	-127,19	3	12	39,30	-126,39
3	13	6,64	93,93	3	13	36,30	146,33	3	13	6,51	-120,49	3	13	37,20	-98,69
3	14	6,61	113,23	3	14	37,30	145,63	3	14	4,92	-116,89	3	14	36,40	-97,89
3	15	4,30	115,13	3	15	35,60	-199,57	3	15	1,96	-106,69	3	15	34,50	-92,69
3	16	0,24	110,23	3	16	31,50	153,33	3	16	-2,37	-120,19	3	16	30,80	-116,79
3	17	-2,86	95,43	3	17	28,50	147,13	3	17	-2,83	-149,99	3	17	29,80	-140,39
4	0	-2,89	111,15	4	0	29,70	134,35	4	0	-0,67	-121,85	4	0	28,40	-131,85
4	1	0,69	125,75	4	1	32,80	139,25	4	1	-0,81	-88,05	4	1	27,70	-102,85
4	2	3,64	119,45	4	2	36,10	148,15	4	2	2,79	-97,05	4	2	31,20	-104,15
4	3	6,92	140,35	4	3	38,60	167,65	4	3	3,97	-129,95	4	3	34,20	-112,35
4	4	6,33	137,65	4	4	38,20	175,35	4	4	5,83	-116,25	4	4	35,50	-107,75
4	5	8,98	94,65	4	5	40,90	126,55	4	5	6,68	-114,75	4	5	37,70	-122,05
4	6	9,30	153,55	4	6	41,10	180,45	4	6	6,93	-103,25	4	6	37,80	-118,65
4	7	9,18	111,85	4	7	41,90	150,65	4	7	7,67	-110,15	4	7	37,90	-105,05
4	8	9,15	99,15	4	8	41,10	111,55	4	8	8,07	-98,35	4	8	38,40	-107,55
4	9	9,54	96,64	4	9	40,70	163,54	4	9	8,50	-116,20	4	9	38,90	-67,80
4	10	8,72	94,34	4	10	40,90	154,34	4	10	5,25	-121,10	4	10	37,90	-69,90
4	11	9,47	115,84	4	11	41,30	175,44	4	11	6,51	-144,80	4	11	37,90	-81,70
4	12	9,44	107,14	4	12	40,20	173,94	4	12	6,61	-157,20	4	12	38,30	-108,30
4	13	6,38	99,04	4	13	37,40	164,54	4	13	5,86	-142,00	4	13	36,80	-88,00
4	14	6,19	107,14	4	14	38,30	174,34	4	14	4,50	-134,70	4	14	34,60	-88,20
4	15	5,78	107,24	4	15	36,00	164,74	4	15	2,33	-133,80	4	15	32,70	-67,10
4	16	1,25	106,54	4	16	32,00	156,44	4	16	-1,70	-130,30	4	16	28,70	-102,70
4	17	-2,16	97,94	4	17	28,40	154,64	4	17	-2,17	-158,80	4	17	28,00	-126,00
5	0	-2,22	113,51	5	0	28,70	122,61	5	0	-1,74	-111,00	5	0	29,90	-139,00
5	1	0,76	123,61	5	1	32,60	138,11	5	1	-1,84	-79,40	5	1	29,80	-113,20
5	2	4,76	126,31	5	2	38,30	148,21	5	2	2,45	-76,20	5	2	34,10	-93,90

5	3	6,05	130,71	5	3	40,00	-196,99	5	3	4,79	-94,80	5	3	36,60	-116,60
5	4	5,99	118,61	5	4	39,00	-193,79	5	4	5,66	-106,40	5	4	37,20	-138,50
5	5	7,83	114,91	5	5	40,60	132,21	5	5	6,87	-123,60	5	5	38,50	-143,70
5	6	9,01	134,71	5	6	38,30	-188,29	5	6	6,89	-95,70	5	6	38,60	-120,50
5	7	9,30	115,41	5	7	39,00	147,11	5	7	7,26	-85,40	5	7	39,10	-120,60
5	8	10,18	109,41	5	8	39,00	135,61	5	8	8,09	-96,70	5	8	40,10	-118,70
5	9	9,41	87,03	5	9	40,30	142,93	5	9	8,66	-124,34	5	9	39,20	-99,54
5	10	10,32	101,93	5	10	40,40	154,23	5	10	8,28	-118,54	5	10	38,40	-87,24
5	11	11,54	123,63	5	11	41,40	160,53	5	11	7,10	-122,84	5	11	38,10	-95,74
5	12	8,76	109,83	5	12	41,10	160,23	5	12	6,88	-149,14	5	12	38,10	-121,64
5	13	6,58	118,53	5	13	36,40	168,93	5	13	6,57	-116,94	5	13	36,60	-91,44
5	14	5,94	127,13	5	14	37,90	164,03	5	14	4,85	-125,34	5	14	34,90	-88,24
5	15	4,97	116,43	5	15	34,60	174,73	5	15	2,18	-110,24	5	15	32,40	-66,44
5	16	0,70	115,53	5	16	30,60	162,13	5	16	-2,03	-121,34	5	16	28,80	-91,94
5	17	-2,62	102,53	5	17	27,80	151,83	5	17	-2,17	-145,54	5	17	28,00	-111,24
6	0	-2,80	121,12	6	0	30,10	151,62	6	0	-2,94	-139,14	6	0	28,80	-131,04
6	1	0,38	133,72	6	1	33,00	151,72	6	1	-2,67	-101,74	6	1	29,40	-100,04
6	2	4,42	124,12	6	2	37,30	157,82	6	2	2,14	-99,44	6	2	34,00	-84,64
6	3	6,88	133,72	6	3	38,50	158,02	6	3	4,90	-116,14	6	3	36,60	-97,64
6	4	6,92	133,82	6	4	38,60	151,02	6	4	5,72	-114,34	6	4	36,70	-106,74
6	5	8,98	120,72	6	5	41,60	132,32	6	5	6,84	-129,04	6	5	39,20	-122,54
6	6	11,01	141,12	6	6	42,70	151,82	6	6	7,68	-105,94	6	6	39,70	-101,74
6	7	10,03	127,72	6	7	42,10	137,22	6	7	7,58	-113,64	6	7	39,20	-112,24
6	8	9,49	102,22	6	8	41,90	123,12	6	8	8,93	-116,84	6	8	39,90	-101,84
6	9	9,77	114,33	6	9	41,70	144,83	6	9	9,03	-110,21	6	9	40,20	-119,61
6	10	9,73	115,83	6	10	41,40	146,73	6	10	8,33	-96,71	6	10	39,90	-95,91
6	11	10,22	134,03	6	11	41,80	164,33	6	11	9,96	-105,01	6	11	40,70	-111,31
6	12	9,24	117,83	6	12	41,50	140,13	6	12	7,52	-115,41	6	12	39,40	-128,01
6	13	6,29	106,23	6	13	38,00	141,33	6	13	6,40	-124,11	6	13	37,60	-123,51
6	14	6,35	118,23	6	14	38,50	142,33	6	14	5,42	-124,61	6	14	37,10	-137,51
6	15	4,17	132,43	6	15	36,10	170,43	6	15	3,77	-78,21	6	15	34,40	-76,91
6	16	0,15	127,43	6	16	31,80	155,83	6	16	-1,57	-86,51	6	16	29,50	-91,41
6	17	-2,75	119,23	6	17	28,80	155,83	6	17	-1,63	-112,71	6	17	29,00	-117,71
7	0	-2,84	107,47	7	0	28,10	163,07	7	0	-0,97	-121,33	7	0	29,80	-130,23
7	1	0,51	118,87	7	1	32,00	167,07	7	1	-1,07	-92,63	7	1	30,10	-103,33
7	2	4,97	110,67	7	2	35,60	164,87	7	2	2,99	-83,03	7	2	34,40	-87,73
7	3	6,22	114,67	7	3	38,00	170,07	7	3	4,44	-107,23	7	3	36,70	-109,63
7	4	6,25	118,87	7	4	37,90	161,77	7	4	5,64	-112,33	7	4	37,00	-112,83
7	5	9,77	114,17	7	5	41,40	122,17	7	5	6,38	-112,13	7	5	38,10	-129,23
7	6	10,00	123,47	7	6	42,00	173,97	7	6	7,05	-111,43	7	6	39,30	-119,83
7	7	8,42	117,87	7	7	40,80	163,87	7	7	6,95	-113,33	7	7	39,30	-117,13
7	8	8,84	92,07	7	8	40,60	141,57	7	8	7,65	-102,83	7	8	38,80	-108,83
7	9	9,39	116,80	7	9	41,20	126,60	7	9	7,80	-104,82	7	9	39,90	-132,32
7	10	9,52	133,00	7	10	42,10	149,00	7	10	6,65	-89,22	7	10	38,90	-106,22
7	11	8,85	145,80	7	11	41,40	-186,40	7	11	7,53	-109,22	7	11	39,20	-113,62
7	12	8,82	126,10	7	12	41,80	118,00	7	12	7,11	-115,52	7	12	39,20	-125,72
7	13	6,31	119,90	7	13	38,30	142,50	7	13	6,61	-112,92	7	13	37,60	-110,12

7	14	7,31	133,10	7	14	38,40	138,10	7	14	5,13	-124,22	7	14	36,10	-130,52
7	15	4,58	123,30	7	15	36,70	151,20	7	15	1,56	-90,42	7	15	33,60	-65,32
7	16	0,75	125,70	7	16	33,20	141,10	7	16	-2,05	-90,42	7	16	29,30	-92,72
7	17	-2,47	118,90	7	17	29,50	135,50	7	17	-2,16	-115,72	7	17	28,90	-112,02
8	0	-2,08	115,83	8	0	29,60	146,03	8	0	-2,48	-142,20	8	0	25,20	-126,80
8	1	0,62	122,33	8	1	32,30	147,13	8	1	-2,30	-113,40	8	1	25,50	-103,60
8	2	5,28	135,23	8	2	36,40	164,13	8	2	1,69	-108,40	8	2	29,70	-87,80
8	3	5,56	143,33	8	3	38,80	165,93	8	3	4,59	-124,80	8	3	33,00	-108,80
8	4	5,18	121,33	8	4	38,10	160,33	8	4	6,18	-116,90	8	4	31,30	-118,50
8	5	9,43	102,23	8	5	41,60	134,63	8	5	7,18	-129,70	8	5	35,60	-117,00
8	6	10,16	123,73	8	6	41,90	151,83	8	6	7,47	-119,00	8	6	37,00	-111,80
8	7	8,18	118,93	8	7	40,40	154,03	8	7	7,24	-113,10	8	7	35,10	-90,50
8	8	9,27	106,63	8	8	41,40	138,83	8	8	8,76	-99,30	8	8	37,70	-90,80
8	9	9,77	111,82	8	9	41,60	129,92	8	9	8,76	-115,15	8	9	39,80	-98,95
8	10	9,49	110,32	8	10	41,50	150,62	8	10	7,57	-111,55	8	10	38,90	-105,15
8	11	7,67	125,02	8	11	40,80	165,32	8	11	6,88	-140,45	8	11	38,50	-109,45
8	12	8,80	112,12	8	12	41,80	130,42	8	12	6,79	-131,35	8	12	39,00	-120,65
8	13	6,93	128,62	8	13	38,40	156,52	8	13	6,57	-127,35	8	13	37,60	-118,45
8	14	7,13	137,32	8	14	38,40	168,72	8	14	5,15	-116,55	8	14	36,50	-91,95
8	15	5,83	126,92	8	15	37,10	154,32	8	15	2,89	-73,25	8	15	33,70	-67,25
8	16	1,56	128,82	8	16	33,30	147,42	8	16	-1,20	-91,35	8	16	30,70	-87,45
8	17	-1,72	121,32	8	17	29,90	150,22	8	17	-1,35	-118,25	8	17	30,10	-110,25